

5-2018

# Photonic tools for advanced sensing and imaging at the nanoscale.

Jafar Hamed Ghithan  
*University of Louisville*

Follow this and additional works at: <https://ir.library.louisville.edu/etd>

 Part of the [Biological and Chemical Physics Commons](#), [Biophysics Commons](#), and the [Optics Commons](#)

---

## Recommended Citation

Ghithan, Jafar Hamed, "Photonic tools for advanced sensing and imaging at the nanoscale." (2018). *Electronic Theses and Dissertations*. Paper 2933.  
<https://doi.org/10.18297/etd/2933>

This Doctoral Dissertation is brought to you for free and open access by ThinkIR: The University of Louisville's Institutional Repository. It has been accepted for inclusion in Electronic Theses and Dissertations by an authorized administrator of ThinkIR: The University of Louisville's Institutional Repository. This title appears here courtesy of the author, who has retained all other copyrights. For more information, please contact [thinkir@louisville.edu](mailto:thinkir@louisville.edu).

PHOTONIC TOOLS FOR ADVANCED SENSING AND IMAGING  
AT THE NANOSCALE

By

Jafar Hamed Ghithan  
B.S., Birzeit University, 2007  
M.S., Al-Quds University, 2010  
M.S., University of Louisville, 2014

A Dissertation

Submitted to the Faculty of the  
College of Arts and Science at the University of Louisville  
in Partial Fulfillment of the Requirements  
for the Degree of

Doctor of Philosophy in Physics

Department of Physics and Astronomy  
University of Louisville  
Louisville, Kentucky

May 2018

Copyright 2018 by Jafar Hamed Ghithan

All rights reserved



PHOTONIC TOOLS FOR ADVANCED SENSING AND IMAGING AT THE  
NANOSCALE

By

Jafar Hamed Ghithan  
B.S., Birzeit University, 2007  
M.S., Al-Quds University, 2010  
M.S., University of Louisville, 2014

A Dissertation Approved on

April 23, 2018

By the Following Dissertation Committee:

---

Dr. Sergio B. Mendes

---

Dr. Martin G. O'Toole

---

Dr. Serban Smadici

---

Dr. Ming Yu

---

Dr. Cecilia Yappert

## DEDICATION

This thesis is dedicated to my beloved wife Dalal who is the light of my life for always being a great source of motivation and inspiration in the dark nights, thank you for your patience and support. I could not have made it through without you by my side. To my little princesses Cilene and Maryam, and my little buddies Hamed and Shaher, I don't have enough words to express my love to you. To my parents Hamed and Najla thank you for your constant love, prayers and support.

## ACKNOWLEDGMENTS

I would like to express my gratitude to all people who helped me throughout this journey. First, I would like to thank my supervisor Dr. Sergio B. Mendes for his guidance to open doors for science, constant support, rigorous oversight of my research, encouraging me and also for always believing in me. I would like to particularly thank him and his family for being a welcoming friends, any time all the time, with all what it means for me and my family as we were away from our home.

I also would like to thank my dissertation committee, Dr. Martin G. O'Toole, Dr. Serban Smadici, Dr. Ming Yu, and Dr. Cecilia Yappert.

I have been privileged to collaborate and work with several people outside the group and would like to express special gratitude to: Dr. Martin G. O'Toole and his group members Dr. Monica Moreno, Betty M. Nunn and Dr. Rajat Chauhan, for their unlimited help, discussion and valuable comments on the SM-EA-IOW bio-sensing applications. Dr. Thomas J. Roussel for his help with all programming in Labview. Dr. Maureen A. McCall and Dr. Jennifer M. Noel for their help in applying STED imaging on biological samples. Dr. Bruce W. Alphenaar and Austin Carver for the work done on the STED microscopy. Dr. Wei Wang for providing all the clinical samples for SM-EA-IOW application.

I also want to thank Dr. John Morrison, Dr. Aziz Shawabka, Mohammad Halhouli and Mahmoud Halhouli for their constant support, encouragement and guidance during my studies here.

I would also like to thank all past and present members of photonics research labs at UofL: Aymen Qatamin, Shadi Alnaanah, Xue Han, Mohammed Irziqat, Scott Smith, Guilherme Sombrio..... Thank you all for sharing those years with me.

Special thanks also goes to Dr. Jayanthi Chakram, Dr. Chris Davis, Joshua Rimmer and Mary Gayle from the Department of Physics and Astronomy for their help.

Finally, I want to thank the financial support from the National Science Foundation, Jewish Heritage for Excellence and the supports from the University of Louisville.



ABSTRACT

PHOTONIC TOOLS FOR ADVANCED SENSING AND IMAGING AT THE  
NANOSCALE

Jafar Hamed Ghithan

April 23 2018

This dissertation reports a novel bio-sensing strategy based on single-mode, electro-active, integrated optical waveguide (SM-EA-IOW) platforms. It also reports the development of a super-resolved far-field optical imaging tool to enable optical, electronic, and spectroelectrochemical investigations at the nanoscale.

SM-EA-IOW platforms with its outstanding sensitivity for spectroelectrochemical interrogation was combined with a sandwich bioassay for the development of a novel immunosensing based strategy for label-free detection of infectious pathogens. The strategy begins with the functionalization of the electroactive waveguide surface with a capturing antibody aimed at a specific target analyte. Once the target analyte is bound to the photonic interface, it promotes the binding of a secondary antibody that has been labeled with a redox active reporter. This labeled antibody reporter forms the analytical signal, which is linked uniquely to both the spectral and electrochemical properties of the redox probe designed to specifically recognize a target analyte. Based on this novel detection strategy experimental results in the interrogation of influenza A (H5N1) HA protein have reached an outstanding level of detection in the picomolar range. In

addition, the novel label-free SM-EA-IOW bio-sensing strategy was successfully demonstrated for detection of gram-negative bacteria in present authentic clinical eye samples. Such demonstration has also shown the flexibility and ability of the new strategy to probe samples in the microliter volume range, without any prior processing or pre-enrichment steps.

As the groundwork towards the optimal operation of the novel sensing strategy, the effects of the adsorption process and the rate of electron transfer of redox bound species to the electrode surface were thoroughly studied. For each interface of a multilayer immunoassay assembly the surface density, the adsorption kinetic, and the electron-transfer rate of bound species of a redox-active protein were investigated using an optical impedance spectroscopy (OIS) technique based on measurements obtained with the SM-EA-IOW platform. Such methodology and acquired knowledge are crucial for the rational development of novel and advanced immuno-biosensors.

Electrochemically modulated fluorescent molecules to be conjugated with relevant antibodies for creating an electroactive probe at the nanoscale was also investigated. Such capability has the potential to enable the development of an arrayed immunosensing technology. Fluorescence emission at the nanoscale suffers from two main restrictions, diffraction limit and photobleaching effects. To address these hindrances, a modulated stimulated emission depletion microscope (STED) that is capable of achieving far-field super-resolved images was developed and used to reduce the power of the applied excitation and depletion laser beams diminish photobleaching effects in single-molecule sub-diffraction STED imaging.

These two photonic devices provide new approaches for bio-sensing from ensemble range to single molecule detection studies and sensing, where new detection limits can be reached that is expected to establish novel bio-sensing devices with higher sensitivity, specificity and easier ways of sample handling.

## TABLE OF CONTENTS

CONTENTS	PAGE
DEDICATION .....	iii
ACKNOWLEDGMENTS .....	iv
ABSTRACT.....	vi
LIST OF TABLES.....	xiv
LIST OF FIGURES .....	xv
Chapter 1 INTRODUCTION.....	1
1.1. Single-Mode Electro-Active Integrated Optical Waveguide Immunosensors .....	1
1.1.1. Immunosensors .....	1
1.1.2. Combination of electro-chemical and optical transductions .....	2
1.1.3. Single-mode electroactive integrated optical waveguide (SM-EA-IOW) .....	4
1.1.4. Benefits of spectroelectrochemical transduction using SM-EA-IOW for bio-sensing .....	6
1.2. Potential-Modulated Fluorescence Immunosensors .....	7
1.3. Hinders Limiting Single Molecule Spectroelectrochemical Imaging .....	8
1.3.1. The diffraction limit .....	8
1.3.2. Photobleaching effect.....	9
1.4. Outline of the Dissertation .....	10
Chapter 2 ADSORPTION AND ELECTRON-TRANSFER KINETICS OF REDOX PROBE AT DIFFERENT MOLECULAR ASSEMBLIES OF AN IMMUNOASSAY BY SINGLE-MODE, ELECTRO-ACTIVE, INTEGRATED OPTICAL WAVEGUIDE .....	12
2.1. Introduction.....	12
2.2. Single-Mode Electro-Active Integrated Optical Waveguides (SM-EA-IOW) .....	13
2.2.1. SM-EA-IOW fabrication.....	13
2.2.2. Potential-modulated SM-EA-IOW setup .....	15
2.2.3. Optical modulated absorbance calculations .....	17
2.3. Binding Kinetics Calculations Using Optical Impedance Spectroscopy .....	18
2.4. Electron-Transfer Rate and Mechanisms at Electro-Active Interfaces .....	20

2.4.1.	Electron transfer rate calculations using optical impedance spectroscopy .....	20
2.4.2.	Electron-transfer mechanisms at electroactive electrodes .....	21
2.5.	Functionalization Protocols of the SM-EA-IOW Surface with Layers of an Immunoassay and Cytochrome c Redox Sample Preparation .....	24
2.5.1.	APTES functionalization .....	25
2.5.2.	Recombinant protein G functionalization .....	26
2.5.3.	Primary capturing antibody functionalization.....	26
2.5.4.	Blocking buffer .....	26
2.5.5.	Recycling the SM-EA-IOW surface .....	27
2.5.6.	Cyt-C sample preparation .....	27
2.6.	Results and Discussion .....	27
2.6.1.	Adsorption of Cyt-C at different molecular assemblies under cyclic voltammetry scan .....	27
2.6.2.	Binding kinetics of Cyt-C at the different interfaces of the immunoassay .....	31
2.6.3.	Electron-transfer rate of Cyt-C at different molecular assemblies.....	33
2.7.	Conclusions.....	39
Chapter 3 INFLUENZA VIRUS DETECTION WITH A FUNCTIONALIZED SM-EA-IOW PLATFORM.....		41
3.1.	Introduction.....	41
3.2.	Bio-Sensing with the Functionalized SM-EA-IOW Platforms.....	42
3.2.1.	The strategy of using SM-EA-IOW for immunosensing .....	42
3.2.2.	Conjugation of a redox probe to a secondary antibody reporter .....	43
3.2.3.	Preliminary tests with the MB-labeled H5N1 secondary antibody .....	45
3.3.	Virus Protein Detection with Immunoassay on the SM-EA-IOW Device.....	50
3.3.1.	Influenza antigen sandwich immunoassay functionalization protocol .....	50
3.3.2.	Tests of the SM-EA-IOW platform to monitor the presence of the HA virus protein through the optical signal under CV potential modulation.....	51
3.3.3.	Optical impedance spectroscopy detection protocol.....	55
3.3.4.	AC voltammetry detection protocol and limit of detection .....	58
3.4.	Conclusions.....	60
Chapter 4 DETECTING TARGETED BACTERIA IN AUTHENTIC CLINICAL SAMPLES USING SM-EA-IOW PLATFORMS .....		62
4.1.	Introduction.....	62
4.2.	Motivation and Strategy for Clinical Sample Detection using SM-EA-IOW Platforms.....	63

4.3.	Functionalization Protocol of the SM-EA-IOW for Gram-Negative Targeted Bacteria and Preliminary Tests of the Immunoassay .....	65
4.4.	Tests and Evaluation of Clinical Samples using the SM-EA-IOW Device .....	69
4.5.	Conclusions.....	72
Chapter 5 TOWARD ELECTROFLUOROCHROMIC BIO-SENSING USING SM-EA-IOW PLATFORM UNDER POTENTIAL MODULATION .....		74
5.1.	Introduction.....	74
5.2.	Experimental .....	75
5.2.1.	Fluorescence spectroscopy.....	75
5.2.2.	Potential-modulated fluorescence spectroscopy using SM-EA-IOW .....	76
5.2.3.	Cresyl violet maleamic sample preparation .....	77
5.3.	Results and Discussion .....	78
5.3.1.	Fluorescence detection of excited cresyl violet maleamic molecules adsorbed on the surface of the SM-EA-IOW .....	78
5.3.2.	SM-EA-IOW electrofluorochromic detection of cresyl violet maleamic under potential modulation (step potential and AC impedance).....	79
5.3.3.	Preliminary tests to conjugate CrViMa into H5N1 secondary antibody.....	85
5.4.	Conclusions.....	88
Chapter 6 PHOTOBLEACHING REDUCTION AND SINGLE MOLECULE SUPER RESOLUTION IMAGING AT LOW EXCITATION AND DEPLETION POWERS WITH MODULATED STED MISCROSCOPY .....		89
6.1.	Introduction.....	89
6.1.1.	The diffraction limit.....	90
6.1.2.	Super resolution imaging techniques .....	92
6.1.3.	Principle of STED microscopy .....	93
6.1.4.	Main challenges in single molecule imaging using STED microscopy.....	95
6.1.5.	Modulated STED microscopy.....	96
6.2.	Experimental Setup (Implementation of Modulated STED Microscopy) .....	97
6.2.1.	Layout of the modulated STED microscope.....	97
6.2.2.	Excitation and depletion beam coupling.....	98
6.2.3.	Excitation and depletion beams; collimation and stage beams launch .....	99
6.2.4.	Doughnut shape .....	100
6.2.5.	Main optical path .....	101
6.2.6.	Coupling laser to objective .....	102
6.2.7.	Detection path .....	103

6.2.8.	Synchronous detection .....	104
6.2.9.	Stage and image acquisition.....	104
6.2.10.	Scanning protocol .....	104
6.3.	Validation and Alignment of the STED Setup.....	105
6.3.1.	Point spread functions of the laser beams .....	105
6.3.2.	Alignment and collinearity of the depletion and excitation beams .....	106
6.4.	Quantitative Investigation of Photobleaching and Background Reduction using Modulated STED Microscopy .....	109
6.4.1.	Sample preparation .....	109
6.4.2.	Experimental validation of the photobleaching reduction using mod STED microscopy .....	109
6.4.3.	Applications of the constructed modulated and CW STED microscope at the University of Louisville .....	125
6.5.	Conclusions.....	129
Chapter 7	SUMMARY AND OUTLOOK .....	131
7.1.	Summary .....	131
7.2.	Outlook .....	133
REFERENCES	.....	134
APPENDICES	.....	143
Appendix 1:	Optical Impedance Spectroscopy Measurements.....	143
Appendix 2:	Calculating Electron Transfer rate kET using Optical Impedance Spectroscopy.....	148
Appendix 3:	The Sensitivity for Guided Waveguide Mode, for the TE Polarization Incident Light with $\lambda = 552$ nm and $\lambda = 610$ nm. ....	151
Appendix 4:	AC Potential Modulation Parameters for Binding Kinetics Measurements of Cyt- C.....	153
Appendix 5:	Confocal imaging Characterization of Immunolayers Functionalized on the SM- EA-IOW Surface.....	155
1.	APTES .....	155
2.	ProG .....	156
3.	Cytochrome c antibody .....	157
4.	Cleaning protocol.....	159
Appendix 6:	Calculation of MB-Labeled H5N1 Ab.....	161
Appendix 7:	Technical Note Released by Xantec Bioanalytics GmbH on Nov 11, 2016. ....	163
Appendix 8:	Gram Positive and Gram Negative Bacteria .....	164

Appendix 9: Conjugation Polyclonal Lipopolysaccharides (LPS) Endotoxins Ab with Methylene Blue Ester.....	165
Appendix 10: Preparation of Cresyl Violet Maleamic Acid.....	167
Appendix 11: CrViMa Conjugation to H5N1 Secondary Antibody.....	170
Appendix 12: Fluorophore Beads Sample Preparation.....	171
Appendix 13: Retinal Slices with Fluorescently Labeled Structures Sample Preparation .....	173
CURRICULUM VITAE.....	175



## LIST OF TABLES

TABLE	PAGE
Table 1. The association rate constant ( $k_a$ ), the dissociation rate constant ( $k_d$ ) and the equilibrium constant ( $K$ ) for Cyt-C binding to different SM-EA-IOW functionalized surfaces. ....	33
Table 2: Comparison between outcomes from the SM-EA-IOW and PCR analysis of eight clinical samples. ....	72

## LIST OF FIGURES

Figure 1-1: Schematic figures for the (a) electro-reflectance, (b) transmittance and (c) potential-modulated attenuated total reflection. ....	5
Figure 1-2: Schematic of a single-mode electro-active integrated optical waveguide. Due to the propagating guided mode, the light interaction with the probes are far superior than traditional spectroelectrochemical methodologies. ....	6
Figure 2-1: (a) The single-mode electroactive integrated optical waveguide structure. (b) Reactive ion beam etching process for fabrication of surface relief gratings. (c) SEM image of the photo-patterns, which are created through a holographic exposer using a Loyd's mirror configuration and a real-time monitoring the development process. ....	15
Figure 2-2: (a) The experimental setup includes a potentiostat for electrical control of the SM-EA-IOW interface, a laser light source, a photo-multiplier detector, a current amplifier, a lock-in amplifier, and an oscilloscope for data collection. Inset (b) Schematic representation of the spectroelectrochemical flow-cell with the multilayer structure of the SM-EA-IOW platform. ....	17
Figure 2-3: Energy, $E$ , as a function of reaction coordinate, $q$ , represents a transition curve of a molecule on an electrode from its reduced state, $R$ , to its oxidized state, $O$ , the curves shows the favorable reaction paths along which the molecule will progress in case of strong or weak interaction. (a) When the interaction is strong the transition to proceeds between $R$ and $O$ states is easier, due to the well-defined continuous curve, as indicated by the curved arrow. (b) Transition curve represents the case of a weak interaction between the redox probe and the electrode, there is smaller likelihood that the system will proceed from one state to another as indicated by the straight arrow. ....	22
Figure 2-4: Inset: an illustration of different electron transfer tunneling pathways within the same multilayer ensemble on an electrode. The diagram shows a transition curve of two different tunneling pathways, a small effective tunneling distance leads to a well-defined continuous curve (dashed red curve), while an effective tunneling with long pathway leads to a sharper transition curve (solid black curve), the probability (indicated by arrows) of the reaction to proceed through tunneling pathway 2 is larger than pathway 1. ....	24
Figure 2-5: (a) Absorbance of Cyt-C plotted against electric potential at each functionalized step of the SM-EA-IOW device. The bulk concentration of Cyt-C protein was kept constant at 100 nM and the CV potential modulation parameters were the same: range of (-0.3 V to +0.3 V) and scanning speed of 20 mV/s. (b) The measured total	

surface coverage density of Cyt-C using its oxidized form at different functionalized surface. (c) The fraction for each interface of surface density of reduced species over the total surface density in the oxidized form. ....	30
Figure 2-6: (a) Absorbance amplitude change of Cyt-C binding on the ITO SM-EA-IOW surface for different concentrations in real-time. (b) Plot of the binding rate versus absorbance amplitude for different Cyt-C concentrations. (c) Plot for determining the association and dissociation constants; y-axis data points were obtained from the slope values in Figure (b) and plotted against Cyt-C concentration. ....	32
Figure 2-7: (a) Representation the optical response in the complex plane of Cyt-C at different functionalized SM-EA-IOW surface. (b) Data from the baseline measurement at different functionalized SM-EA-IOW surface, zoomed from the highlighted data presented in Figure 2-7 (a). ....	35
Figure 2-8: (a) The parametric plot of $y(\omega) = k_{ET} x(\omega)$ with the linear fitting used to retrieve the electron-transfer rate at each functionalized SM-EA-IOW surface. (b) Natural logarithm of the electron-transfer rate plotted at each different functionalized surface of the SM-EA-IOW, where the plateau and tunneling regions are indicated. ....	35
Figure 2-9: Schematic illustrate the possible role of BSA on the electron-transfer process. (a) Without BSA, Cyt-C may penetrate to a defect state and contribute to the electron-transfer rate, such defects is blocked when BSA is added. (b) The functionalized layers are uniform that adding BSA will have negligible effect on the adsorption sites of Cyt-C on the SM-EA-IOW surface, in this case BSA forms more compact layers, which may result in blocking an electron transfer pathway. Schematic representations are not to scale. ....	37
Figure 2-10: Comparison of the behavior of surface coverage, equilibrium rate constant and electron transfer rate of Cyt-C proteins at different functionalized layers. Data shown are not to scale, it is just to compare the effect of BSA upon adding to the bio-immunolayers. ....	39
Figure 3-1: Spectroelectrochemical immunoassay detection with impedance and AC voltammetry optical measurements on SM-EA-IOW platform. Inset: Steps of the sandwich bioassay with the bonded Ab, the binding of the biological target, and finally the secondary Ab with a redox-active optical tag. ....	42
Figure 3-2: 2.4 $\mu$ M MB in its oxidized state (red curve), and reduces state (green) which is colorless. Here the reduction was done chemically by using ascorbic acid 22 mM in the presence of 500 mM HCl. ....	44
Figure 3-3: (a) Strategy for conjugating secondary Ab with methylene blue ester. (b) Experimental evidence of the aimed conjugation. ....	45
Figure 3-4: Spectral molar absorptivity of methylene blue ester after conjugation with the secondary Ab at different oxidation states. The reduction was done chemically by using ascorbic acid 22 mM in the presence of 500 mM HCl. ....	46

Figure 3-5: Absorbance data as measured by the SM-EA-IOW device with a wave-guided light at 637 nm for an adsorbed sub-monolayer of the MB-labeled secondary H5N1 Ab (black and red) and an adsorbed sub-monolayer of the MB (blue trace) undergoing CV potential modulation on different SM-EA-IOW surface. ....	47
Figure 3-6: (a) Experimental setup for fluorescence data collection from the surface of the SM-EA-IOW, the setup included a monochromator connected to CCD camera for spectrally resolved measurements. (b) Fluorescence signal detected from the SM-EA-IOW platform functionalized with ITO/APTES after incubation of MB-labeled secondary H5N1 Ab (red curve) and native MB (black curve), data was collected after rinsing the flow-cell. (c) Confocal image of the SM-EA-IOW surface with adsorbed MB and (d) with adsorbed MB-labeled secondary H5N1 Ab. Confocal images (c) and (d) were acquired under same conditions and parameters, and after sonication of the SM-EA-IOW device in DI water for 10 minutes.....	49
Figure 3-7: Experimental setup for electrical control of the SM-EA-IOW interface. ....	52
Figure 3-8: Optical absorbance at 610 nm as measured by the SM-EA-IOW platform under CV scans. Red trace in the presence of HA virus antigen and black trace in the instance the virus antigen was absent from the solution.....	53
Figure 3-9: Absorbance measured in the presence of a blocking peptide that prevents the antigen adsorption.....	54
Figure 3-10: Schematic representation of the results in the figures (3-8 and 3-9) in case (a) MB-labeled H5N1 Ab is adsorbed to the surface in the presence of the target analyte. (b) When the antigen is absent. And (c) in case when a blocking peptide is used.....	55
Figure 3-11: (a) The corresponding absorbance amplitude of MB-labeled H5N1 Ab driven by an AC potential modulation measured by the SM-EA-IOW device. (b) Corresponding faradaic current density versus angular frequency for the AC potential modulation results in (a). ....	57
Figure 3-12: Faraday current density from the redox probe (MB-labeled secondary H5N1 Ab) for different volume concentrations of the virus antigen.....	59
Figure 3-13: Maximum of the faradaic current density for each volume concentration of virus antigen, which allows to determine the limit of detection. ....	60
Figure 4-1: Schematic representation of three different bacteria detection methodologies: culturing techniques (upper left), PCR-based methods (upper right), and the proposed SM-EA-IOW optical immunosensor (bottom). Note that the time indicated for each method refers to the total estimate assay time. (a) Clinical samples of aqueous and vitreous humor from the eyes of patients in the range of 100 $\mu$ L. (b) Specific capture antibodies immobilized onto the SM-EA-IOW surface for the gram negative and MB-labeled gram negative Ab. The bacteria cell fragments are captured onto the antibody-modified SM-EA-IOW surface that is then exposed to the specific MB-labeled Ab, and the modulated absorbance is measured under a modulated AC voltammetry. (c)	

Absorbance measured from the SM-EA-IOW provides the monitored optical signal. Peak at the formal potential in the absorbance curve is correlated to the presence of the targeted bacteria onto the sample.....	64
Figure 4-2: Structure of the multilayer, the SM-EA-IOW device functionalized with a sandwich bioassay: an APTES monolayer, covalently bounded primary (capture) antibody, targeted bacteria, and secondary antibody conjugated with the MB redox-active optical probe.....	66
Figure 4-3: Optical absorbance at 610 nm as measured by the SM-EA-IOW platform under CV scans. The traces correspond to the data when the SM-EA-IOW device was exposed to gram-negative bacteria fragments (black trace) and in the instance the gram-negative bacteria fragments was absent from the solution (red trace); data collected after rinsing the cell.....	67
Figure 4-4: Absorbance amplitude measured under AC potential modulation with the functionalized SM-EA-IOW device targeting endotoxin bacteria.....	68
Figure 4-5: Optical absorbance at 610 nm as measured by the SM-EA-IOW platform under CV scans for samples labeled S1 and S4 (data collected after rinsing). All other clinical samples tested showed similar noisy absorbance curves under CV scans). .....	70
Figure 4-6: Amplitude of optical absorbance at 610 nm as measured by the SM-EA-IOW platform under AC voltammetry. All curves correspond to data collected after the SM-EA-IOW device, which was functionalized with APTES and primary LPS Ab, was exposed to a particular clinical sample, as labeled, and the MB-labeled secondary Ab (10 $\mu\text{g/mL}$ ). All data was collected after rinsing. ....	71
Figure 5-1: Schematic representation of fluorescence spectrometer. ....	75
Figure 5-2: The experimental setup for fluorescence data collection from the surface of the SM-EA-IOW include a CCD camera and a monochromator for spectrally resolved measurements.....	77
Figure 5-3: (Red) Fluorescence spectrum of CrViMa (500 nM) collected by the fluorescence spectrophotometer. (Black) fluorescence spectrum of CrViMa collected from the SM-EA-IOW surface.....	79
Figure 5-4: (a) Fluorescence spectrum of CrViMa 500 nM collected from the surface of the SM-EA-IOW under step potential using a CCD spectrometer. (b) Same as in Figure 5-4(a) but here the step potential started from +0.6 V to -0.6 V. (c) (red data points) Average fluorescence at (632 $\pm$ 10) nm from the data presented in Figures 5-4(a)-(b) with a curve fitting (blue data points) and the derivative of the fitted line (black curve) to determine the formal potential. ....	81
Figure 5-5: Fluorescence of CrViMa collected from the surface of the SM-EA-IOW using excitation laser at 514 nm under AC impedance with a DC bias at -0.085 V, an amplitude of modulation of 30 mV and optical detection using a PMT with notch filter at 514 nm. ....	83

Figure 5-6: The parametric plot of $y(\omega) = k_{ET} x(\omega)$ with a linear fitting used to retrieve the electron-transfer rate of electrofluorochromic-active CrViMa molecules based on the potential-modulated fluorescence signal.....	85
Figure 5-7: Steps of the proposed sandwich bioassay with the bonded Ab, the biological target binding, and the secondary Ab with an electrofluorochromic-active optical marker. ....	86
Figure 5-8: UV-Vis absorbance of free CrViMa and CrViMa-labeled H5N1 Ab. ....	87
Figure 5-9: Fluorescence spectrum of CrViMa-labeled H5N1 Ab.....	88
Figure 6-1: Schematic diagram of a fluorescence microscope. ....	91
Figure 6-2: Schematic diagram of a confocal microscope.....	92
Figure 6-3: Schematic two-level energy diagram of a fluorescent molecule. ....	93
Figure 6-4: (a) Bright and dark states and the transition between A to B and vice versa is photoinducible. (b) The excitation spot (blue) is overlapped with the STED depletion laser profile (orange) at x-y focal plane to create an effective excitation spot below the diffraction limit. (c) The special phase plate imprints a phase factor $\exp(i n \phi)$ onto the incident beams, Gaussian beams are transformed into doughnut beams by destructive interference on the optical axis. (d): (1) Ensemble in a sample in B dark state. (2) Some portion of the ensemble is excited to state A within a diffraction limit spot size. (3) A sub-diffraction-sized effective excitation point spread function is generated by superimpose conventional excitation beam and a depletion beam exhibiting a central zero intensity zone. (4) This effective excitation point spread function is scanned across the specimen, and this results in an image that is beyond the diffraction limit. ....	94
Figure 6-5: Experimental setup with the 488 nm and 592 nm laser lines used for the excitation and depletion sources, respectively. The laser beams are injected into single-mode fibers with focusing lenses. The excitation beam was modulated using a function generator. The depletion laser was passed through a spiral phase plate to generate the doughnut shape. Both beams were circularly polarized by a quarter-wave plate. The depletion beam was collinearly aligned with the excitation laser coupled into the confocal imaging path. Laser focusing and fluorescence collection was done through an objective lens (Olympus, 100X, 1.35 NA). Sample was scanned using an XYZ piezo electrically driven stage. A photomultiplier tubes was used for light detection. The detected signal was synchronized to the excitation laser modulation using a lock-in amplifier connected to a computer for data acquisition.....	97
Figure 6-6: (a) Coupling excitation beam into SMF. (b) Coupling depletion beam into SMF.....	99
Figure 6-7: Excitation/ Depletion beam fiber launch. ....	100
Figure 6-8: The collimated depletion beam is engineered to a doughnut shaped beam using a vortex phase plate mounted on a 4-axis stage. ....	101

Figure 6-9: Main optical path combining both laser beams on the objective and also collecting the fluorescence signal. Quarter wave plate converts the beams onto circular polarization. Scanning piezoelectric stage used to construct the image. ....	102
Figure 6-10: Detection path consists of notch filters followed by 45 <sup>0</sup> mirror that sends the beam through an achromatic doublets that focus the detected fluorescence onto a multimode optical fiber. ....	103
Figure 6-11: Schematic representation of the scan strategy to construct an image. ....	105
Figure 6-12: Point spread functions of the excitation and depletion beams measured by collecting the back reflected light from a strip target. The measured FWHMs show the dimension of the laser beams are close to the diffraction limit ~200 nm. ....	106
Figure 6-13: (a) Alignment of the system; for the alignment several irises was placed at several points as indicated. The beams are send through the iris through the objective, and a back reflection mirror used to reflect back the beams through the objective lens, and the lasers are allowed to pass back through the irises to confirm optimal alignment. (b) Metallic mirror is placed on front of the beams, then the beams allowed to be reflected back and forth through irises until overlapping of the two beams was achieved. ....	107
Figure 6-14: (a) Digital camera is used to image both beams. (b) Symmetric of the two beams can be monitored overtime using the digital camera. (c) Overlapping of the two beams also monitored in real-time using the digital camera mounted on the microscope. ....	108
Figure 6-15: (a) Normalized fluorescence signal as a function of the number of scans for different CW excitation powers in the confocal imaging configuration. Each data point represents the average of normalized intensities of five different beads; for each bead the normalized intensity was calculated as $I_i/I_1$ , where $I_1$ represents the intensity of a particular bead at the first confocal image and $i_i$ refers to its intensity at the i-th image. For all images at a particular excitation power, the dwell time (75 $\mu$ s), the pixel size (15 nm), and the scan area were kept constant. For each different excitation power, a different scan spot was adopted. (b) Normalized fluorescent signal in modulated confocal imaging as a function of the modulation frequency at an average power of 16 $\mu$ W, a dwell time of 100 $\mu$ s, and a pixel size of 15 nm. For each modulation frequency, a different scan spot was adopted. (c) Normalized fluorescent signal in modulated confocal imaging as a function of the dwell time at an average power of 16 $\mu$ W, a pixel size of 15 nm, and a modulation frequency of 95 kHz. For each dwell time, a different scan spot was adopted. (d) Normalized fluorescent signal in both CW confocal and AC modulated confocal (95 kHz) as a function of the average excitation power at a dwell time of 100 $\mu$ s and a pixel size of 15 nm. For each average excitation power, a different scan spot was adopted. In Figs. (b, c, and d), each data point represents the average of normalized intensities of five different fluorescent beads and for each bead the normalized fluorescence intensity was calculated as $I_5/I_1$ , where $I_1$ is the intensity measured in the first scan and $I_5$ is the intensity after the same area was scanned five times. ....	112

Figure 6-16: A side-by-side comparison of carboxylate fluorescent beads 20 nm recorded in the (a) modulated confocal and (b) CW confocal configurations at excitation power of 7  $\mu$ W. Beads are not well recorded in the CW confocal image, but recorded with better SNR in the modulated confocal recordings. Scale bar in both images is 1  $\mu$ m. In both images pixel size and dwell time were set to be 15 nm and 30  $\mu$ s, respectively. .... 114

Figure 6-17: The normalized fluorescence intensity when overlapping two Gaussian beams: one for the excitation and one for the depletion; black curve corresponds to CW excitation beam and red curve corresponds to AC modulated excitation beam. Different scan areas were adopted for the CW and modulated excitation approaches. Also, each specific intensity in the depletion beam was performed at a different scan area. For all data points, the dwell time (100  $\mu$ s) and the pixel size (15 nm) were kept constant. .... 116

Figure 6-18: Fluorescence reduction for different STED intensities measured on the 20 nm carboxylate modified beads samples with both the modulated STED (solid) and CW STED (dashed) configurations at two different excitation powers of 7  $\mu$ W and 16  $\mu$ W (as indicated in brackets), and different embedding medium TDE (circles) and Vectashield (triangles). .... 118

Figure 6-19: A side-by-side comparison of carboxylate modified fluorescent beads recorded in the (a) CW confocal and (b) CW STED configurations. Closely-spaced beads are not well-resolved in the CW confocal image, but are better discernible in the CW STED recordings. (c) Undesirable background effects appeared in CW STED configuration when the depletion power was increased to 370 mW. Scale bar in all images is 1  $\mu$ m. The normalized intensity profiles in (d) show the spatial resolution measured to be approximately 190 nm for the CW confocal image and about 83 nm for the CW STED image at 270 mW depletion power, and due to background signal at 370 mW in CW STED the estimated resolution measured was 240 nm. .... 120

Figure 6-20: Comparison of (a) modulated confocal at excitation average power of 16  $\mu$ W, (b) modulated STED at excitation average power of 16  $\mu$ W and depletion average power of 410 mW, (c) modulated STED images at excitation average power of 7  $\mu$ W and depletion average power of 310 mW and (d) modulated STED images at excitation average power of 16  $\mu$ W and depletion average power of 310 mW of carboxylate modified 20 beads obtained for the same sample region. Scale bar is 500 nm for all images. (e) Normalized intensity profiles of the same bead in the three imaging configurations in (a) and (b) and for CW STED -image is not shown-. FWHM shown in the profiles were estimated based on a fitted lorentzian curve. The CW STED at a high power level shows degradation in the spatial resolution compared to the results of the confocal image. On the other hand, the spatial resolution measured for the modulated STED image at (b) was approximately 44 nm and for the modulated confocal was about 192 nm, at excitation average power of 16  $\mu$ W and depletion average power of 410 mW. (f) Normalized intensity profiles of the same bead in the two images in (c) and (d) FWHM shown in the profiles were estimated based on a fitted lorentzian curve. The spatial resolution measured for the modulated STED image at excitation average power



of 7  $\mu\text{W}$  and depletion average power of 310 mW was approximately 48 nm and for the modulated STED image at excitation average power of 16  $\mu\text{W}$  and depletion average power of 310 mW was approximately 68 nm. .... 123

Figure 6-21: Comparison of the (a) modulated confocal and (b) CW STED images for the 20 nm carboxylate modified fluorospheres embedded in a medium (Vectashield) that creates a significant refractive-index contrast. (c) Modulated STED image for the 20 nm carboxylate modified fluorospheres embedded in a medium (Vectashield) same area as (a) and (b). Scale bar is 500 nm in all images. (d) The normalized intensity profiles of the same particles in the modulated STED image CW STED and its modulated confocal counterpart. The estimated average spatial resolution measured was about 190 nm for the modulated confocal image, around 53 nm for the modulated STED image and due to background effect 240 nm in CW STED. .... 125

Figure 6-22: Imaging of retina bipolar cells (Gus-GFP-PNA) labeled with Alexa 488. Images from modulated confocal approach are shown in (a) and from modulated STED shown in (b). Special resolution of the smallest features presented in (c), where the black trace corresponds to the modulated confocal image and the red trace for the modulated STED. The modulated STED image demonstrates distinguishable particles that cannot be resolved by the modulated confocal imaging. Excitation average power used was about 2.0-2.5  $\mu\text{W}$  and depletion power was 95 mW. Pixel dwell time was set at 30  $\mu\text{s}$ . Scale bars in both images are 1  $\mu\text{m}$ . .... 127

Figure 6-23: The scanning capacitive photocurrent technique used for STED electrical imaging. (a) When light incident on the sample it generates separated charge pairs, (b) an additional potential is created, which to first approximation is given by  $\Delta V_p = (\frac{Q_d}{\epsilon})$ . A pulsed light source then creates a measurable ac-voltage on the electrode. It is referring to the photo-generated electrical signal as capacitive photocurrent. (c) Measurement set-up including sample holder for STED electrical imaging (d) Photo showing objective and sample holder. .... 128

Figure 6-24: (a) Schematic representation of the spectroelectrochemical flow-cell with the ITO working electrode, where the modulated fluorescence detected is after excitation the molecules. (b) Experimental setup includes a potentiostat for electrical control of the ITO interface, STED microscope, photo-multiplier detector, current amplifier, lock-in amplifier, and an oscilloscope for data collection. .... 129

## CHAPTER 1 INTRODUCTION

### 1.1. Single-Mode Electro-Active Integrated Optical Waveguide Immunosensors

#### 1.1.1. Immunosensors

There is a continuing demand for fast and simple analytical methods to establish new biosensors for the detection of clinical, biological, environmental and chemical analytes. As a result, biosensor-related research has a continuing growth over recent years [1]. A biosensor is generally defined as an analytical device which is used to convert a bio-related response into a physicochemical processable signal. Among several critical features, biosensors must show high selectivity, sensitivity, reversibility and efficient reagent usage [2]. In general, a biosensor design is consisted of three main parts: a recognition element or bioreceptors, a physicochemical transducer, and an electronic part. The main requirement of the recognition element is to provide a high degree of selectivity, and biosensor recognition incorporating antibody-antigen interactions –immunosensors– provide a promising means of detection due to their high affinity and specificity [3].

Immunosensors can be classified as competitive or noncompetitive systems [4]. In a competitive immunoassay, all reactants are mixed together simultaneously, and labeled antigens compete with unlabeled antigens for the same binding site on an antibody. Noncompetitive immunoassays (also known as “sandwich” immunoassay)

proceed in a stepwise manner: first an antibody for the target antigen is adsorbed to a solid phase. Next, the antibody-coated surface is exposed to a sample that may contain a target antigen. After the adsorption process has stabilized, a multistep washing is done to remove unbound antigens and a second antibody with a label is added to enable detection of the antigen. This immunoassay format often offers superior specificity than competitive as it uses more than one element for analyte recognition [5]. The sensitivity and simplicity of immunoassay-based biosensors depend directly on the quality of the transducer technology used.

#### 1.1.2. Combination of electro-chemical and optical transductions

Biosensors in general and immunosensors can be categorized based on the transducing signal used for detection and quantification of the targeted analyte into three main types: mass-based (piezoelectric and microgravimetric devices) [6], optical (refractive index, chemiluminescence, interferometric and fluorescent) [7, 8], and electrochemical (potentiometric, amperometric, voltammetric, capacitive, conductometric and impedance) immunosensors [2, 9-11].

Due to their rapid signal generation and non-destructive operation mode, optical and electrochemical immunosensors are considered as one of the most popular immunoassay-based biosensors [3, 12].

Typically, optical transduction in photonic biosensors is leveraged by the sensitivity of an optical mode confined to the sensing surface, which features a surface-propagating electromagnetic wave whose amplitude decays —the evanescent field— exponentially as a function of distance from the sensing surface [13]. Interactions or local changes in the evanescent field that occurs following a physicochemical event at the

sensing surface is transduced into the properties of the optical surface mode to provide a quantifiable and measured readout. Depending on the particular optical transduction approach, the form of the measured readout includes fluorescence detection [14, 15], absorbance [16], spectroscopic shifts [17] and refractive index changes [7, 18, 19].

The coupling of electrochemical transduction schemes has also been successfully demonstrated to generate immunosensors technologies that are highly selective and sensitive [18, 20-22]. Electrochemical biosensors can be divided by the electrical parameter that they measure (potentiometric, amperometric, voltammetric, capacitative, conductometric and impedance). They all share the same advantage that the electrochemical process is interfacial and gives good confinement of the sensing transduction to the sensor surface. The ability to use electrochemical impedance spectroscopies in such technique increases detection sensitivity and provides a more efficient method for bio-sensing [12, 23].

Recently, multi-sensing transduction methods in which more than one transducer are combined together have been gaining in popularity [24-27]. A combination of multi sensing transducers can extract different properties, increase the selectivity and provide information that would not be available with the respective transducer technique alone. Mainly, there has been advances in combination of conventional electrochemical and spectroscopic measurements, well known as spectroelectrochemical methods [28-30]. Such combination of optical signal and electrochemical signal provides information that would not be available with the conventional electrochemistry or optical respective techniques separately.

Spectroelectrochemical methods where an optical signal is spectrally tuned to probe exclusively the faradaic process of redox activities has been demonstrated to provide a superior route to investigate electrochemical processes in molecular adsorbates with unprecedented selectivity by avoiding nonfaradaic components that typically hinder conventional electrochemical approaches using electrical signals alone [31-34]. Also a recent report showed that applying a combination of electro-optical measurements has led to an increase in the sensitivity of specific molecular binding taking place at the sensing surface and was immune to nonspecific signals from molecules in the bulk solution [18].

#### 1.1.3. Single-mode electroactive integrated optical waveguide (SM-EA-IOW)

Transmittance and reflectance optical probing under potential modulation were the first methods to be applied for spectroelectrochemical interrogation [33, 35]. Those methods lack sensitivity due to the one-time interaction between the probing light beam and the redox species. As illustrated in Figure 1-1, a modified method with about 100X higher sensitivity than potential-modulated reflection or transmission measurements is potential-modulated attenuated total reflection [8, 31, 36]. Although those optical impedance techniques represent an important improvement over the traditional electrochemical approaches, they still lack sensitivity to probe redox species with weakly absorbing chromophores and/or at low surface concentrations. A limiting factor for superior performance has been the short path-length of interaction between the probing light beam and the redox adsorbate under interrogation.

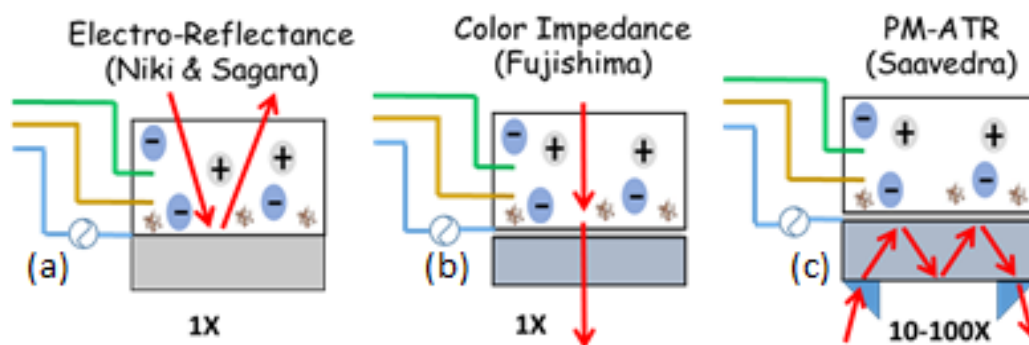


Figure 1-1: Schematic figures for the (a) electro-reflectance, (b) transmittance and (c) potential-modulated attenuated total reflection.

Recently [37], a novel optical impedance spectroscopy technique based on a single-mode, electro-active, integrated optical waveguide (SM-EA-IOW) illustrated in Figure 1-2 was developed which overcomes with far superior sensitivity the limitations of the conventional spectroelectrochemical methods. Due to the much greater effective path length provided by a SM-EA-IOW platform, experiments demonstrated that this technique provides an enhancement in sensitivity that is more than 10,000X higher compared to the electro-reflectance or transmission impedance approaches. By working under AC potential modulation on the SM-EA-IOW, the detection and full electrochemical characterization of a redox protein submonolayer with unprecedented sensitivity (better than femto-moles/cm<sup>2</sup>) was achieved. Optical measurements of low surface densities became possible by SM-EA-IOW which makes it a good candidate for bio-sensing technologies.

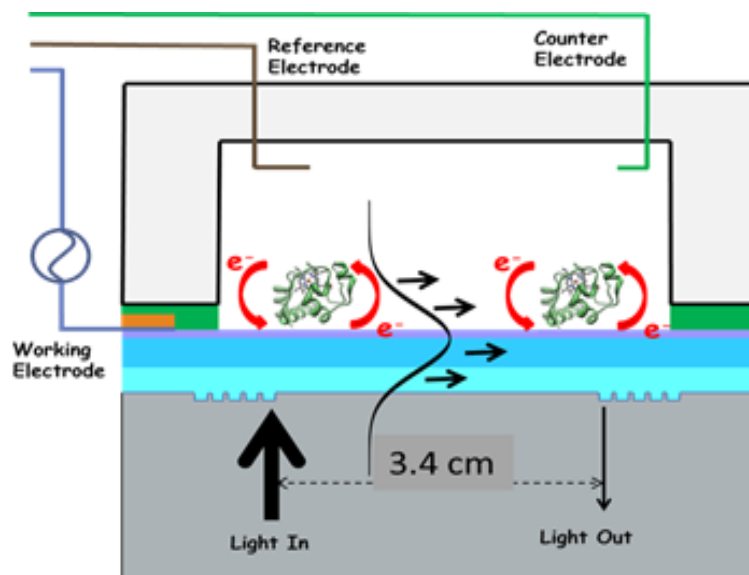


Figure 1-2: Schematic of a single-mode electro-active integrated optical waveguide.

Due to the propagating guided mode, the light interaction with the probes are far superior than traditional spectroelectrochemical methodologies.

#### 1.1.4. Benefits of spectroelectrochemical transduction using SM-EA-IOW for bio-sensing

An immunosensor-based strategy using electro-optical transduction for direct detection of biological targets based on sandwich bioassays incorporated on highly sensitive SM-EA-IOW platforms is of great interest. The selectivity of the sensor can benefit from the advantages of three highly sensing and selective methods for detection of an analyte: optical (surface guided light and wavelength of interrogation), electrochemical (using synchronous electrochemical methods such as AC voltammetry) and biological (using sandwich immunoassay). The SM-EA-IOW offers a platform of unprecedented sensitivity and an ideal approach for the creation of fully integrated biosensor devices for point-of-care applications.

## 1.2. Potential-Modulated Fluorescence Immunosensors

Due to strong baseline signals, absorbance detection methods in general and absorbance-based biosensors are limited to ensemble averages as it is challenging to reach absorption at a single molecule level. However, using fluorescence detection against a dark background, it is possible to monitor events at the level of very few molecules or even at the single molecular level [24]. Fluorescence-based biosensors have been one of the most often applied scheme in the fields of medical testing, biotechnology, and drug discovery [38, 39]. However, such technique suffers from an important weakness due to background fluorescence generated from several components present in the bulk phase (e.g., serum) of the tested samples [14]. A buildup of a methodology using an electro-optical potential-modulated fluorescence signal -fluoroelectrochromic- against a dark background, may allow SM-EA-IOW to monitor events at the level of very few molecules whose response can be switched by reversible electrochemical manipulation. Such modulated fluorescence measurements using SM-EA-IOW under potential modulation by a working electrode and the optical excitation through a guided wave can be a driving mechanism of analytical signals that are strictly confined to the device surface, which can generate a selective signal that is blind to background fluorescence from other biological components present in the bulk phase. All combined those features are expected to lead to single or a few molecules sensitive in an electro-optical transduction based immunosensor.



### 1.3. Hinders Limiting Single Molecule Spectroelectrochemical Imaging

#### 1.3.1. The diffraction limit

Fluorescence imaging microscopy is one of the most essential tool to study biological molecules, tissues, pathways and events in living cells [40, 41]. Fluorescence imaging is also being developed as a quantitative analysis method, where counting fluorescent spots in a constructed image is related to bound molecules population into the sensing or substrate surface [42, 43]. Also by using fluorescence imaging the indirect measurement of single oxidation-reduction events by observing the fluorescence was established and spectroelectrochemical measurements at the single molecule level has been demonstrated [44].

Nevertheless, imaging and even single molecule spectroelectrochemical measurements using conventional optical fluorescence microscopy is limited by the diffraction barrier of the focused light [45-47]. Even the most advanced fluorescence microscopy which is confocal microscopy can only yield optical resolution within the diffraction limit of about 200 nm, which is still larger than many substructures that cannot be resolved in detail. A consequence of this limitation is that molecules can be under-counted or over-counted without any way of independently verifying how many fluorophores are present on a surface. Such limitations have driven the development of super-resolution optical imaging methodologies capable to overcome the diffraction barrier [48]. The main far-field optical microscopy strategies with subdiffraction resolution are: structured-illumination microscopy [49], single-molecule based localization microscopy [50] and stimulated-emission depletion (STED) microscopy [51].

Stimulated emission depletion (STED) microscopy was the first and most direct approach to overcoming the diffraction limit for far-field single-molecule fluorescence imaging [52]. Briefly, the excitation light is overlapped by a high intensity donut-shaped light to depopulate markers from their fluorescent on state to the ground off state by stimulated emission, resulting in a narrower region beyond the diffraction barrier. A sharper spot is achieved by increasing the intensity of the stimulated donut-shaped light beam [53].

### 1.3.2. Photobleaching effect

Under STED imaging and in fluorescence imaging conditions in general, the fluorescence is observed to decrease substantially during imaging and over time, which is a major hurdle known as photobleaching effects [54-56]. This limiting factor in single-molecule fluorescence spectroscopy is related to the quantum yield and fluorescence stability of the probe molecules under study [57]. The photobleaching problem which results in lack of signal-to-noise ratio that limits the precision of most fluorescent techniques, has severe impact on the image formation and the collected quantitative fluorescence data. Such limitation is considered as one of the largest factors restraining future developments in single molecule spectroscopy [42]. The prevention of photobleaching is very important not only for quantitative spectroscopy but also for construction of high-quality images [58]. Unfortunately, the mechanism of photobleaching during imaging in general is not fully understood and some aspects still remain obscure [59, 60]. Although none have been yet in the position of being able to develop a technique to eliminate of photobleaching, attempts toward mitigating the phenomena are considered steps in the right track.

In STED imaging a general concept named modulated STED is a simple approach that can be used to address and minimize the photobleaching effect in single molecule fluorescence STED imaging. Modulated STED was proposed by Ronzitti and colleagues [61] that is based on an intensity modulation of the excitation laser beam combined with synchronous detection of the fluorescence signal with a lock-in amplifier while using a CW depletion beam for reaching super-resolution in far-field imaging. A study addressing the photobleaching effect is not only important for single-molecule level super-resolution imaging but also towards single molecule spectroscopic studies.

#### 1.4. Outline of the Dissertation

In chapter 2, the fabrication of SM-EA-IOW and optical impedance spectroscopy (OIS) using the SM-EA-IOW platform is briefly described. Then the surface density, adsorption kinetics and electron transfer rate of a redox-active protein probe at different interfaces of a multilayer immunoassay assembly functionalized on the SM-EA-IOW platform are investigated using OIS. In chapter 3, the detection, identification, and quantification of a targeted virus antigen using a sandwich bioassay on the SM-EA-IOW device is demonstrated. In chapter 4, the flexibility of the SM-EA-IOW platform to be used for different target analyts is demonstrated and the ability to specifically target and detect infectious bacteria from a clinical sample is presented. In chapter 5, the study electron-transfer rate of electrofluorochromic molecules under potential-modulated SM-EA-IOW fluorescence spectroscopy is applied. In Chapter 6, the design, buildup, and characterization of a super resolution modulated STED imaging technique is demonstrated, and the ability of the modulated STED to reduce and study photobleaching effect in single molecule subdiffraction imaging is discussed. In Chapter 7, concluding

remarks as well as future outlooks for possible applications of SM-EA-IOW biosensors and modulated STED optical tools are presented.

## CHAPTER 2 ADSORPTION AND ELECTRON-TRANSFER KINETICS OF REDOX PROBE AT DIFFERENT MOLECULAR ASSEMBLIES OF AN IMMUNOASSAY BY SINGLE-MODE, ELECTRO-ACTIVE, INTEGRATED OPTICAL WAVEGUIDE

### 2.1. Introduction

The development of an optimized sensor technology based on the optical interrogation of an electrically-modulated redox probe requires an electro-active interface that promotes the surface adsorption of the probe and favors an efficient electron transfer process between such probe and a supporting electrode. In this chapter an investigation of the impact of different layers forming an immunoassay on the surface density, adsorption kinetics, and electron transfer mechanisms for a particular redox-active probe is carried out. An easily handled, small, and well-established redox active probe, cytochrome c protein [62-64], was used as a reporter and a model to quantify and evaluate the molecular adsorption, the binding kinetics, and the electron-transfer mechanisms of each immunolayer required to functionalize the SM-EA-IOW device. Such characterization is important to better understand the surface properties of the biosensor and critical to address the sensitivity and reversibility of the biosensor performance. Also, using the SM-EA-IOW platform has the advantage and the ability to retrieve kinetic information and electron-transfer rate at very low surface coverages.

Since the guided optical signal is to be both optically and electrochemically locked to the targeted probe the photonic platform provides a superior route for sensitive, selective, and specific rate constants measurements. The study of adsorption kinetics and electron transfer mechanisms provides insights for advancing biosensors based on the SM-EA-IOW platform and similar technologies.

The first section of this chapter presents a description of the SM-EA-IOW fabrication, experimental setup and optical impedance absorbance measurements. The second section shows the binding kinetics calculations and electron-transfer rate calculations based on optical impedance spectroscopy measurements. Also a discussion on the electron-transfer mechanisms of redox-active molecules adsorbed on modified surface electrodes is presented. Then, functionalization protocols of bio-immunolayers is described. The next section includes the results and discussions and finally the conclusions of this chapter is provided.

## 2.2. Single-Mode Electro-Active Integrated Optical Waveguides (SM-EA-IOW)

### 2.2.1. SM-EA-IOW fabrication

A critical step in the fabrication of SM-EA-IOW devices is to provide a simultaneously extremely high optical transparency for propagation of guided waves and outstanding electrical conductivity [65]. The SM-EA-IOW platform on a glass slide was formed by a multilayer stack of a high-refractive index of alumina film, a silica as a transition layer and a transparent indium tin oxide conductive electrode. To couple a light beam in and out of the SM-EA-IOW device, a pair of surface-relief gratings (see Figure 2-1) was fabricated on the glass substrate prior to depositing the multilayer stack.

In this thesis, the waveguide grating-couplers and associated optics needed is centered at about 550 nm. To do this, both surface-relief gratings were fabricated with a pitch-size of about 323 nm, which provided a convenient coupling angle close to normal incidence to the device. The separation between the two gratings, which defines the propagation length along the SM-EA-IOW device, was set by the fabrication process to be 3.4 or 2.5 cm. Glass substrates with surface-relief gratings were then coated with highly transparent layers (e.g. alumina and silica) using an atomic layer deposition (ALD) process as described elsewhere [66]. Next, a DC sputtering technique was used to deposit the ITO layer. A careful calibration and optimization of the ITO vacuum deposition process (O<sub>2</sub> partial pressure, DC power and substrate temperature) was carefully implemented as described previously [67] to reach both high electrical conductivity and high optical transparency. In addition to the optimized vacuum deposition process, the EA-IOW devices with the ITO film were further treated with a novel UV-thermal annealing processes to optimize their optical and electrical properties. After such procedures, a single-mode EA-IOW device with an attenuation loss better than about 6 dB/cm loss calculated based on envelope technique measurements described elsewhere [66] and a resistivity of  $3 \times 10^{-3} \Omega \text{ cm}$  was fabricated.

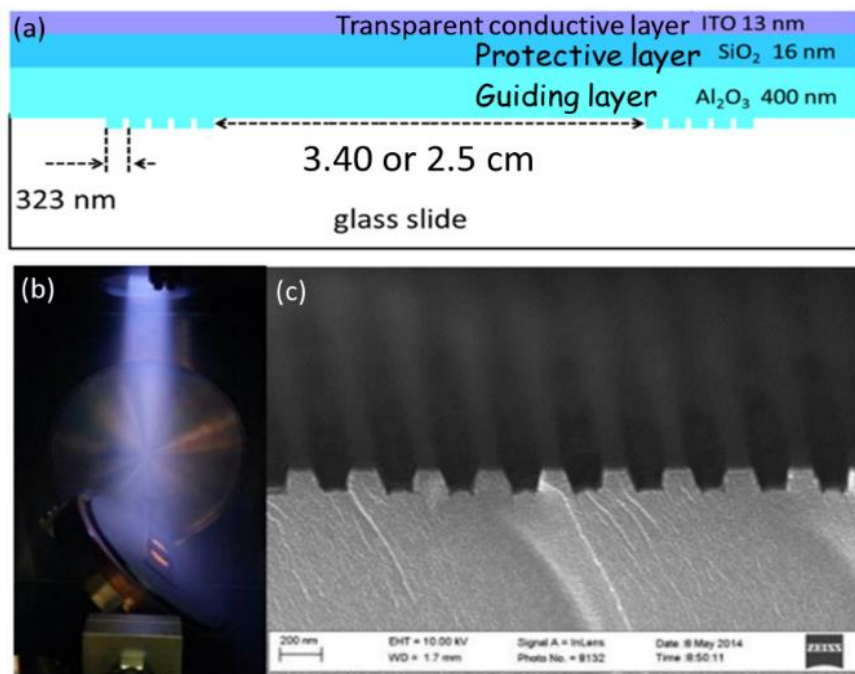


Figure 2-1: (a) The single-mode electroactive integrated optical waveguide structure. (b) Reactive ion beam etching process for fabrication of surface relief gratings. (c) SEM image of the photo-patterns, which are created through a holographic exposor using a Lloyd's mirror configuration and a real-time monitoring the development process.

### 2.2.2. Potential-modulated SM-EA-IOW setup

Figure 2-2(a) shows a schematic representation of the experimental setup that was used to control and collect data from the SM-EA-IOW platform. This optical layout, which is identical to the layout previously reported [37], was used for all spectroelectrochemical experiments. At the heart of the setup the SM-EA-IOW platform was mounted in a conventional electrochemical flow-cell (Figure 2-2(b)). A set of diffraction-limited optical components was deployed to launch the light beam towards the integrated grating coupler. Electrochemical measurements using the SM-EA-IOW were performed with standard three electrodes mounted in a homemade flow-cell configuration



(working electrode ITO film on the surface of the SM-EA-IOW device, platinum wire as counter electrodes and a Ag/AgCl electrode in 1M KCl solution as a reference electrode) to provide an electrochemically-controlled aqueous environment in the superstrate region of the photonic device. A solid state laser source with a linearly transverse-electric polarized laser light (552 nm, Coherent Obis) was routed to the input port of the SM-EA-IOW flow-cell. The out-coupled light from the SM-EA-IOW flow-cell was focused into an optical fiber by a focusing lens and directed into a photomultiplier detector (PMT, H5783, Hamamatsu), which was connected to a low-noise current preamplifier (SR570, Stanford Research Systems). The optical signal was monitored while a potentiostat (CHI 660D, CHInstruments, Inc.) was used to control the electric potential applied to the working electrode. In AC potential-modulated absorbance measurements, the collected PMT signal that is electronically processed by a current pre-amplifier was sent to a lock-in-amplifier (SR810, Stanford Research Systems). A function generator (DS345, Stanford Research Systems) connected to the potentiostat provided a continuous sinusoidal wave to electrically drive the SM-EA-IOW working electrode, and was used to provide a trigger to the lock-in-amplifier for impedance measurements. An oscilloscope (DSO8104A Infiniium, Agilent) was used to read and record all signal measurements.

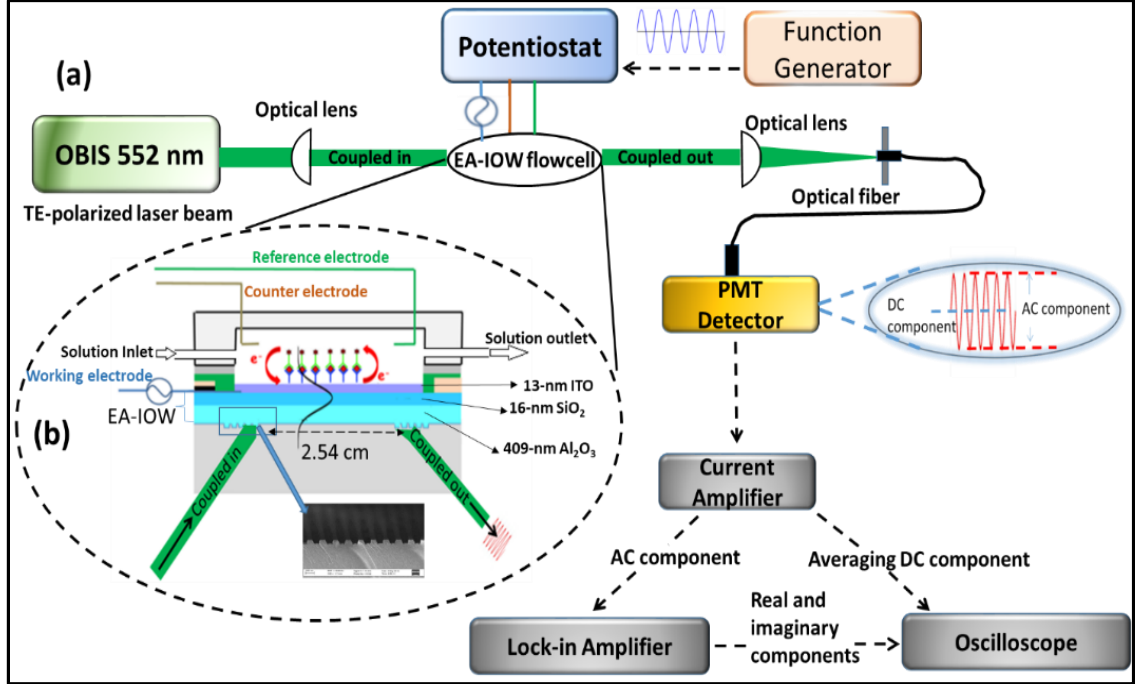


Figure 2-2: (a) The experimental setup includes a potentiostat for electrical control of the SM-EA-IOW interface, a laser light source, a photo-multiplier detector, a current amplifier, a lock-in amplifier, and an oscilloscope for data collection. Inset (b) Schematic representation of the spectroelectrochemical flow-cell with the multilayer structure of the SM-EA-IOW platform.

### 2.2.3. Optical modulated absorbance calculations

For optical impedance spectroscopy measurements, the modulated absorbance was obtained as described in details elsewhere [37]. Briefly, under an AC potential modulation,  $E = E_{dc} + \Delta E_{ac} \sin(\omega t)$ , (where  $E_{dc}$  represents the DC bias term and  $\Delta E_{ac}$  represents the amplitude of an AC modulation at angular frequency  $\omega$ ) a modulated optical signal is measured for a light beam propagating along the SM-EA-IOW device. First, baseline optical data under AC electrical potential modulation in the absence of the redox adsorbate is collected and can be described as  $I_0 = I_{dc,0} + \Delta I_{ac,0} \sin(\omega t + \theta_0)$

where  $I_{dc,0}$  represents a term that is constant in time and its value will depend solely on  $E_{dc}$ . The term  $\Delta I_{ac,0}$  represents the amplitude, and the term  $\theta_0$  represents the phase of the optical signal response originated under the electric potential modulation. Next, in the presence of a redox probe the modulated optical signal is measured and can be described by,  $I = I_{dc} + \Delta I_{ac} \sin(\omega t + \theta)$ , where  $I_{dc}$  represents a term that is constant in time and its value will depend solely on  $E_{dc}$ . The term  $\Delta I_{ac}$  represents the amplitude, and the term  $\theta$  represents the phase of the optical signal response originated under the electric potential modulation in the presence of a redox active molecule. As shown in [37] the in-phase ( $\Delta A'_{ac}$ ) and out-of-phase ( $\Delta A''_{ac}$ ) components of the AC modulated optical absorbance in the presence of a redox species can be determined by:

$$\Delta A'_{ac} = -\frac{\Delta I_{ac} \cos(\theta)}{I_{dc} \ln(10)} + \frac{\Delta I_{ac,0} \cos(\theta_0)}{I_{dc,0} \ln(10)} \quad \text{Equation 2-1}$$

$$\Delta A''_{ac} = -\frac{\Delta I_{ac} \sin(\theta)}{I_{dc} \ln(10)} + \frac{\Delta I_{ac,0} \sin(\theta_0)}{I_{dc,0} \ln(10)} \quad \text{Equation 2-2}$$

From the in-phase and out-of-phase components of the AC modulated optical absorbance one can measure the total absorbance amplitude, which equals to:

$$\Delta A_{ac} = \sqrt{(\Delta A'_{ac})^2 + (\Delta A''_{ac})^2} \quad \text{Equation 2-3}$$

Additional details on the above equations and how to retrieve optical absorbance can be found in Appendix 1.

### 2.3. Binding Kinetics Calculations Using Optical Impedance Spectroscopy

The adsorption and interactions of Cyt-C proteins to a particular interface, which is referred here as the phase state ( $P_s$ ), to form the complex (Cyt-C: $P_s$ ) can be formulated by the following equation [68, 69]:



and the rate complex formation can be described by:

$$\frac{d[CytC:P_s]}{dt} = k_a[CytC][P_s] - k_d[CytC:P_s] \quad \text{Equation 2-5}$$

where  $[CytC]$  is the concentration of Cyt-C in the bulk solution,  $[P_s]$  is the concentration of total phase state,  $[CytC:P_s]$  is the concentration of the complex formed between Cyt-C and phase state,  $k_a$  is the association rate constant, and  $k_d$  is the dissociation rate constant.

The total phase states ( $P_s^{tot}$ ) concentration in each experiment at each functionalized surface is constant and equal to the sum of the bound  $[CytC:P_s]$  and unbound  $[P_s]$  phase state concentrations,  $P_s^{tot} = [CytC:P_s] + [P_s]$ . Then the differential in Equation 2-5 becomes

$$\frac{d[CytC:P_s]}{dt} = -(k_a[CytC] + k_d) [CytC:P_s] + \alpha k_a P_s^{tot} [CytC] \quad \text{Equation 2-6}$$

Where  $\alpha$  is a variable constant and obviously the complex Cyt-C: $P_s$  concentration,  $[CytC:P_s]$ , which resulted from the adsorption of Cyt-C on the electrode surface, is linearly proportional to the absorbance  $\Delta A_{ac} \propto [CytC:P_s]$ . One can measure the optical absorbance amplitude as it change over time using Equation 2-3 under an AC potential modulation. Therefore, Equation 2-6 can be rewritten as:

$$\frac{d(\Delta A_{ac}(t))}{dt} = -(k_a[CytC] + k_d)\Delta A_{ac}(t) + \alpha k_a P_s^{tot} [CytC] \quad \text{Equation 2-7}$$

From Equation 2-7 a plot of  $\frac{d(\Delta A_{ac}(t))}{dt}$  vs  $\Delta A_{ac}(t)$  gives a straight line with slope ( $S_{\Delta A_{ac}}$ ) given by  $S_{\Delta A_{ac}} = -k_a[CytC] - k_d$ . Then by collecting the data for several Cyt-C concentrations and creating an additional plot of  $S_{\Delta A_{ac}}$  vs  $[CytC]$ , a straight line will be generated with a slope and y-intercept equal to  $-k_a$  and  $-k_d$ , respectively.

## 2.4. Electron-Transfer Rate and Mechanisms at Electro-Active Interfaces

### 2.4.1. Electron transfer rate calculations using optical impedance spectroscopy

To obtain and retrieve electron-transfer rate of redox events from the optical absorbance measurements obtained under AC potential modulation a methodology was used as described previously [70]. Simply, in order to determine the electron-transfer rate ( $k_{ET}$ ) using OIS with SM-EA-IOW, it is enough to collect both the electrical impedance  $Z(\omega)$  of the electrochemical flow-cell and the modulated absorbance amplitude,  $\Delta A_{ac}(\omega)$ . For the electrochemical reaction described in Appendix 2,  $k_{ET}$  can be expressed as:

$$k_{ET} = \frac{1}{2C_a R_{ct}} = \frac{y(\omega)}{x(\omega)} \quad \text{Equation 2-8}$$

where  $y(\omega)$  and  $x(\omega)$  are defined as

$$x(\omega) = 2[Z'_{tot}(\omega)\Delta A'_{ac}(\omega) - Z''_{tot}(\omega)\Delta A''_{ac}(\omega)] \quad \text{Equation 2-9}$$

and

$$y(\omega) = \omega [Z'_{tot}(\omega)\Delta A''_{ac}(\omega) + Z''_{tot}(\omega)\Delta A'_{ac}(\omega)] \quad \text{Equation 2-10}$$

where  $Z'_{tot}(\omega)$  and  $Z''_{tot}(\omega)$  are the real and imaginary parts of the total electrical impedance, respectively, which are recorded by the potentiostat, and  $\Delta A'_{ac}(\omega)$  and  $\Delta A''_{ac}(\omega)$  are obtained from the optical impedance measurements. With  $Z_t(\omega)$  and  $\Delta A_{ac}(\omega)$  known, as shown in Equation 2-8, one can use a parametric plot of  $y(\omega)$  against  $x(\omega)$ , from which a linear graph is formed with a slope equal to the electron-transfer rate,  $k_{ET}$ , of the faradaic process.

#### 2.4.2. Electron-transfer mechanisms at electroactive electrodes

The behavior of electron-transfer rate of redox active molecules with the thickness of molecular assemblies on an electrode displays mainly two regimes, known as a plateau region and a tunneling region [63, 71, 72].

The plateau region lies at smaller layer thicknesses, where the electron-transfer rate shows weak dependence on thickness and distance from the electrode [73]. The difference of electron-transfer rates in this region is controlled by either conformational gated mechanisms [74] or friction control mechanisms [75, 76]. In conformational-gated mechanisms, the electron-transfer process is controlled by a nuclear rearrangement of the redox-active molecules [77, 78]. While in friction electron-transfer mechanisms [79], the electron-transfer event depends on the characteristic relaxation mobility of the redox molecules [80] and the strength of the interaction between the immobilized species and the modified electrode [81].

A transition oxidation-reduction reaction curve [82] can be used to illustrate the effect of the interaction strength between a redox probe and an electrode on the electron-transfer rate. In a transition curve of oxidation-reduction reaction at an electrode, the potential energy of a molecule is drawn as a function of a generalized reaction coordinate. For example, during the course of a reduction reaction the system first moves along the curve of oxidized state towards the reduced state till it reaches a transition state, where the electron transfer only occurs at this crossing point, according to Franck-Condon principle [83], and the system proceeds to its new state.

In case of a strong interaction between adsorbed molecules and the electrode a transition curve can be illustrated as shown in [Figure 2-3\(a\)](#). In such case a well-defined

continuous transition curve with a large splitting between the reaction paths is expected; generally, the reaction will proceed via the path with the smallest energy needed. As illustrated in Figure 2-3(a) when the molecule reaches the transition state it will be easier to proceed to the other corresponding state as indicated by the curved arrow. On the other hand, a weak interaction leads to a smaller splitting of the reaction paths and when molecules reach the transition state it has a tendency to remain in the same state, as indicated with the straight arrow in Figure 2-3(b).

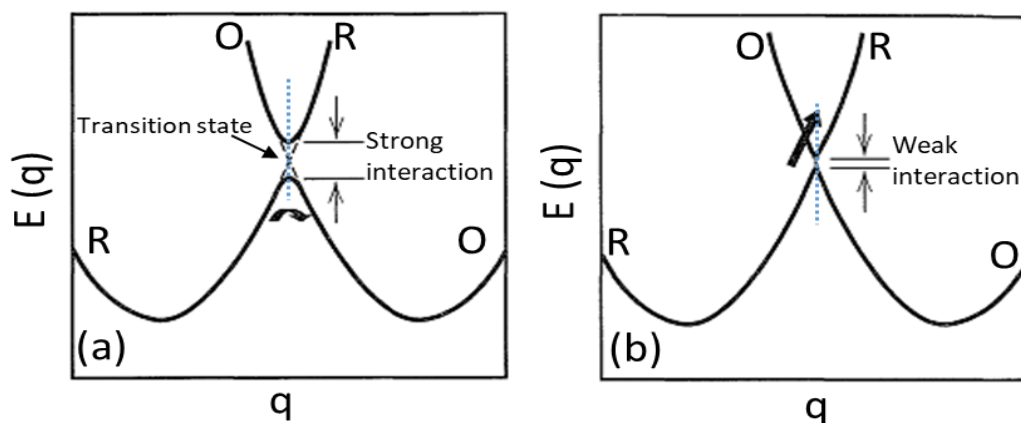


Figure 2-3: Energy,  $E$ , as a function of reaction coordinate,  $q$ , represents a transition curve of a molecule on an electrode from its reduced state, R, to its oxidized state, O, the curves shows the favorable reaction paths along which the molecule will progress in case of strong or weak interaction. (a) When the interaction is strong the transition to proceeds between R and O states is easier, due to the well-defined continuous curve, as indicated by the curved arrow. (b) Transition curve represents the case of a weak interaction between the redox probe and the electrode, there is smaller likelihood that the system will proceed from one state to another as indicated by the straight arrow.

The electron-transfers of redox adsorbed molecules on an electrode functionalized with thick layers is controlled by the electron tunneling probability. In this region the electron-transfer rate is predicted by an exponential decay as a function of effective electron transfer distance described by the following equation [84],

$$k_{ET} \propto e^{-(\alpha R_{eff})} \quad \text{Equation 2-11}$$

where  $\alpha$  is a decay factor and  $R_{eff}$  is the effective electron-transfer distance.

In this region the main differences in electron-transfer rates are due to the physical distance of the redox probe from the electrode [76]. Another contribution may come from the differences in the electronic path coupling between the redox probe and the electrode, which is related to the minimum energy required for a redox probe to proceed from one state to another. Such variations in coupling could result in different tunneling pathways with ones that are more effective than others [85, 86]. A distribution of tunneling pathways can be illustrated as shown in Figure 2-4, where a functionalized layer on an electrode has two tunneling pathways that have the same physical distance, but the effective tunneling separation of the two pathways are not the same. If one considers that tunneling pathway 2 has smaller effective distance, then when the reaction reaches a transition state as indicated by the transition curves, it has higher probability to proceed through tunneling pathway 2 denoted by the red curved arrow.



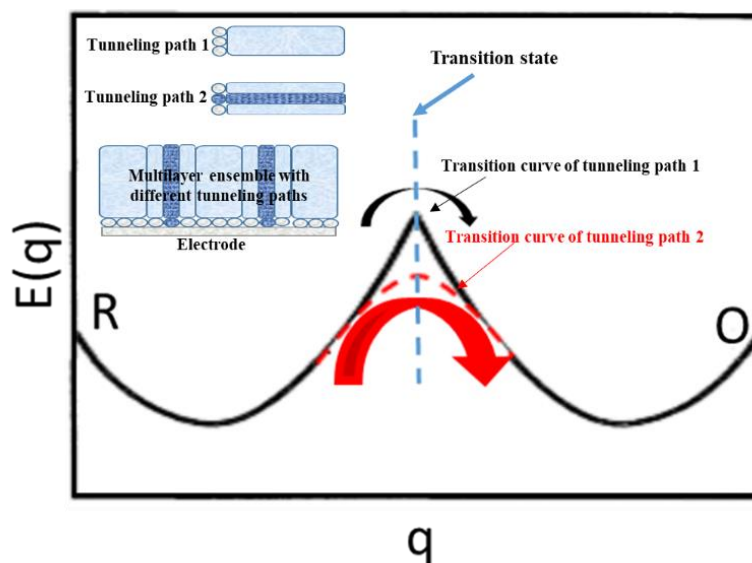


Figure 2-4: Inset: an illustration of different electron transfer tunneling pathways within the same multilayer ensemble on an electrode. The diagram shows a transition curve of two different tunneling pathways, a small effective tunneling distance leads to a well-defined continuous curve (dashed red curve), while an effective tunneling with long pathway leads to a sharper transition curve (solid black curve), the probability (indicated by arrows) of the reaction to proceed through tunneling pathway 2 is larger than pathway 1.

## 2.5. Functionalization Protocols of the SM-EA-IOW Surface with Layers of an Immunoassay and Cytochrome c Redox Sample Preparation

Immobilization protocols of immunolayers on the SM-EA-IOW surfaces are crucial for evaluating the adsorption and electron-transfer kinetics in a redox process. The ability to renew the surface, sensitivity combined with the specificity are all highly dependent on the surface functionalization process. To functionalize the SM-EA-IOW with layers of an immunoassay the protocols described below were followed. More

detailed information on the characterization of the morphology of the functionalized layers can be found in Appendix 2.

Each new SM-EA-IOW device and prior to its first usage was electrochemically stabilized by applying 10 CV cycles followed by about 20 minutes of relaxation time prior to any additional processing or data collection.

#### 2.5.1. APTES functionalization

3-(Aminopropyl) triethoxysilane (APTES) is one of the most frequently used organic silane coupling agent that is chemically reactive for enabling the introduction of bioactive groups on a substrate [87]. Here, the addition of APTES provides a facile conjugation/adsorption strategy for successive protein layers on the ITO interface of the SM-EA-IOW device [88]. Surface preparation began with cleaning of the SM-EA-IOW to remove any contamination. This procedure was accomplished by sequentially sonicating the SM-EA-IOW device in deionized (DI) water, acetone, ethanol and 2-propanol for 15 minutes each time and then drying with N<sub>2</sub> gas. The ITO surface of the SM-EA-IOW was then functionalized with APTES (purchased from Sigma Aldrich) by immersing the device overnight into a solution containing 10 mL of 2-propanol, 100  $\mu$ L of APTES, and 4 to 5 drops of DI water; the device surface was then thoroughly rinsed with 2-propanol and DI water, and dried under N<sub>2</sub>. Some portion of APTES can be just physically adsorbed to the working surface [89], so in order to remove those APTES species the SM-EA-IOW was sonicated in DI water for 15 minutes. Later here the data for SM-EA-IOW functionalized solely with the APTES layer is referred to as “.../APTES”.

### 2.5.2. Recombinant protein G functionalization

Recombinant protein G (ProG) is a commonly used antibody-binding protein adopted in several immunoassay systems [90]. ProG (from proprietary source purchased from Sigma Aldrich) with a concentration of 4 µg/mL was adsorbed to the APTES layer to promote the capture and the proper orientation of the antigen-binding sites in the immobilized antibodies; those binding sites should be oriented away from the solid phase for optimum conditions to capture the target analytes. In order to remove aggregated ProG molecules, the ProG solution was filtered using a 0.2 µm membrane filter before being used. The SM-EA-IOW functionalized with ProG is later referred to as ".../ProG".

### 2.5.3. Primary capturing antibody functionalization

Next, after the proper protocols were established for creating a resilient layer of ProG on the SM-EA-IOW device surface, the ProG surface was exposed to capture antibodies (Ab) –Cyt-C antibody (A-8) mouse monoclonal IgG2b (purchased from Santa Cruz Biotechnology)–. The SM-EA-IOW functionalized with Cyt-C Ab is later referred to as ".../Cyt-C Ab".

### 2.5.4. Blocking buffer

A blocking buffer solution containing 1% Bovine Serum Albumin (BSA) (purchased from Sigma Aldrich) was deployed, which is typically used to minimize non-specific adsorption on a surface of interest. The SM-EA-IOW functionalized with BSA is later referred to as ".../BSA".

#### 2.5.5. Recycling the SM-EA-IOW surface

By sonicating the ITO/APTES/ProG/Ab SM-EA-IOW surface in a potassium carbonate solution with pH 9-11, it was possible to reverse the interaction between ProG and ProG/Ab with the ITO/APTES surface, enabling easy renewal of the sensing surface.

#### 2.5.6. Cyt-C sample preparation

Cytochrome c from horse heart with 99.7 % purity was purchased from Sigma Aldrich. A stock solution of Cyt-C at its oxidized state was prepared by dissolving small unknown weight of Cyt-C in 50 mM phosphate buffer solution (PBS) with pH 7. The protein concentration ( $C$ ) was calculated by measuring the absorbance ( $A$ ) using UV-Vis spectrophotometer at  $\lambda = 409$  nm and using Beer's law  $C = A/(\epsilon b)$ , where  $\epsilon$  is the molar absorptivity of Cyt-C in its oxidized form at wavelength 409 nm  $106,000 \text{ M}^{-1}\text{cm}^{-1}$  and  $b = 1$  cm. With a stock solution of known concentration different Cyt-C concentrations were then prepared by dilutions as desired.

### 2.6. Results and Discussion

#### 2.6.1. Adsorption of Cyt-C at different molecular assemblies under cyclic voltammetry scan

The setup described in Figure 2-2 (without synchronous detection) was used to evaluate the effect of each functionalized interface on the adsorption of Cyt-C. This study was done under cyclic voltammetry (CV) potential modulation because it provides a clear and simple identification of the redox process. At each functionalized surface, CV scan was set with a potential interval from -0.3 V to +0.3 V and a scan speed of 20 mV/s. Optical data under CV scan was collected first without the presence of Cyt-C proteins in

the flow-cell. Then, a 2 mL of 100-nM Cyt-C solution was injected into the flow-cell and another 30 minutes was used to stabilize the adsorption process of Cyt-C proteins on top of the functionalized surface. Next, a 10 mL of PBS, which corresponds to about five times the volume of the flow-cell, was used to rinse the electrochemical flow-cell. Finally, the optical data under CV potential scan under the same parameters as mentioned above were collected with Cyt-C proteins present in the flow-cell. Such optical signals with and without Cyt-C were then used to generate the absorbance plot using the expression of absorbance ( $A$ ) written as:

$$A = -\log \frac{I_{\text{Cyt-C}}}{I_0} \quad \text{Equation 2-12}$$

where  $I_0$  refers to the optical baseline signal and  $I_{\text{Cyt-C}}$  the optical signal with Cyt-C adsorbed on the SM-EA-IOW.

In Figure 2-5(a) the optical absorbance of Cyt-C is plotted against the electric potential at each functionalized layer on the SM-EA-IOW device under CV potential modulation. For each measurement, the bulk concentration of Cyt-C protein was kept at 100 nM and the parameters for the CV potential modulation were also kept the constant. Between each set of measurements displayed in Figure 2-5(a), the SM-EA-IOW device was re-cleaned using the protocols described above. The measured absorbance in the oxidized state, which is marked by the black rectangle in Figure 2-5(a), was used to determine the total surface density ( $\Gamma$ ) of the adsorbed probe species, Figure 2-5(b), using the formula  $\Gamma = A/(S \epsilon_{ox})$ , where  $S$  is the sensitivity factor of the SM-EA-IOW device ( $\sim 14500$ , see Appendix 3) and  $\epsilon_{ox}$  is the molar absorptivity of the redox probe (Cyt-C) in its oxidized state and equals to  $9.0 \times 10^3 \text{ M}^{-1} \text{ cm}^{-1}$  at 552 nm (note Appendix 1). Next the data was used in the reduced state, which is marked by the red rectangle in

Figure 2-5(a), to calculate for each interface the fraction of reduced species over total surface density; the results are shown in Figure 2-5(c). The reduced surface coverage was measured using the formula  $\Gamma_{red} = A_{red}/(S \varepsilon_{red})$ , where  $\Gamma_{red}$  is the total surface coverage of Cyt-C in its reduced state,  $A_{red}$  is the absorbance measured at the reduced state of Cyt-C and  $\varepsilon_{red}$  is the molar absorptivity of the redox probe (Cyt-C) in its reduced state and equals to  $27.7 \times 10^3 \text{ M}^{-1} \text{ cm}^{-1}$  at 552 nm.

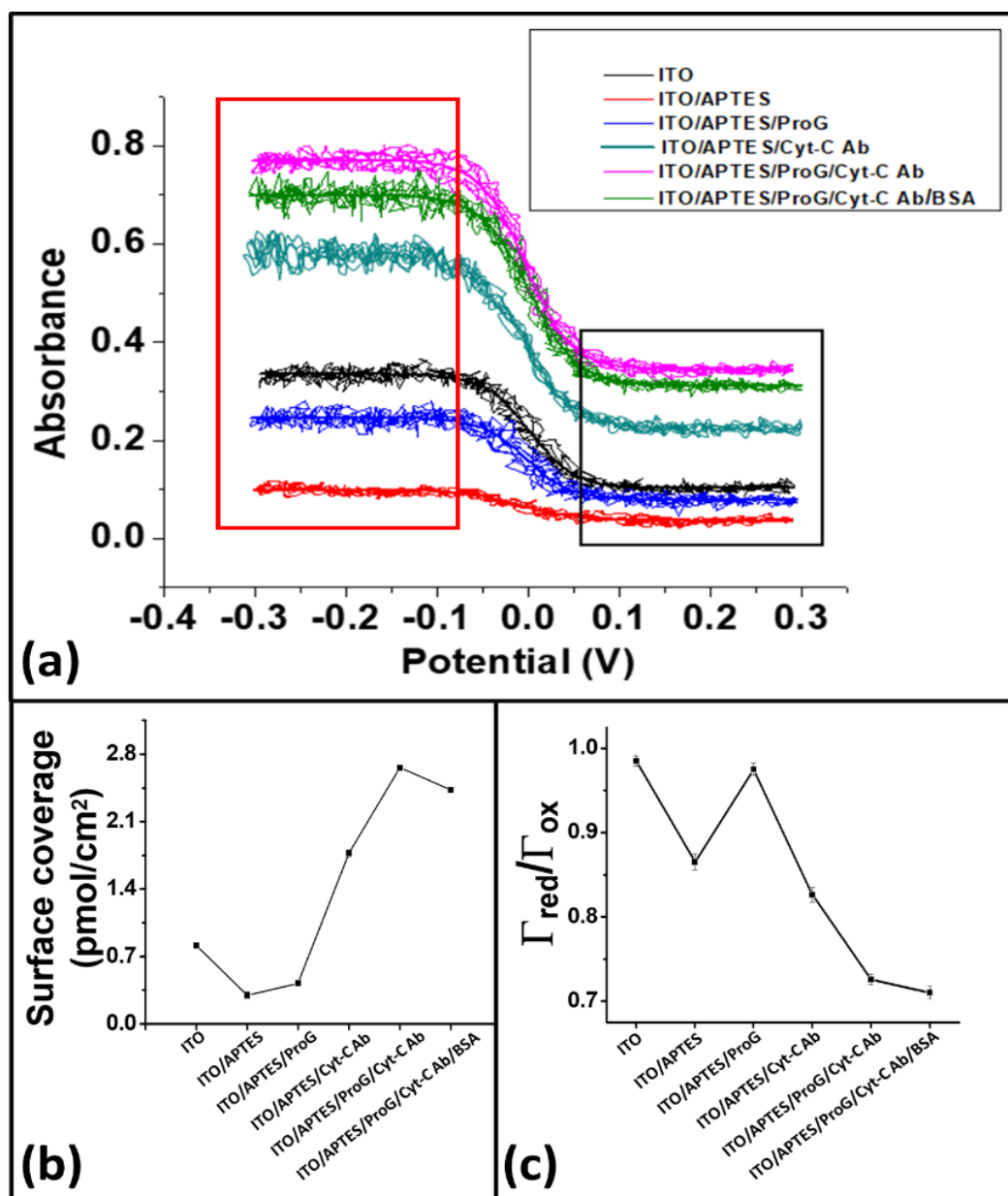


Figure 2-5: (a) Absorbance of Cyt-C plotted against electric potential at each functionalized step of the SM-EA-IOW device. The bulk concentration of Cyt-C protein was kept constant at 100 nM and the CV potential modulation parameters were the same: range of (-0.3 V to +0.3 V) and scanning speed of 20 mV/s. (b) The measured total surface coverage density of Cyt-C using its oxidized form at different functionalized surface. (c) The fraction for each interface of surface density of reduced species over the total surface density in the oxidized form.

As can be observed in Figure 2-5(b-c), the functionalized surface has a strong influence on Cyt-C adsorption to the SM-EA-IOW surface. The presence of ProG in combination with the capturing Ab greatly increases the binding affinity, which may indicate that the ProG is indeed working to orient the capturing Ab. Typically, the BSA is used to eliminate nonspecific binding events, however, the results indicate that there is a small change in the surface coverage of Cyt-C with and without BSA, such small change is most likely due to the dense, complete functionalization of the immunolayers which leads to minimizing the nonspecific binding of Cyt-C. The data presented in Figure 2-5(c) shows, for each layer formed onto the SM-EA-IOW, the transition of Cyt-C to its correspondent reduced state decrease, this data shows indeed that each additional layer acts as a barrier for the electron transfer process and also confirm the success functionalization of the biological layers. Also, the data in Figure 2-5(a) confirms the ability of the SM-EA-IOW platform to optically detect and quantify the electron-transfer process of redox species adsorbed on all the multilayer stacks that were deployed to functionalize the SM-EA-IOW surface. Such assurance forms the basis of electro-optical transduction sensing methodology using SM-EA-IOW photonic platforms.

### 2.6.2. Binding kinetics of Cyt-C at the different interfaces of the immunoassay

Figure 2-6 shows the evaluation of rate constants for Cyt-C adsorption on bare ITO SM-EA-IOW platforms. Using the same experimental setup illustrated in Figure 2-2 absorbance amplitudes were measured under synchronous detection during the adsorption process at different Cyt-C concentrations (10, 50 and 100 nM) injected into the flow-cell from low to high concentrations. Both modulated optical baseline and optical signal were collected by applying an AC modulated potential with a frequency of 25 Hz, 10 mV amplitude of modulation and a DC bias of -10 mV; additional information on the data collection can be found in Appendix 4. The optical baseline response with the corresponding x (in-phase) and y (out-of-phase) components via synchronous detection were recorded at time zero. Then for each Cyt-C concentration injected into the flow-cell the optical response, x and y components via synchronous lock-in detection were recorded every 30 seconds for the first six minutes and after that every three minutes. For each concentration of Cyt-C injected into the flow-cell the absorbance amplitude was recorded for a total time of 40 minutes, which is approximately the time needed to reach a plateau adsorption region as shown in Figure 2-6(a). Each data point as a function of time was calculated as described in Appendix 1 with baseline collected at time zero.

To calculate the binding constants for Cyt-C adsorbed on ITO SM-EA-IOW surface the formalism in section 2.3 was adapted as follow; Figure 2-6(a) corresponds to the absorbance amplitude of Cyt-C proteins adsorbed on ITO surface versus time with concentrations as indicated. First, for each interaction curve in Figure 2-6(a), an exponential curve fit of the absorption amplitude as a function of time,  $\Delta A_{ac}(t)$ , was used to measure the modulated amplitude rate  $\frac{d(\Delta A_{ac}(t))}{dt}$ . Then,  $S_{\Delta A_{ac}}$  was calculated by



plotting the binding rate  $\frac{d(\Delta A_{ac}(t))}{dt}$  versus absorbance amplitude,  $\Delta A_{ac}(t)$ , and is plotted in Figure 2-6(b). Next, each  $S_{\Delta A_{ac}}$  obtained from Figure 2-6(b) was plotted against its corresponding [Cyt-C], results shown in Figure 2-6(c). Finally, a linear fit from which the association  $k_a$ , and dissociation  $k_d$  binding constants were calculated from the slope and the y-intercept of the fitted line, respectively.

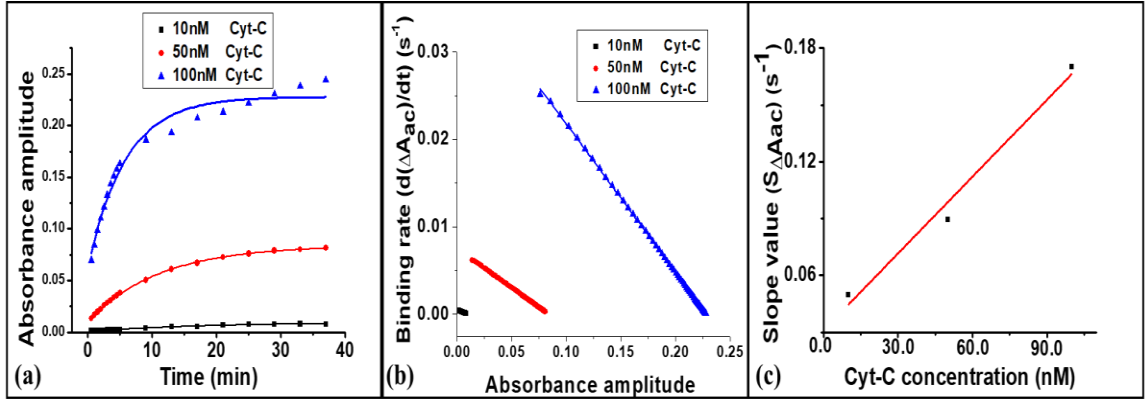


Figure 2-6: (a) Absorbance amplitude change of Cyt-C binding on the ITO SM-EA-IOW surface for different concentrations in real-time. (b) Plot of the binding rate versus absorbance amplitude for different Cyt-C concentrations. (c) Plot for determining the association and dissociation constants; y-axis data points were obtained from the slope values in Figure (b) and plotted against Cyt-C concentration.

Following the same kinetic measurements and procedure of Cyt-C on ITO, Cyt-C kinetic measurements at the different functionalized immunolayers assemblies were carried out. Between each set of measurements, the SM-EA-IOW device was re-cleaned using the protocols already described above. Table 1 summarizes the results of the association and dissociation rate constants of Cyt-C interaction, and the equilibrium constant defined as  $K = k_a/k_d$ , at the different immunolayer assemblies functionalized on the SM-EA-IOW device. From the results it is noticed that each layer surface has a

strong influence on the affinity of Cyt-C binding to the SM-EA-IOW surface. It can be noticed that the presence of a capturing Cyt-C Ab increases the binding affinity and the equilibrium rate constants of Cyt-C to the functionalized electrode surface. Furthermore, the lowest binding affinity of Cyt-C was observed when the SM-EA-IOW was functionalized with APTES, such low affinity is due to the weak interaction between Cyt-C and APTES, as APTES as well as Cyt-C have positive charges at neutral pH [91, 92]. Moreover, in comparison to the ITO/APTES/ProG/Cyt-C Ab immunolayer one can notice the small change in the overall equilibrium constant when a blocking buffer -BSA- was used. This small change may indicate the homogeneous morphology of the functionalized immunolayers on the SM-EA-IOW device surface, such hypothesis is also supported by the adsorption measurements of Cyt-C where only a small effect on the surface coverage of Cyt-C was observed when BSA was used (Figure 2-5).

Table 1. The association rate constant ( $k_a$ ), the dissociation rate constant ( $k_d$ ) and the equilibrium constant ( $K$ ) for Cyt-C binding to different SM-EA-IOW functionalized surfaces.

SM-EA-IOW functionalized surface	$k_a$ ( $s^{-1} M^{-1}$ )	$k_d$ ( $s^{-1}$ )	$K = \frac{k_a}{k_d}$ ( $M^{-1}$ )
ITO	$1.35 \times 10^6$	0.0311	$4.34 \times 10^7$
ITO/APTES	$0.62 \times 10^6$	0.1630	$0.38 \times 10^7$
ITO/APTES/ProG	$1.65 \times 10^6$	0.0284	$5.81 \times 10^7$
ITO/APTES/ProG/Cyt-C Ab	$1.90 \times 10^6$	0.0072	$26.4 \times 10^7$
ITO/APTES/ProG/Cyt-C Ab/BSA	$1.43 \times 10^6$	0.0041	$28.0 \times 10^7$

### 2.6.3. Electron-transfer rate of Cyt-C at different molecular assemblies

To measure the electron-transfer rate of Cyt-C at the different immunolayer assemblies, a modulated potential with a 10 mV amplitude at the formal potential (-10

mV) was applied with the frequency ranging from 1 Hz to 45 Hz. A Cyt-C solution at a concentration of 100 nM was used for all the experiments in this section. For each layer on the SM-EA-IOW the total electrical impedance and the out-coupled optical signal under synchronous detection, as described in Figure 2-2, with and without the redox-active Cyt-C protein in the flow-cell were measured. Figure 2-7(a) represents the optical response plotted in the complex plane measured by the SM-IOW platform, each data point corresponds to a particular modulation frequency of the AC applied potential, which increases clockwise from the smallest (1 Hz) to the largest (45 Hz). Figure 2-7(b) corresponds to a zoom of the collected baseline optical response. It is noticed that each layer has an effect on the charge transfer resistance of the surface, this can be concluded from the decrease in the baseline optical absorbance amplitude as more layers are added to the surface. Such decrease confirms the successful functionalization of the SM-EA-IOW with the immunoassay bio-interphases.

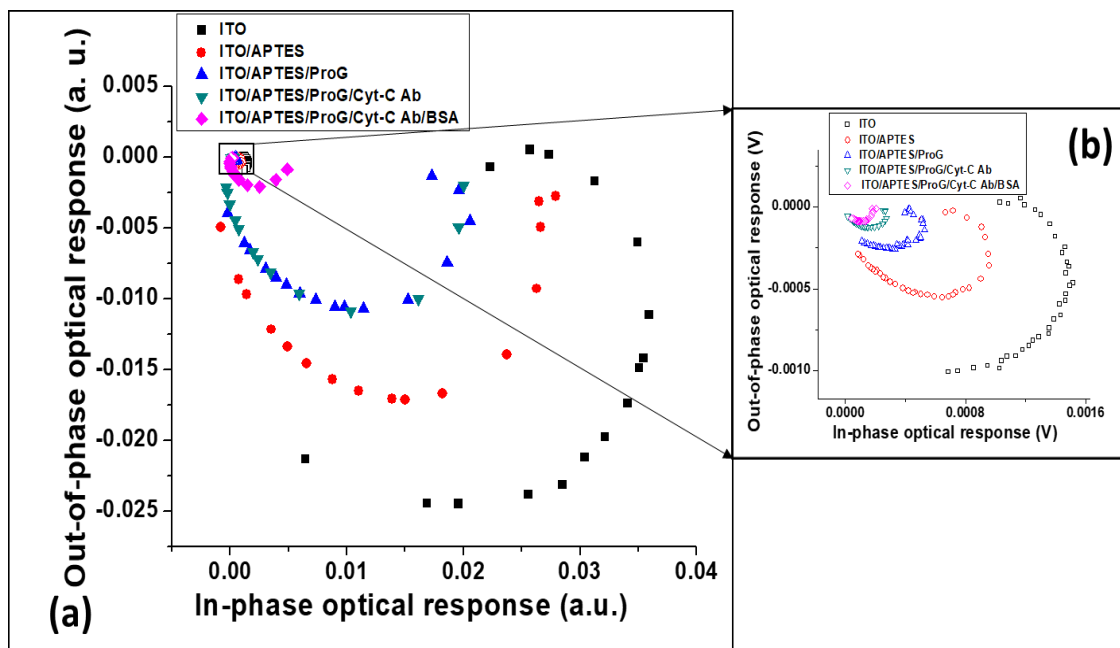


Figure 2-7: (a) Representation the optical response in the complex plane of Cyt-C at different functionalized SM-EA-IOW surface. (b) Data from the baseline measurement at different functionalized SM-EA-IOW surface, zoomed from the highlighted data presented in Figure (a).

The optical data presented in Figure 2-7 allows the use of the parametric plot of  $y(\omega)$  against  $x(\omega)$  as described in section 2.4.1 and the results are shown in Figure 2-8(a). The slope of the linear fit can provide the electron-transfer rate,  $k_{ET}$ , of the faradaic process. Figure 2-8(b) represents the natural logarithm of  $k_{ET}$  for Cyt-C proteins for each of the immunolayers.

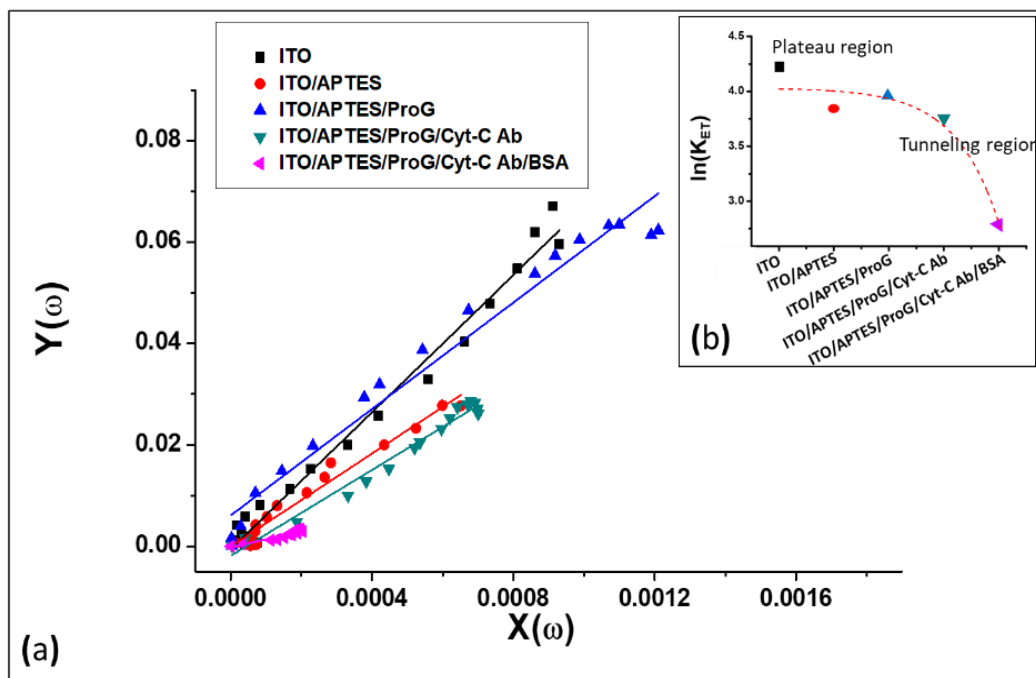


Figure 2-8: (a) The parametric plot of  $y(\omega) = k_{ET} x(\omega)$  with the linear fitting used to retrieve the electron-transfer rate at each functionalized SM-EA-IOW surface. (b) Natural logarithm of the electron-transfer rate plotted at each different functionalized surface of the SM-EA-IOW, where the plateau and tunneling regions are indicated.

Based on the results in Figure 2-8(b) one can infer the following observations: First, measured changes and decrease in electron-transfer rate of Cyt-C indicate that each layer act as a barrier for the electron-transfer process between the Cyt-C proteins and the electrode surface; such effect was also confirmed in results shown in Figure 2-5(c).

Second, compared to ITO/APTES functionalized surface, the molecular ensemble ITO/APTES/ProG is thicker than ITO/APTES; still the electron-transfer rate of Cyt-C proteins is higher with ProG present, this small electron-transfer rate dependence on thickness indicates a plateau region behavior at ITO, ITO/APTES and ITO/APTES/ProG layers. Also, as discussed previously in result summarized in Table1, the binding affinity between Cyt-C and ITO/APTES/ProG is 15 fold higher than the binding affinity between Cyt-C and ITO/APTES, this difference in the strength of interaction most likely led to the higher electron-transfer rate of Cyt-C with ProG present; this effect is similar to the schematic illustrated in Figure 2-3. Such dependence of electron-transfer rate on the strength of interaction between Cyt-C and the functionalized immunolayers in the plateau region does not support the simple conformational electron-transfer mechanism.

Third, as shown in Figure 2-8(b) for thicker molecular assemblies, ITO/APTES/ProG/Cyt-C Ab and ITO/APTES/ProG/Cyt-C Ab/BSA layers, an exponential decay for the electron-transfer rate of Cyt-C proteins was observed. Such fast exponential decay indicates an electron-transfer tunneling mechanism through those layers. It is also noticed that the largest drop among all electron-transfer rates was upon adding BSA onto the layers. Since BSA is used to block nonspecific adsorption, it is expected to have small effect on the thickness of the functionalized immunolayer assemblies [93], therefore the drop in the electron-transfer rate of Cyt-C proteins upon

using BSA indicates the possibility of two scenarios. The first one suggests that BSA will block defects and will prevent nonspecific adsorption of Cyt-C proteins onto such defects present on the functionalized SM-EA-IOW platform, and since the electron-transfer rate is measured on an ensemble average basis the results will be an average of both the electron-transfer rate of the specific and nonspecific adsorbed Cyt-C proteins. Then upon adding BSA the contribution of nonspecific will be eliminated, as illustrated in Figure 2-9(a). The second scenario suggests that adding BSA on the functionalized immunolayers may result in more compact functionalized layers [82], as presented in Figure 2-9(b), such compact layers can lead to an additional barrier and further prevent an effective electron-transfer pathway, resulting in a drop in the electron-transfer rate, in a case similar to the transition curve presented in Figure 2-4.

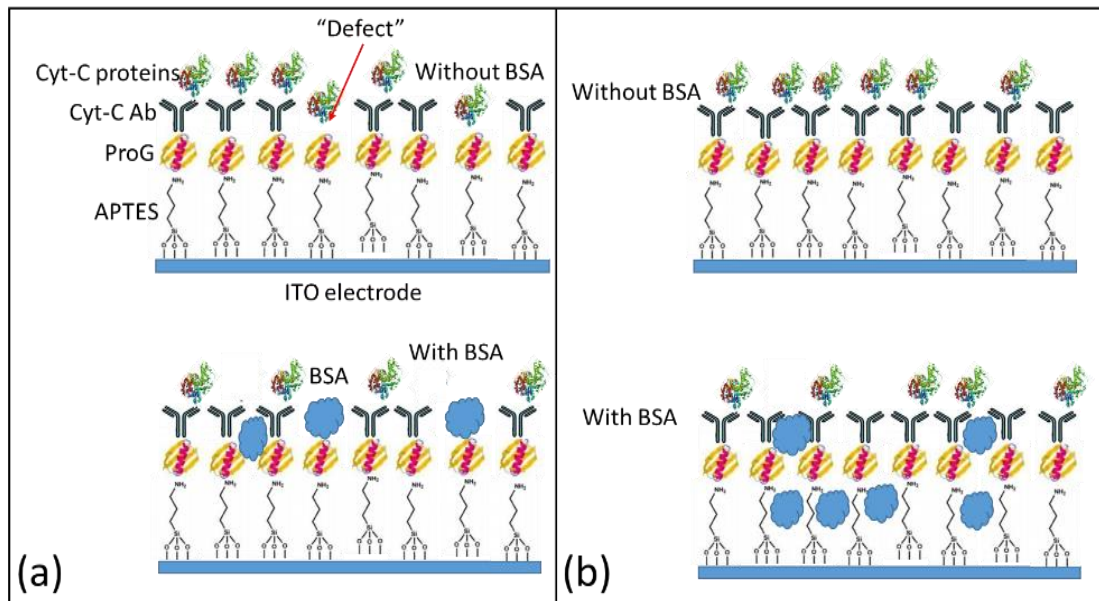


Figure 2-9: Schematic illustrate the possible role of BSA on the electron-transfer process. (a) Without BSA, Cyt-C may penetrate to a defect state and contribute to the electron-transfer rate, such defects are blocked when BSA is added. (b) The

functionalized layers are uniform that adding BSA will have negligible effect on the adsorption sites of Cyt-C on the SM-EA-IOW surface, in this case BSA forms more compact layers, which may result in blocking an electron transfer pathway. Schematic representations are not to scale.

The later scenario is more probable, such conclusion is based on the comparison shown in Figure 2-10, as discussed previously where small change has been noticed on the surface coverage and the equilibrium rate constant with and without BSA despite the drop in electron-transfer rate. Such small change in surface coverage suggests that the chance to have defects on the functionalized SM-EA-IOW is small and the functionalized bio-immunolayers form a dense, complete, and homogeneous morphology of the functionalized layers on the SM-EA-IOW device surface, which also was confirmed from confocal images discussed and shown in Appendix 5.

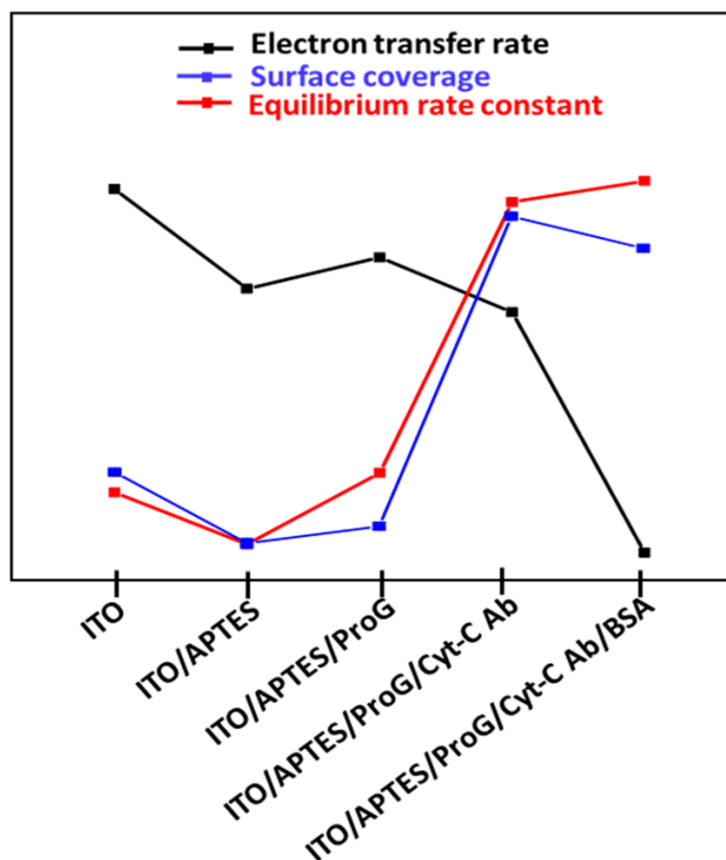


Figure 2-10: Comparison of the behavior of surface coverage, equilibrium rate constant and electron transfer rate of Cyt-C proteins at different functionalized layers. Data shown are not to scale, it is just to compare the effect of BSA upon adding to the bio-immunolayers.

## 2.7. Conclusions

It was demonstrated that the high sensitive SM-EA-IOW can be used to address several phenomena of the redox active molecules adsorbed on modified electrodes, such as mechanisms of electron-transfer rate, molecular binding and affinity strength. The kinetics and mechanism of charge-transfer processes are often difficult to identify and many aspects of the electron-transfer mechanism on electrodes remain unclear because of



the complex and inhomogeneous character of the adsorbed biomolecular systems. Nevertheless, compared to theoretical studies, the results showed that SM-EA-IOW platform provides a powerful tool to optically detect and quantify the electron-transfer mechanisms of redox species adsorbed on different multilayer stacks. This conformation opens new applications of this extremely sensitive SM-EA-IOW platform not only in fundamental studies of electron-transfer events but also to better bridge the opto-electrical signals measured in bio-sensing.

## CHAPTER 3 INFLUENZA VIRUS DETECTION WITH A FUNCTIONALIZED SM-EA-IOW PLATFORM

### 3.1. Introduction

The ability to drive and detect a redox reaction through different molecular immunolayer assemblies on the SM-EA-IOW and the application to retrieve electron-transfer rate were described and confirmed in Chapter 2; such assurance opens the possibility for using this highly sensitive device under electro-optical interrogation in biosensing. In this chapter, the development of a novel immunosensor-based strategy for direct detection of important viral pathogens based on sandwich bioassays incorporated on the SM-EA-IOW for immunosensing is described. Using a redox probe, the faradaic current of the electron-transfer process between the redox probe and the working electrode is reconstructed by the optical signals which serves as a finger print for the sensing methodology. The focus in this chapter is on the detection and identification of the influenza A virus H5N1 to demonstrate the capabilities of the SM-EA-IOW platform for the detection and quantification of bio-agents. More specifically, the detection of the hemagglutinin protein (HA) from the H5N1 virus was deployed.

## 3.2. Bio-Sensing with the Functionalized SM-EA-IOW Platforms

### 3.2.1. The strategy of using SM-EA-IOW for immunosensing

The sensing strategy using SM-EA-IOW is illustrated schematically in Figure 3-1.

The strategy is based on a sandwich immunoassay approach, which starts with the functionalization of the SM-EA-IOW with a capturing Ab aimed to a specific target analyte. Once the target analyte is bond to the SM-EA-IOW interface, it promotes the binding of a reporter Ab labeled with a redox-active probe that will be electrochemically modulated on the SM-EA-IOW platform to provide the probing optical signal.

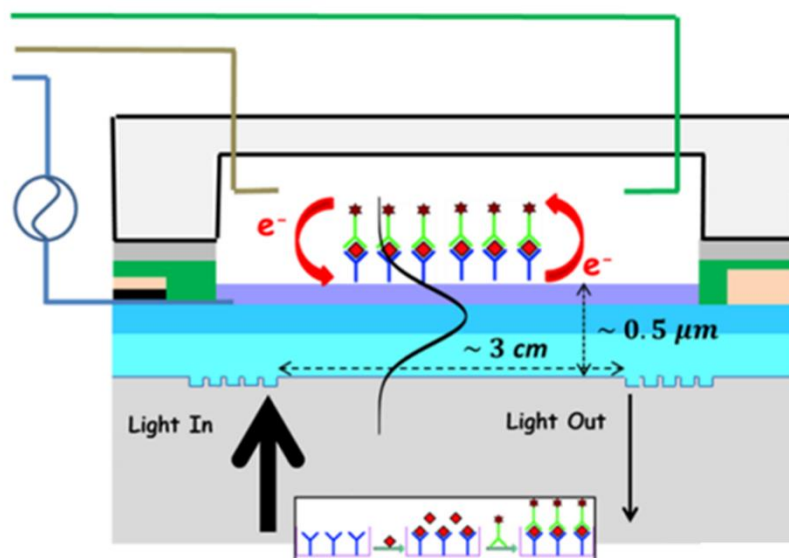


Figure 3-1: Spectroelectrochemical immunoassay detection with impedance and AC voltammetry optical measurements on SM-EA-IOW platform. Inset: Steps of the sandwich bioassay with the bonded Ab, the binding of the biological target, and finally the secondary Ab with a redox-active optical tag.

### 3.2.2. Conjugation of a redox probe to a secondary antibody reporter

To form the transducing electro-optical signal that can be incorporated onto the SM-EA-IOW for sandwich immunoassay based detection, as illustrated in Figure 3-1, a redox-active molecule that can be conjugated onto the reporting secondary Ab is an appealing route. A good example of a redox-active probe molecule is methylene blue (MB). MB can be used as a very selective redox tag and has already shown great performance in integrated DNA structure switching sensors [25, 94]. As shown in Figure 3-2, critical spectral properties of MB under redox reaction can be achieved [34, 95], and its spectroelectrochemical analysis of this phenomenon was experimentally realized [96, 97]. The MB dye, which is normally deep blue in color, can be converted to its colorless leuco-form using electrochemical potential modulation. This process is exceptionally reversible and MB features a unique switching change in optical absorbance that can be electrochemically driven through an electric potential modulation; such features of a dye fit the detection strategy using the SM-EA-IOW device described in Figure 3-1.

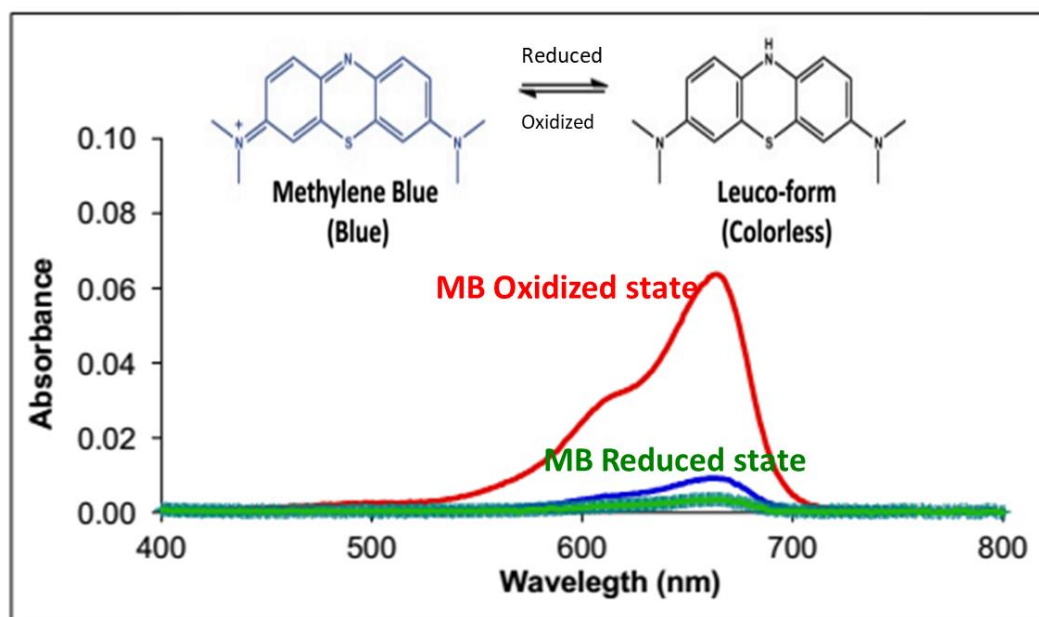


Figure 3-2: 2.4  $\mu$ M MB in its oxidized state (red curve), and reduces state (green) which is colorless. Here the reduction was done chemically by using ascorbic acid 22 mM in the presence of 500 mM HCl.

For labeling the secondary Ab, a derivative of MB with the same reduction spectrum properties that is available as NHS-ester was purchased from Biosearch Technologies (MB-1000S-5, 5 mg, molecular weight = 598.12 g/mol). Such material features a carboxylic acid functionality for direct coupling to amino groups of antibodies and proteins. As mentioned previously, the targeted antigen is hemagglutinin protein (HA) from the H5N1 virus, for that a secondary polyclonal Ab for the influenza A H5N1 to serve as a reporting probe was purchased from Santa Cruz Biotechnology (sc-54958, 20  $\mu$ g/mL, 1 mL, molecular weight = 144 kDa, goat polyclonal IgG) and conjugated with MB ester. As illustrated in Figure 3-3(a) the conjugation process began by mixing the secondary H5N1 Ab with the MB ester dye for two hours at room temperature. A protein labeling kit (A10235, Thermo Fisher Scientific) was used for the conjugation of the secondary H5N1 Ab with the MB ester, then the conjugated secondary H5N1 Ab was purified by using a resin column and a PBS solution as elution buffer. The concentration of MB-labeled H5N1 Ab and the degree of labeling were determined based on UV-Vis absorption spectroscopy (Figure 3-3(b)). Also in Figure 3-3(b) the spectrum shows a direct comparison of the absorption spectra of MB-ester dye (blue curve) and the same amount of dye conjugated to the secondary H5N1 Ab (red curve). A shift in the UV-Vis spectrum was observed, which indicates the successful labeling procedure of the secondary Ab with the MB-ester dye. The degree of labeling (details in Appendix 6)

which provides the average number of dye molecules coupled to Ab protein molecules was determined to be about 1.

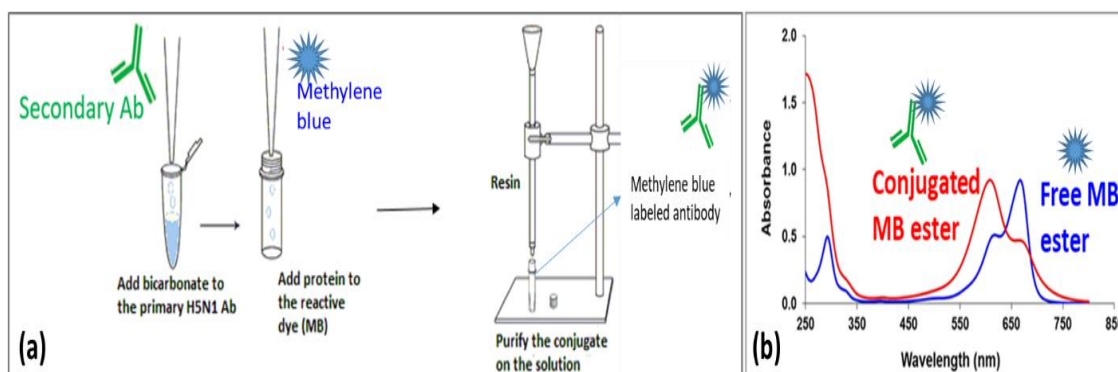


Figure 3-3: (a) Strategy for conjugating secondary Ab with methylene blue ester. (b) Experimental evidence of the aimed conjugation.

### 3.2.3. Preliminary tests with the MB-labeled H5N1 secondary antibody

The first step was to make sure that the MB-labeled H5N1 secondary Ab have similar reduction spectrum properties as the pure MB-ester. The activity of the reduction of the MB-labeled H5N1 secondary Ab was confirmed using chemical reduction process, results shown in Figure 3-4 support that the oxidation reduction process of the labeled secondary Ab is still active.

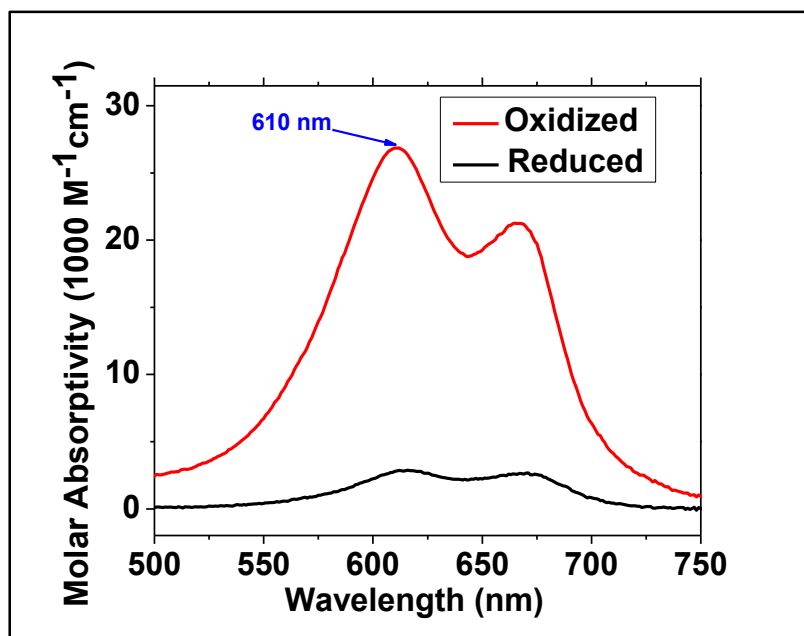


Figure 3-4: Spectral molar absorptivity of methylene blue ester after conjugation with the secondary Ab at different oxidation states. The reduction was done chemically by using ascorbic acid 22 mM in the presence of 500 mM HCl.

Next the oxidation reduction reversibility of the MB-labeled H5N1 secondary Ab adsorbed onto ITO/APTES functionalized SM-EA-IOW surface under CV potential modulation was tested. First, the optical baseline signal under CV scan (20 mV/s) was obtained. Then the ITO/APTES surface was functionalized with MB-labeled H5N1 secondary Ab, with a concentration of (10  $\mu\text{g/mL}$ ), by injecting 2 mL of the labeled Ab sample into the flow-cell and let it incubate for one hour before being rinsed with PBS. With the MB-labeled H5N1 secondary Ab being adsorbed onto ITO/APTES surface the optical signal under CV scan was recorded. With the baseline and optical signal known, the absorbance of the adsorbed MB-labeled H5N1 secondary Ab was measured.

Then after cleaning the SM-EA-IOW following the cleaning process described in chapter 2, the absorbance under CV scan of the MB-labeled secondary H5N1 Ab

adsorbed onto ITO/APTES/ProG SM-EA-IOW surface was measured, here the functionalization of MB-labeled secondary H5N1 Ab and data collection was the same as mentioned above for ITO/APTES.

The experimental results in Figure 3-5 shows the oxidation reduction reversibility of the MB-labeled H5N1 secondary Ab, also the results confirm the transduction capability of the SM-EA-IOW platform to detect the electron transfer events of the probe as it is incorporated to the device surface (results shown after rinsing the flow-cell). One also can notice a substantial drop of the redox signal in the presence of ProG, due to such substantial drop the ProG layer was not included in the final immunoassay for the H5N1 antigen detection.

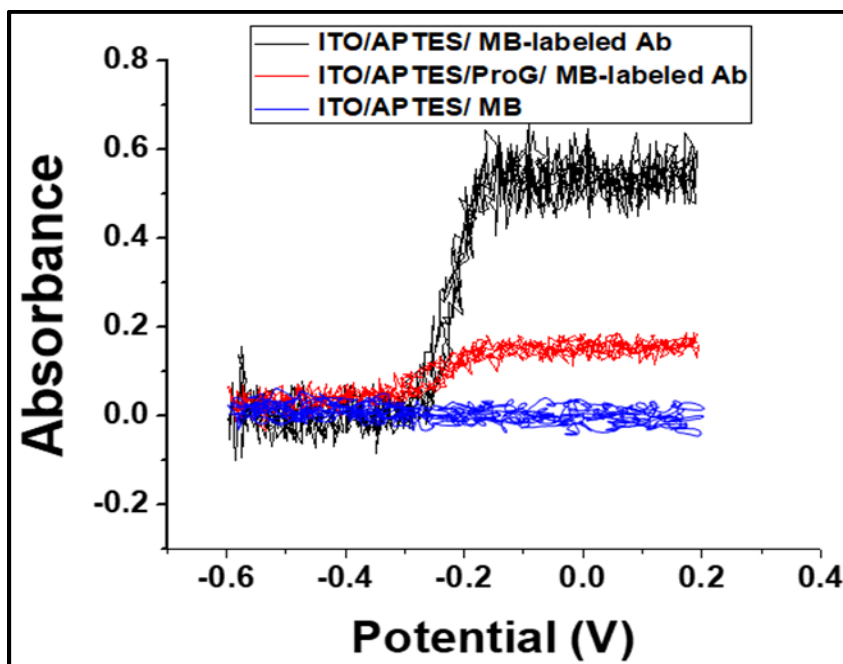


Figure 3-5: Absorbance data as measured by the SM-EA-IOW device with a wave-guided light at 637 nm for an adsorbed sub-monolayer of the MB-labeled secondary H5N1 Ab (black and red) and an adsorbed sub-monolayer of the MB (blue trace) undergoing CV potential modulation on different SM-EA-IOW surface.



Another test was performed to evaluate the direct interaction and binding activity of MB-labeled secondary H5N1 Ab. Taking advantage of the fluorescence property of MB [98] the fluorescence signal was collected from the surface of the SM-EA-IOW platform using the experimental setup illustrated in Figure 3-6(a). As shown in Figure 3-6(b) the detected fluorescence signal was stable and strong even after rinsing the flow-cell. However, when a pure MB species was injected into the flow-cell (without any Ab conjugation) with 300 nM concentration, the fluorescence signal disappeared after rinsing the flow-cell with 20 mL of PBS solution as shown in Figure 3-6(b) which is consistent with the absorbance measurements under CV scan shown in Figure 3-5 (blue trace). Those results were also confirmed by confocal imaging of both samples with pure MB (Figure 3-6(c)) and the MB-labeled secondary H5N1 Ab (Figure 3-6(d)), such results confirm that the conjugation between MB and the secondary H5N1 Ab did not affect the functionality and reactivity of the secondary Ab.

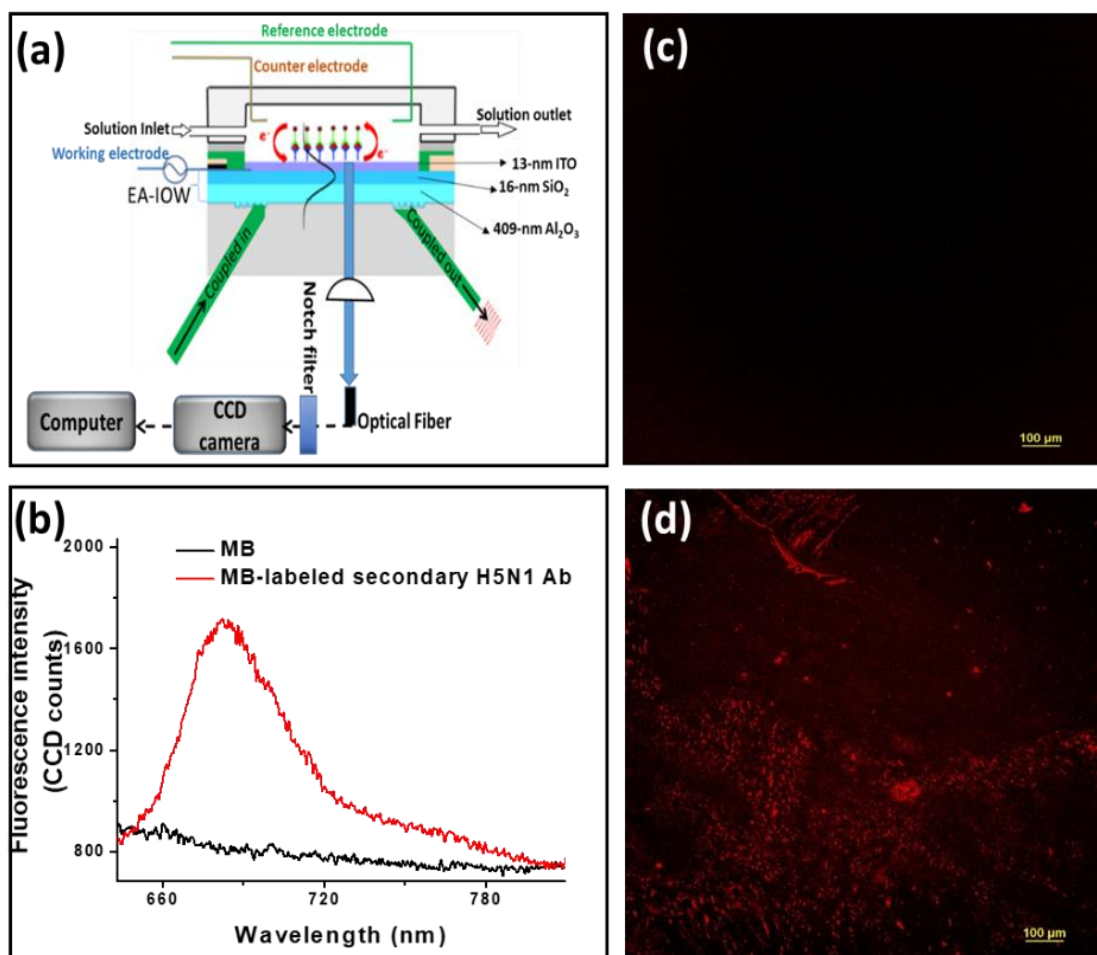


Figure 3-6: (a) Experimental setup for fluorescence data collection from the surface of the SM-EA-IOW, the setup included a monochromator connected to CCD camera for spectrally resolved measurements. (b) Fluorescence signal detected from the SM-EA-IOW platform functionalized with ITO/APTES after incubation of MB-labeled secondary H5N1 Ab (red curve) and native MB (black curve), data was collected after rinsing the flow-cell. (c) Confocal image of the SM-EA-IOW surface with adsorbed MB and (d) with adsorbed MB-labeled secondary H5N1 Ab. Confocal images (c) and (d) were acquired under same conditions and parameters, and after sonication of the SM-EA-IOW device in DI water for 10 minutes.

### 3.3. Virus Protein Detection with Immunoassay on the SM-EA-IOW Device

After successfully conjugating the MB-ester to a secondary H5N1 Ab to form the probing reporting signal, the detection of the H5N1 virus antigen using the SM-EA-IOW device was performed.

#### 3.3.1. Influenza antigen sandwich immunoassay functionalization protocol

The buildup of a sandwich immunoassay for detecting hemagglutinin (HA) protein from the H5N1 avian influenza A virus using the SM-EA-IOW platform was adopted as follow. First, a monoclonal anti-H5 (H5N1) Ab that served as the capturing Ab was purchased from Santa Cruz Biotechnology (ab82455abcam, 250  $\mu$ g, 2 mg/mL) and bound to the functionalized APTES SM-EA-IOW interface by injecting a solution with a concentration of 2  $\mu$ g/mL into the flow-cell, this concentration was chosen in accordance to the characterization done in chapter 2 for Cyt-C Ab functionalization. After functionalization with the capture Ab for approximately one hour, the flow-cell with the SM-EA-IOW device was thoroughly rinsed with a PBS solution to remove unbound species from the SM-EA-IOW interface. Then, recombinant influenza A hemagglutinin (HA) of the H5N1 influenza virus solution (H5N1 HA(P-20) P:(sc-54958P, 200  $\mu$ g/mL, 0.5 mL)), purchased from Santa Cruz Biotechnology, was injected into the flow-cell and allowed to adsorb to the surface bounded capturing antibodies for one hour before rinsing again with PBS. Finally, a MB-labeled polyclonal secondary H5N1 Ab solution with a concentration of 10  $\mu$ g/mL was injected into the flow-cell and let bind to the virus protein species residing on the SM-EA-IOW surface for one hour, again the flow-cell was rinsed with PBS. The presence of bound MB-labeled polyclonal secondary H5N1 Ab was then interrogated with the SM-EA-IOW device. Virus protein

antigen solutions with different concentrations (200, 100, 20, and 0 ng/mL) were used. After data collection at each specific concentration of the virus protein solution, between each set of measurements the interaction between the capture antibodies and the ITO/APTES surface was reversed by sonicating the SM-EA-IOW device in a potassium carbonate solution (pH 9-11) following the cleaning process described in chapter 2 for easily renewing of the sensing interface.

### 3.3.2. Tests of the SM-EA-IOW platform to monitor the presence of the HA virus protein through the optical signal under CV potential modulation

For data accusation the experimental setup used was the same as described in chapter 2 and shown in [Figure 3-7](#), here the laser beam wavelength deployed was at 610 nm or 633 nm and SM-EA-IOW platforms with a separation distance between the coupling gratings of about 3.4 cm was used.

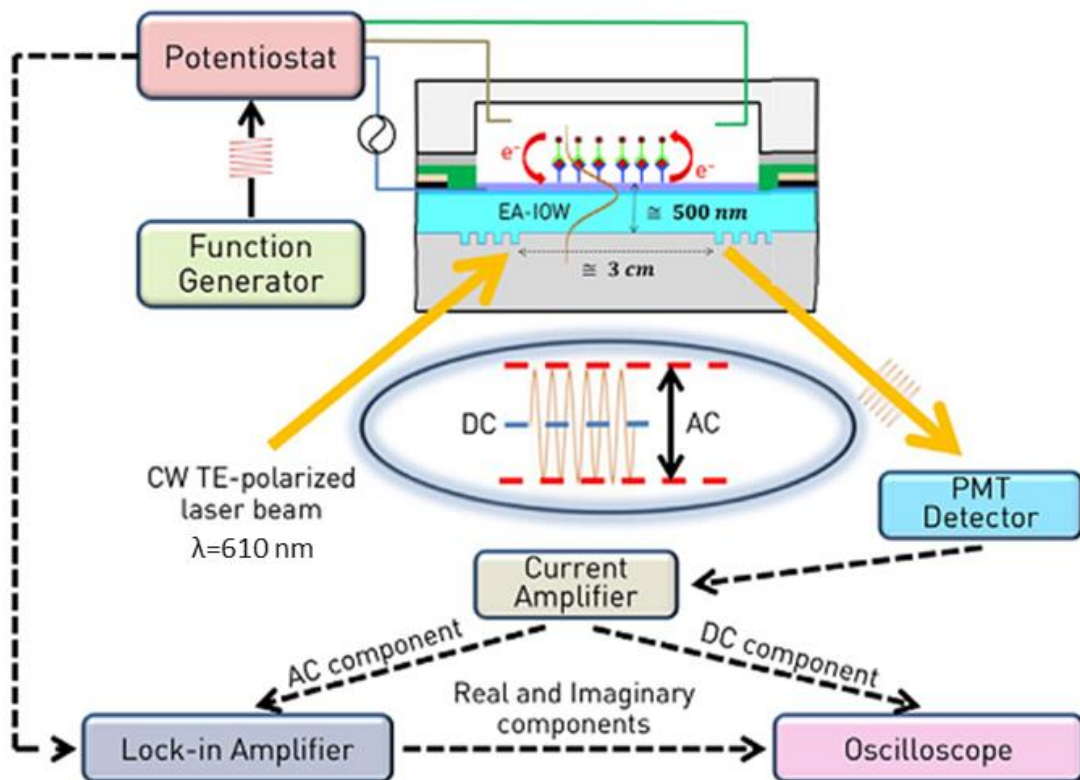


Figure 3-7: Experimental setup for electrical control of the SM-EA-IOW interface.

The optical absorbance data on the SM-EA-IOW device for the sandwich immunoassay of the virus H5N1 protein was first collected under CV potential modulation, the baseline optical signal was collected after adsorption of the influenza virus antigen and the reporter optical signal was collected after incubation of the MB-labeled H5N1 Ab at a concentration of  $10 \mu\text{g/mL}$ . The results displayed in Figure 3-8 represent the absorbance optical data (red trace) collected when the SM-EA-IOW device functionalized with APTES and primary Ab was exposed to HA virus antigen ( $200 \text{ ng/mL}$ ) and MB-labeled H5N1 secondary Ab ( $10 \mu\text{g/mL}$ ). As the applied potential in the CV scans (scan rate  $20 \text{ mV/s}$ ) crosses the formal potential (at about  $-0.2 \text{ V}$ ) of the MB-labeled H5N1 Ab molecule, it triggers an associated optical absorption change (the red trace in Figure 3-8). In addition, from the measured absorbance,  $A$ , the total surface

density of the adsorbed probe species can be determined,  $\Gamma = A/(S \epsilon)$ , where  $S$  is the sensitivity factor of the SM-EA-IOW device (Appendix 3) and  $\epsilon$  is the molar absorptivity of the redox probe obtained from Figure 3-4, such calculation gave a value of  $\Gamma = 388$  fmol/cm<sup>2</sup>. The black trace corresponds to data when the SM-EA-IOW device functionalized under the same protocol mentioned above but in this case it was exposed to just MB-labeled H5N1 secondary Ab (10 µg/mL), and the virus antigen was absent from the solution. The experimental results in Figure 3-8 confirm the ability of the SM-EA-IOW platform to detect the presence and absence of the HA virus protein through spectroelectrochemical changes in the redox probe. Also, the negligible absorbance signal without the virus antigen indicated that non-specific adsorption of the MB-labeled Ab has been kept to a minimum at the functionalized SM-EA-IOW interface.

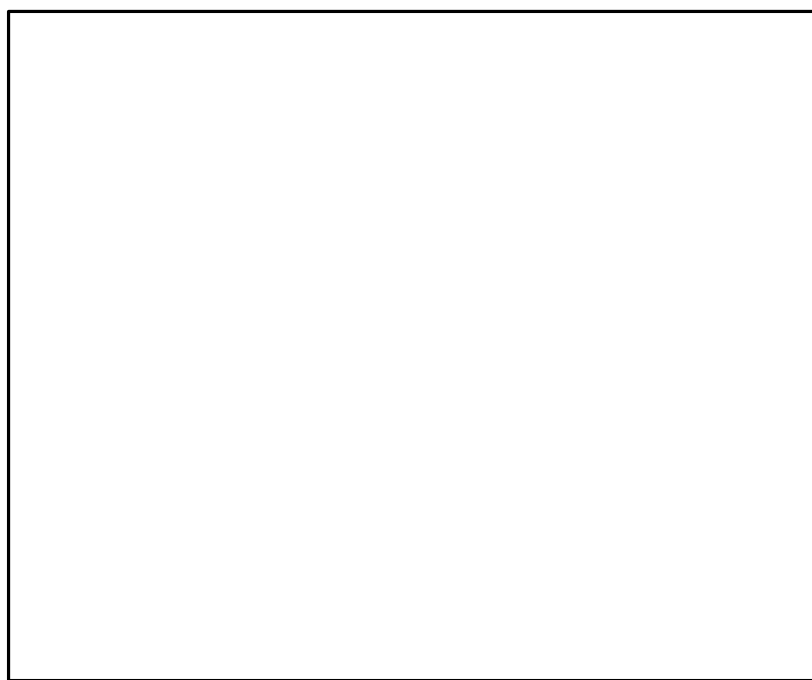


Figure 3-8: Optical absorbance at 610 nm as measured by the SM-EA-IOW platform under CV scans. Red trace in the presence of HA virus antigen and black trace in the instance the virus antigen was absent from the solution.

As another control experiment, the SM-EA-IOW functionalized with capturing antibodies was exposed to a blocking peptide. Then, as described above, the absorbance signal using a wavelength of interrogation at 610 nm was obtained under CV potential modulation after the SM-EA-IOW was exposed to the virus antigen and the MB-labeled H5N1 Ab. Figure 3-9 shows the null results, when a blocking peptide is bound to the capture Ab it prevents the adsorption of both the influenza virus antigen and the secondary MB-labeled H5N1 Ab probe on the device surface (data shown without rinsing the flow-cell). This experimental results confirm the selectivity of the functionalized SM-EA-IOW platform.

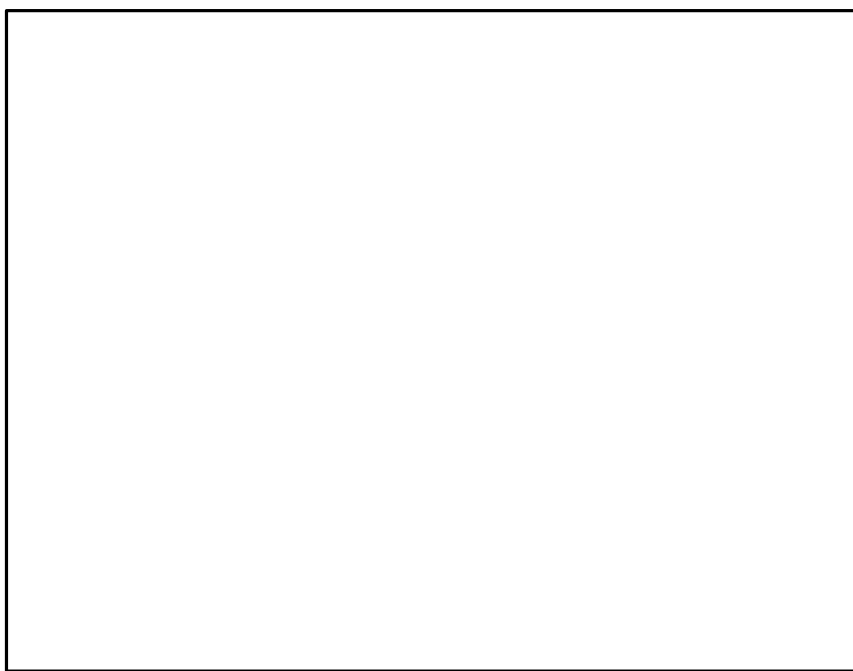


Figure 3-9: Absorbance measured in the presence of a blocking peptide that prevents the antigen adsorption.

A schematic representation that summarizes the results of Figure 3-8 and Figure 3-9 is provided in Figure 3-10. First, Figure 3-10(a) illustrates the results of Figure 3-8 (red trace), where the virus antigen species are present in the immunoassay and the probe

is bound to the device surface and provides a strong analytical response even after rinsing the flow-cell. In contrast, Figure 3-10(b) illustrates the results in Figure 3-8(black trace), where the virus antigen is not present and the probe species are not bound to the surface and the analytical signal vanishes after the flow-cell was rinsed. Figure 3-10(c) illustrates the results of Figure 3-9, where a blocking peptide was used and no redox signal was detected, which indicates that the nonspecific adsorption of the MB-labeled H5N1 Ab on the SM-EA-IOW surface was negligible.

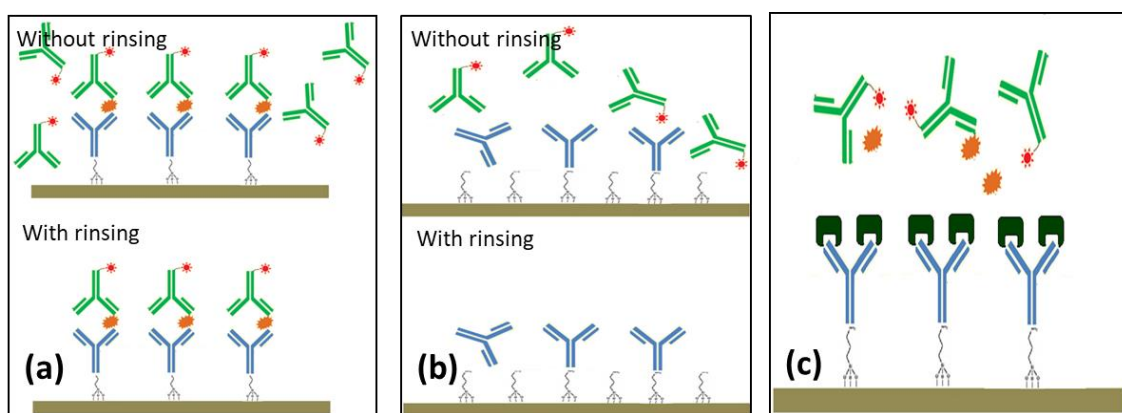


Figure 3-10: Schematic representation of the results in the Figures (3-8 and 3-9) in case (a) MB-labeled H5N1 Ab is adsorbed to the surface in the presence of the target analyte. (b) When the antigen is absent. And (c) in case when a blocking peptide is used.

### 3.3.3. Optical impedance spectroscopy detection protocol

As noticed CV modulation provides a clear and simple identification of the redox process, but as discussed in chapter 2 using AC impedance modulation on the SM-EA-IOW platform in combination with synchronous detection from a lock-in amplifier can improve the signal-to-noise ratio with faster transduction time. Figure 3-11(a) shows the absorbance amplitude signal versus angular frequency of the probe (MB-labeled secondary H5N1 Ab) driven by an AC potential modulation applied to the SM-EA-IOW



surface (potential modulation amplitude = 30 mV, DC bias at the formal potential = -220 mV, laser wavelength = 633 nm) that has been fully functionalized with the immunoassay (ITO/APTES/Primary Ab/Virus Antigen, virus antigen concentration = 200 ng/mL) to detect the virus antigen. The absorbance amplitude was measured by taking the baseline optical signal after adsorption of the influenza virus antigen and the reporter optical signal collected after incubation of the MB-labeled H5N1 Ab with data processing as described in Appendix 1. The corresponding faradaic current density versus angular frequency of the AC modulation mentioned above is displayed in Figure 3-11(b). The results displayed shows a characteristic resonance frequency for the faradaic process with a peak value centered at about 50 rad/sec, such resonant peak frequency is associated with the electron transfer rate of the redox probe present on the electrode surface of the SM-EA-IOW device, which is helpful when a potential AC voltammetry modulation technique is applied.

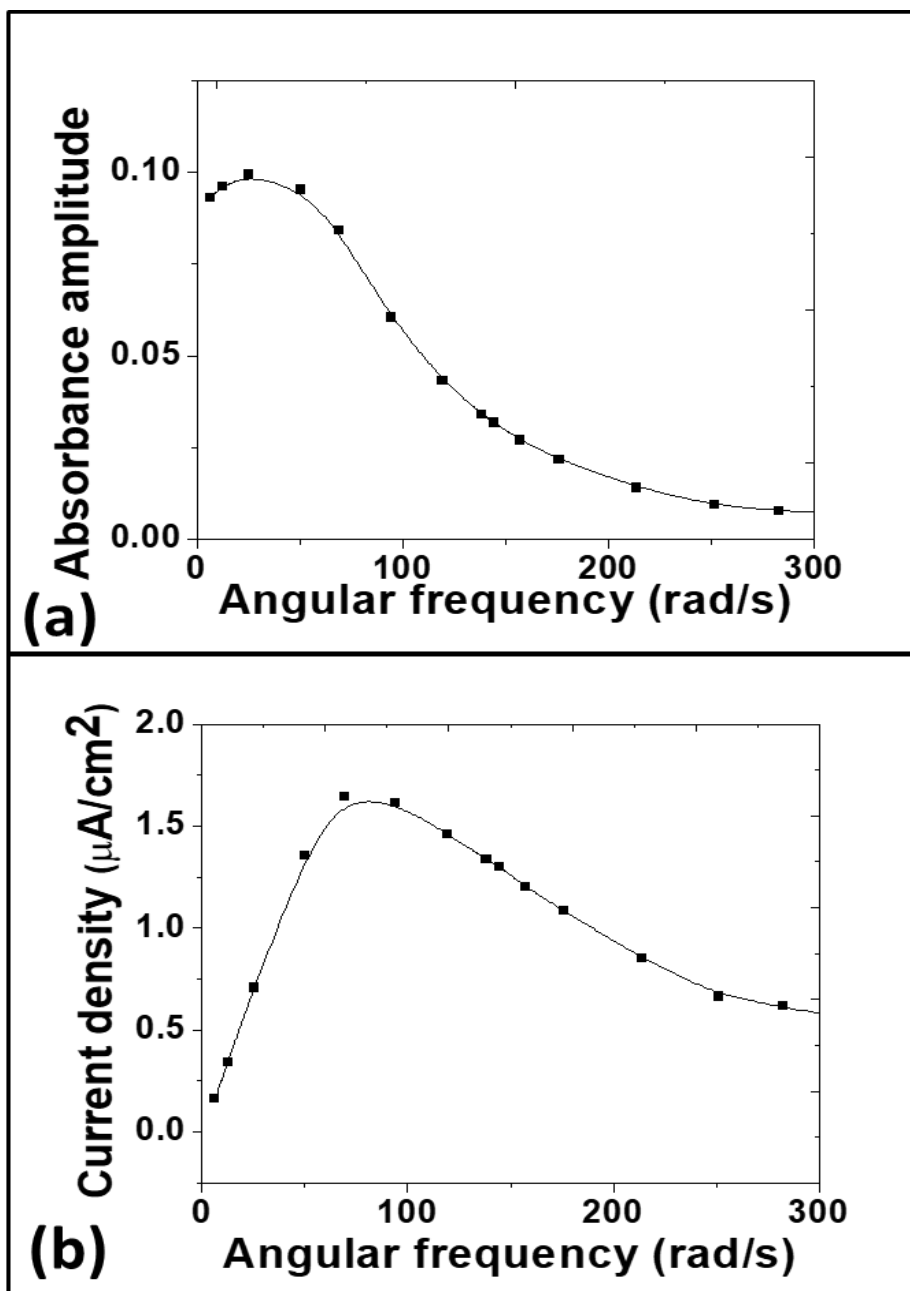


Figure 3-11: (a) The corresponding absorbance amplitude of MB-labeled H5N1 Ab driven by an AC potential modulation measured by the SM-EA-IOW device. (b) Corresponding faradaic current density versus angular frequency for the AC potential modulation results in (a).

#### 3.3.4. AC voltammetry detection protocol and limit of detection

Once the modulation frequency that maximizes the faradaic current of the redox probe has been experimentally determined, an AC voltammetric technique was applied at different DC bias potential while optical data was collected with the SM-EA-IOW platform. For device applications, AC voltammetry is a more robust transduction scheme to operate the platform as it is not time consuming and much more immune to noise due to the frequency filtering capability provided by a lock-in amplifier that reads the modulated AC signal. Briefly, a sinusoidal potential modulation was applied on the SM-EA-IOW device (amplitude of 30 mV, modulation angular frequency 50 rad/sec) with varied DC bias potential over a range of (-360 mV to +40 mV) that encompasses the formal potential of the redox process of the probe MB-labeled H5N1 Ab. The absorbance amplitude at each DC potential was measured by taking the baseline optical signal after adsorption of the influenza virus antigen and the reporter optical signal collected after incubation of the MB-labeled H5N1 Ab with data processing as described in Appendix 1. As shown in Figure 3-12 for different virus antigen concentration, a plot of the faradaic current density (y-axis) against the DC bias potential measured (x-axis) from the absorbance modulated amplitude displays a peak intensity around -170 mV, which corresponds to the redox activity of the MB-labeled H5N1 Ab over the functionalized SM-EA-IOW surface. As the DC bias potential is set away from the formal potential (away from -170 mV) of the targeted probe, the analytical signal decreases towards zero. The peak intensity of the faradaic current density reported by the redox probe under the AC voltammetry is proportional to bounded surface concentration

of the target antigen and provides a direct route to the detection and quantification of the virus analyte.

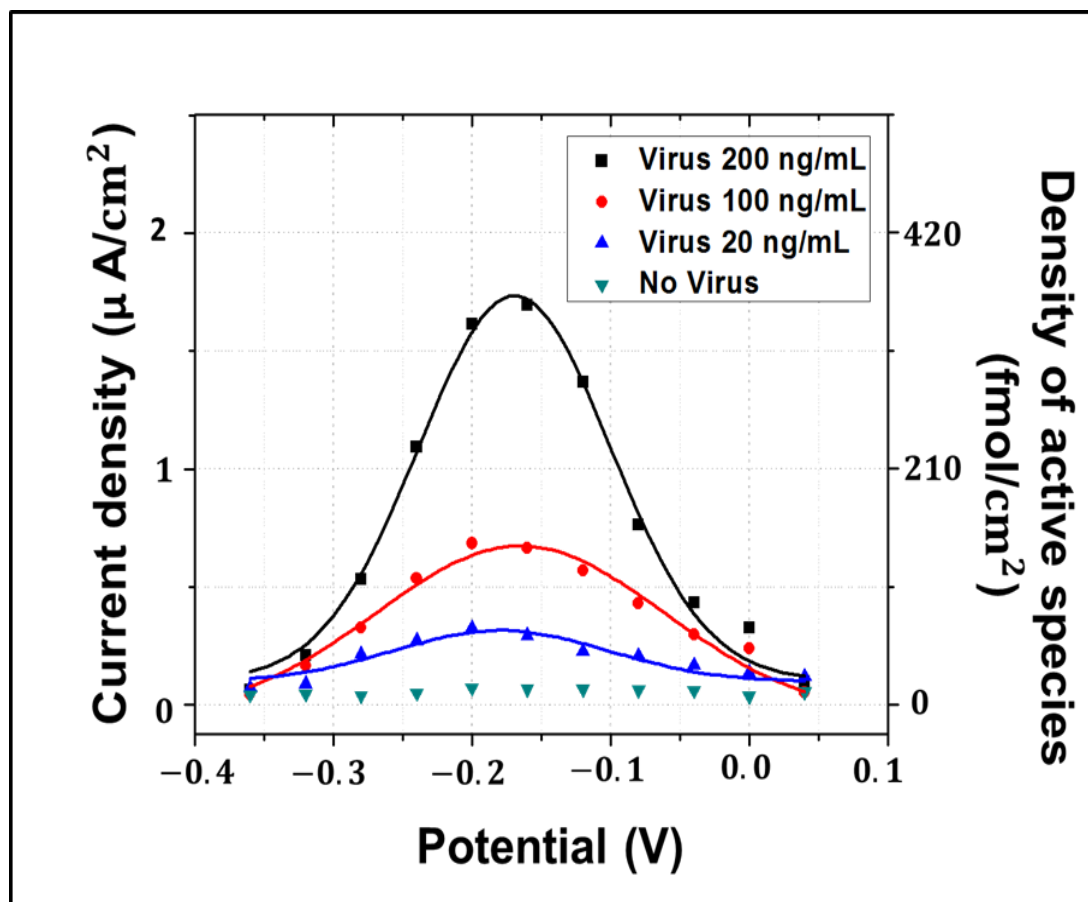


Figure 3-12: Faraday current density from the redox probe (MB-labeled secondary H5N1 Ab) for different volume concentrations of the virus antigen.

From the AC voltammetry data above, a plot of the corresponding peak intensity of the current density at different virus antigen concentrations was used to determine the limit of detection, as shown in Figure 3-13. An experimental limit of detection was determined using a standard 3-sigma to be about 4 ng/mL which corresponds to 77 picomolar (pM) for the virus antigen under test using the SM-EA-IOW platform. Such preliminary experimental results for the influenza A (H5N1) HA protein have reached an

outstanding level of detection, even though several features can still be optimized in this technology to further improve device performance. Nevertheless, such limit of detection figure already surpasses several technologies currently being used (e.g., see Appendix 7).

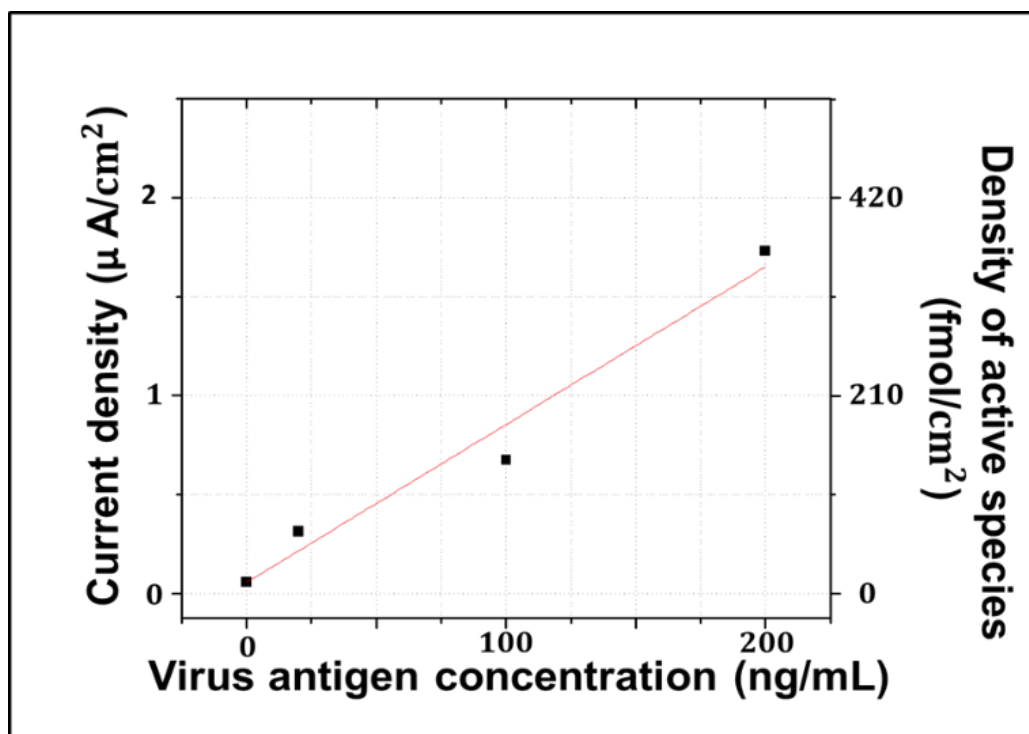


Figure 3-13: Maximum of the faradaic current density for each volume concentration of virus antigen, which allows to determine the limit of detection.

### 3.4. Conclusions

Results showed successful combination of the high sensitivity single-mode SM-EA-IOW platform with a biologically specific sandwich immunoassay to demonstrate a novel strategy for pathogen analysis. Due to the extremely high sensitivity of the conductive and transparent photonic device, a remarkable limit of detection was experimentally demonstrated for an influenza virus antigen when using a highly selective probe that is biologically specific through the Ab/antigen binding affinity. Equally

important, the transduction mechanism of the bio-photonic device is also highly selective, as the monitored analytical signal is optically and electrochemically locked to the probe tailored for the antigen detection. It is optically locked by using a laser wavelength that is tuned to the optical transition associated with the conjugated redox probe. And it is electrochemically locked by modulating the applied potential at the formal potential of the targeted redox probe events. And it is also confined to surface events next to the electrode interface through confinement of the electromagnetic radiation along the electroactive optical waveguide. The redundancy of these selective factors is expected to minimize unwanted false signals from interferons invariably present during detection with biological specimens. The advances described here have the potential to create a new bio-sensing technology capable of offering substantially shorter detection times with simpler and more cost-effective protocols, which are critical for point-of-care applications in disease diagnostics. Moreover, the specific focus on influenza antigen should not obscure the versatility of the technology that can be adapted for detection of a variety of pathogens even in clinical samples.

## CHAPTER 4 DETECTING TARGETED BACTERIA IN AUTHENTIC CLINICAL SAMPLES USING SM-EA-IOW PLATFORMS

### 4.1. Introduction

The capability of the SM-EA-IOW device presented in chapter 3 is remarkable as an impressive limit of detection has been reached by means of a highly selective probe. This probe is biologically specific through the antibody/antigen binding affinity and detection can be performed at a relatively short period of time. However, the samples of the influenza virus antigen previously described were prepared under special laboratory conditions. In this chapter, authentic clinical samples from patients of a rapidly progressive and potentially catastrophic infectious disease of the eyes, endophthalmitis, was targeted for detection using the SM-EA-IOW platform. Early diagnosis of endophthalmitis is key for its proper treatment [99]. More specifically, gram-negative bacteria in those clinical samples were targeted using the SM-EA-IOW and results were compared with polymerase chain reaction (PCR) tests. The ability to test clinical samples using the SM-EA-IOW platform has the potential to advance the bio-sensing technology as it offers substantially shorter detection times, more cost effective protocols, and simpler operating procedures, which are all critical characteristics needed for point-of-care sensing applications.

## 4.2. Motivation and Strategy for Clinical Sample Detection using SM-EA-IOW

### Platforms

A significant challenge for the treatment of any infectious, and specifically bacterial-related diseases, is to ensure and quantify the cause via appropriate sensing and monitoring techniques in real-time evaluation [100]. Although advanced techniques in microbiology, e.g., culture and PCR techniques, [Figure 4-1](#) upper left and right respectively, have been used to diagnose infectious bacteria diseases, they still lack the ability to detect microorganisms in real-time or on-site [101-103]. Therefore, there is an unmet need for rapid, direct, and portable bio-sensing methods to evaluate in real-time such infectious diseases.

Towards applications targeting genuine clinical samples with the SM-EA-IOW bio-sensing platform similar steps as previously described had to be followed. As before, the photonic surface had to be functionalized with a specific antibody to act as the capturing component for the aimed analyte that causes a particular infection; here the gram-negative bacteria ([Figure 4-1\(b\)](#)) was targeted. The detection strategy deployed for the real clinical sample is based on the same methodology described in chapter 3. Briefly, a laser beam is coupled onto the SM-EA-IOW device and optical data is collected throughout the experiment before and after injecting a MB-labeled Ab that is specifically designed as a signal reporter for the gram-negative bacteria. The presence of the targeted bacteria in the analytical sample is expected to result in their capture onto the SM-EA-IOW surface which promotes binding events of the MB-labeled Ab onto the device interface. The out-coupled laser beam is collected for measuring the optical absorbance under AC voltammetry, which creates a time-effective protocol with better



SNR for detection and a characteristic peak at the formal potential of the redox probe is expected to be observed as the finger print for the targeted bacteria (Figure 4-1(c)).

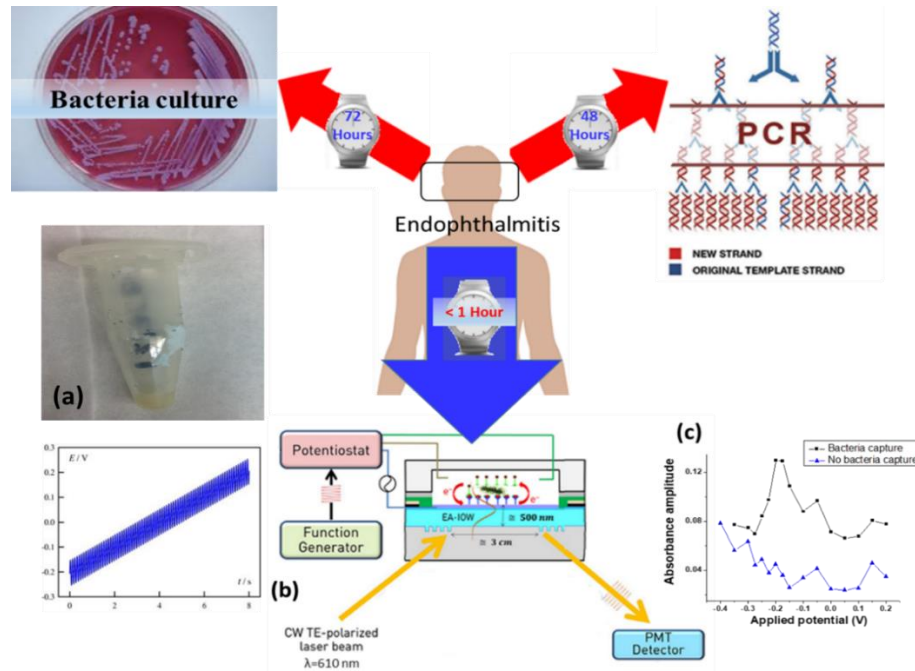


Figure 4-1: Schematic representation of three different bacteria detection methodologies: culturing techniques (upper left), PCR-based methods (upper right), and the proposed SM-EA-IOW optical immunosensor (bottom). Note that the time indicated for each method refers to the total estimate assay time. (a) Clinical samples of aqueous and vitreous humor from the eyes of patients in the range of 100  $\mu\text{L}$ . (b) Specific capture antibodies immobilized onto the SM-EA-IOW surface for the gram negative and MB-labeled gram negative Ab. The bacteria cell fragments are captured onto the antibody-modified SM-EA-IOW surface that is then exposed to the specific MB-labeled Ab, and the modulated absorbance is measured under a modulated AC voltammetry. (c) Absorbance measured from the SM-EA-IOW provides the monitored optical signal. Peak at the formal potential in the absorbance curve is correlated to the presence of the targeted bacteria onto the sample.

#### 4.3. Functionalization Protocol of the SM-EA-IOW for Gram-Negative Targeted Bacteria and Preliminary Tests of the Immunoassay

First, the ability of the SM-EA-IOW device to detect gram-negative bacteria was tested. For this purpose, a sample of a gram-negative endotoxin from *E. Coli* K12 bacteria was prepared and tested (more details on sample preparation can be found in Appendix 8). The functionalization protocol of the SM-EA-IOW was the same as previously described in chapters 2 and 3; however, here the functionalized immunoassay is for gram-negative bacteria detection as illustrated in Figure 4-2. Since for diagnostic testing with clinical samples the amounts of available material is limited in volumes of about 150  $\mu\text{L}$  or less, the flow-cell was redesigned to have a capacity of less than 70  $\mu\text{L}$  in solution volume. After the SM-EA-IOW surface was functionalized with APTES, the SM-EA-IOW device was mounted into the electrochemical flow-cell and the ITO/APTES interface was in situ functionalized with capturing antibody species by injecting a solution of monoclonal antibody gram-negative endotoxin (anti-gram-negative endotoxin antibody (clone B40/22) LS-C56151, LSBio Inc.) at a concentration of 2  $\mu\text{g/mL}$ . After incubation of the SM-EA-IOW device with the capturing antibody solution for approximately 20 minutes, the flow-cell was thoroughly rinsed with a PBS solution to remove unbound species. Next, a solution containing the targeted bacteria was injected into the flow-cell and allowed to bind to the capturing antibodies already immobilized on the device surface before rinsing again with PBS. Finally, a secondary lipopolysaccharides (LPS) polyclonal endotoxins Ab (anti-lipopolysaccharide (LPS) antibody LS-C71709, LSBio) at a concentration of 10  $\mu\text{g/mL}$  that was already labeled with the MB redox-active probe (conjugation details summarized in Appendix 9) was

injected and incubated in the flow-cell for around 20 minutes before the cell was rinsed again.

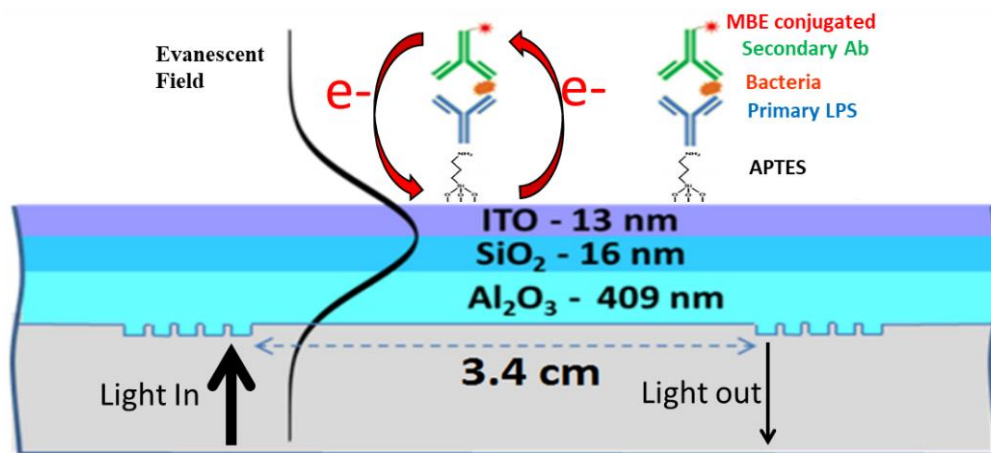


Figure 4-2: Structure of the multilayer, the SM-EA-IOW device functionalized with a sandwich bioassay: an APTES monolayer, covalently bounded primary (capture) antibody, targeted bacteria, and secondary antibody conjugated with the MB redox-active optical probe.

After establishing the functionalization protocol, the optical absorbance data was collected with the SM-EA-IOW platform with and without the presence of the targeted bacteria under CV potential modulation. The optical absorbance when the SM-EA-IOW device was functionalized with APTES, primary LPS Ab and then exposed to gram-negative bacteria fragments followed by MB-labeled LPS Ab ( $10 \mu\text{g/mL}$ ) is shown by the black trace in Figure 4-3. As expected when the applied potential in the CV scans (scan rate  $20 \text{ mV/s}$ ) crosses the formal potential of the MB-labeled LPS Ab molecule (at about  $-0.2 \text{ V}$ ); it triggered an associated optical absorption change that was clearly detected. The red trace in Figure 4-3 corresponds to data collected when the SM-EA-IOW device functionalized with APTES and primary LPS Ab was exposed to MB-labeled LPS Ab

(10  $\mu\text{g/mL}$ ), in this case the gram-negative bacteria was absent from the solution. The negligible absorbance signal (and redox transition) in this data describes negligible amounts of MB-labeled LPS Ab on the SM-EA-IOW surface when the gram-negative bacteria is absent. As previously seen for the HA virus antigens in chapter 3, those two experimental results confirm the ability of the SM-EA-IOW platform to monitor the presence of a gram-negative bacteria through the optical signal of the biologically-matched redox probe. Also, those results confirm the successful functionalization of the SM-EA-IOW platform for the targeted bacteria and the flexibility of the SM-EA-IOW device to be used for different pathogen disease detection.

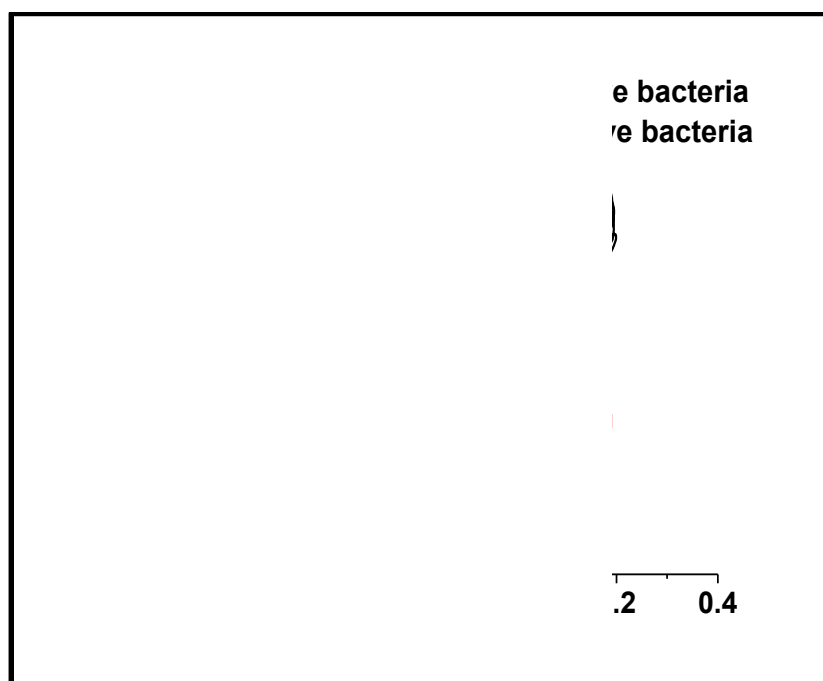


Figure 4-3: Optical absorbance at 610 nm as measured by the SM-EA-IOW platform under CV scans. The traces correspond to the data when the SM-EA-IOW device was exposed to gram-negative bacteria fragments (black trace) and in the instance the gram-negative bacteria fragments was absent from the solution (red trace); data collected after rinsing the cell.

Furthermore, for the gram-negative endotoxin fragments adsorbed on the SM-EA-IOW device that has been fully functionalized with an immunoassay to detect the targeted bacteria, the absorbance amplitude was measured following the same data collection procedure under synchronous detection, illustrated in Figure 3-7, and calculations described in Appendix 1. An AC potential modulation with frequency range from 1 to 45 Hz, an amplitude of modulating potential = 30 mV and DC bias at  $-220$  mV was used. Figure 4-4 shows the absorbance amplitude versus the angular frequency for the targeted bacteria sample. As observed, the absorbance amplitude features a peak value centered at about 5 Hz, this frequency is associated with the electron-transfer rate of the redox event under the interfacial conditions present on the electrode surface of the photonic device and can be used when applying AC voltammetry to test the clinical samples. After confirming the success functionalization of the SM-EA-IOW for targeting gram-negative bacteria, the next step was to test the clinical samples using the SM-EA-IOW platform.



Figure 4-4: Absorbance amplitude measured under AC potential modulation with the functionalized SM-EA-IOW device targeting endotoxin bacteria.

#### 4.4. Tests and Evaluation of Clinical Samples using the SM-EA-IOW Device

Eight genuine clinical samples of aqueous and vitreous humor from the eyes of patients that were presented with infections in the front of the eye (Uveitis) or in the back of the eye (Endophthalmitis) were collected by Dr. Wei Wang (Ophthalmology and Visual Sciences Dept, University of Louisville) according to an approved Institutional Review Board (IRB) for the University of Louisville and in accordance with the tenets of the Declaration of Helsinki [99]. Patients were seen in clinical settings and samples taken with sterile technique. There was no prior treatment with antibiotics to interfere with the etiology of the samples. Samples were tested for polymerase chain reaction (PCR) of bacterial material. Sequencing results were referenced by data provided by The National Center for Biotechnology Information databases. These results were kept blinded until the clinical samples had been tested with the SM-EA-IOW technology.

The same functionalization protocol of the SM-EA-IOW device described above was followed, but here instead of targeting the endotoxin from *E. Coli* K12 bacteria the gram-negative bacteria in the clinical samples was targeted. For all clinical samples tested, samples were used without any additional treatment and they were tested under CV potential modulation and AC voltammetry.

First, the optical absorbance of the clinical samples were acquired under CV potential modulation at the functionalized SM-EA-IOW device for the targeted gram-negative bacteria, results plotted in Figure 4-5. For all clinical samples, optical absorbance was measured at 610 nm. Data were collected when the SM-EA-IOW device functionalized with APTES and primary LPS Ab was exposed to a clinical sample and MB-labeled LPS Ab (10  $\mu\text{g/mL}$ ). Between each clinical sample tested, in addition to re-

cleaning the SM-EA-IOW device using the protocols described in previous chapters, the device was also roughly rinsed with 10% bleach solution and all components of the flow-cell was swiped using surface disinfectant decontaminant cleaner (CaviCide 13-1008, Metrex research) and sequentially sonicated in 10% bleach and DI water. Although the CV scan typically provides a straightforward identification of the redox process, here the results for the absorbance under CV scan for most of the clinical samples as illustrated in Figure 4-5 for two samples, show low SNR due excessive scattering from innumerable debris material present in the clinical sample. Under such low SNR in the optical CV data it was difficult to make a judgement for the absence or presence of the targeted gram-negative bacteria in each sample. However, by applying an AC voltammetric potential modulation on the SM-EA-IOW platform, in combination with synchronous detection from a lock-in amplifier, it was expected to improve the SNR and resolve this challenge.

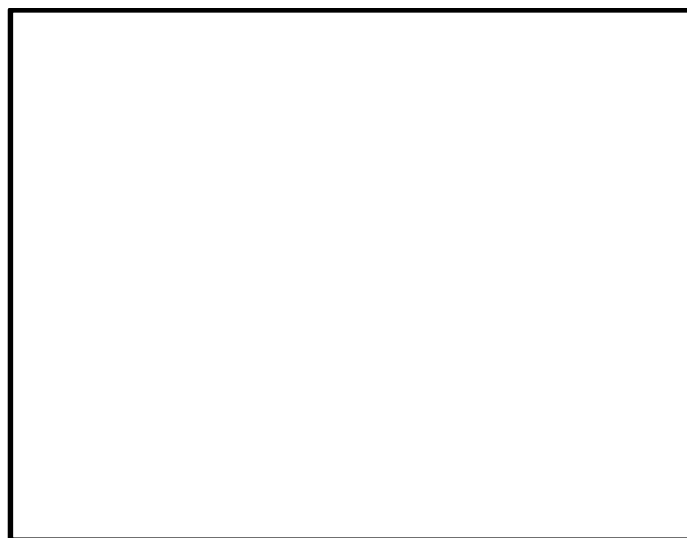


Figure 4-5: Optical absorbance at 610 nm as measured by the SM-EA-IOW platform under CV scans for samples labeled S1 and S4 (data collected after rinsing). All other clinical samples tested showed similar noisy absorbance curves under CV scans).

For each clinical sample the optical data was collected with the SM-EA-IOW platform under an applied AC voltammetric technique at the frequency of 5 Hz. This frequency was chosen based on the results presented in Figure 4-4. The potential was AC-modulated at an amplitude of 30 mV with a DC bias potential that varied over the range of  $-400$  mV to  $200$  mV for encompassing the formal potential of the redox process of the MB redox probe. As shown in Figure 4-6 a peak of the absorbance amplitude reported by the redox probe provides a clear and direct route to the detection of the targeted gram-negative bacteria. Based on those clear peaks under AC voltammetric potential-modulation the presence or absence of gram- negative bacteria was established.

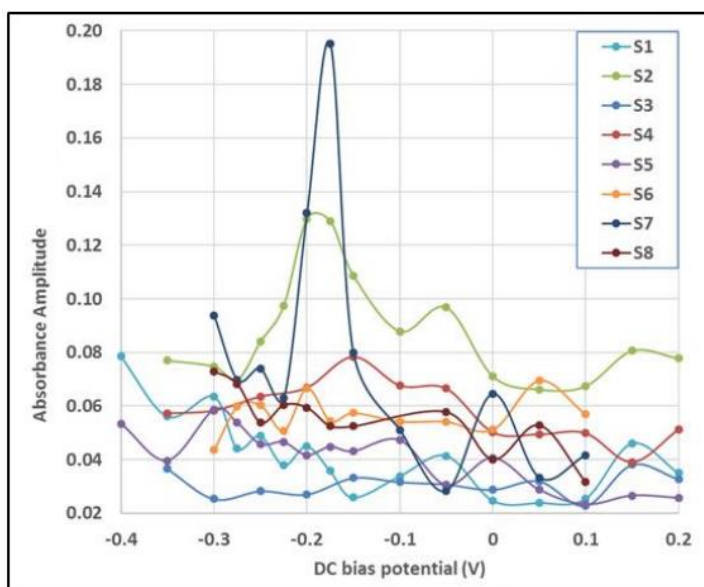


Figure 4-6: Amplitude of optical absorbance at 610 nm as measured by the SM-EA-IOW platform under AC voltammetry. All curves correspond to data collected after the SM-EA-IOW device, which was functionalized with APTES and primary LPS Ab, was exposed to a particular clinical sample, as labeled, and the MB-labeled secondary Ab ( $10 \mu\text{g/mL}$ ). All data was collected after rinsing.



After testing all the clinical samples using the SMEA-IOW, the results were compared with the tests obtained under PCR. Table 2 compares the outcomes of the SM-EA-IOW interrogation with those from PCR analysis, which was outsourced from a private company. Out of the 8 tested samples, 7 samples show agreement and 1 sample has an inconclusive outcome. Even when the PCR showed the existence of gram positive bacteria, still the SM-EA-IOW technology only detected the targeted gram-negative bacteria; such results confirm the bio-sensing methodology performance in terms of selectivity in authentic clinical samples.

Table 2: Comparison between outcomes from the SM-EA-IOW and PCR analysis of eight clinical samples.

Sample ID	EA-IOW results	PCR results	Agreement
S1	No	No	Yes
S2	Yes	Yes	Yes
S3	No	(gram positive)	Yes
S4	Yes	1 Yes, 1 No	Inconclusive
S5	No	No	Yes
S6	No	(gram positive)	Yes
S7	Yes	Yes	Yes
S8	No	No	Yes

#### 4.5. Conclusions

In conclusion, the results in this chapter showed the application, flexibility and the ability of the new label-free SM-EA-IOW immunosensors to test real clinical samples

without any pre-enrichment, filtering, or other processing steps of the samples under test. The SM-EA-IOW biosensor was capable of selectively identifying the targeted analyte with fast combination of electro-chemical and optical transduction interrogation, and the results obtained were in good agreement with state-of-the-art tests. Also, the device has demonstrated the ability to handle small sample volumes ( $\sim 50 \mu\text{L}$ ), is cost effective, and can be made simple to operate. Those results encourage the use of SM-EA-IOW to be implemented in a portable device arrangement. Such sensing strategy is expected to contribute in resolving several limitations of current bio-sensing technologies for point-of-care applications.

## CHAPTER 5 TOWARD ELECTROFLUOROCHROMIC BIO-SENSING USING SM-EA-IOW PLATFORM UNDER POTENTIAL MODULATION

### 5.1. Introduction

The transduction methodology and performance using the SM-EA-IOW platform described in the previous chapters are remarkable. The transduction mechanism itself is highly specific as the monitored analytical signal is both optically and electrochemically locked to the specific probe designed for the analyte detection. The redundancy of those selective factors highly contributes to minimize unwanted false signals from possible interference invariably present in authentic clinical samples during detection.

From this leveraged position, the investigation of electrochemically modulated fluorescent molecules to be conjugated with relevant antibodies, creating a potential-modulated fluorescent probe to work with the SM-EA-IOW device, is expected to lead to an additional breakthrough in the SM-EA-IOW bio-sensing platform. Transduction with potential-modulated fluorescent signal can lead to monitor events at the level of very few molecules whose response can be switched by reversible electrochemical manipulation. Such features will allow the generation of few molecules analytical signal that is strictly confined to surface-bound fluorophore species and eliminate background fluorescence from other biological components present in the bulk phase (e.g., serum) [14]. All combined those features are expected to further boost the SM-EA-IOW bio-sensing

performance. In this chapter, the investigation of electrochemically modulated fluorescent molecules aimed to be conjugated with relevant antibodies for creating a potential-modulated fluorescent probe to work with the SM-EA-IOW device is presented. For preliminary tests, cresyl violet molecules was investigated; those molecules display a well-characterized fluorescence behavior [42] that is dependent on its redox events. The cresyl violet molecules were investigated under potential-modulated fluorescent detection using the SM-EA-IOW. Also, preliminary attempts to conjugate the cresyl violet with secondary antibodies as a biomarker for an electrofluorochromic detection scheme is presented.

## 5.2. Experimental

### 5.2.1. Fluorescence spectroscopy

For fluorescence spectra measurements a home-built fluorescence spectrometer as shown in Figure 5-1 was used. A laser was directed to a cuvette holder, then the fluorescence signal was collected at orthogonal orientation, filtered with a notch filter, and sent to a monochromator-CCD camera for spectra acquisition.

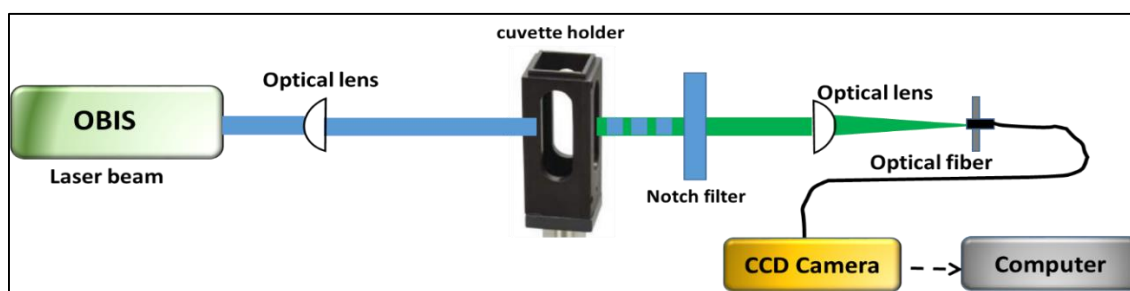


Figure 5-1: Schematic representation of fluorescence spectrometer.

### 5.2.2. Potential-modulated fluorescence spectroscopy using SM-EA-IOW

The setup for the potential-modulated fluorescence measurements with the SM-EA-IOW is shown in Figure 5-2(a). As mentioned previously the SM-EA-IOW platform was mounted in a conventional electrochemical flow-cell (Figure 5-2(b)) and a set of diffraction-limited optical components was deployed to launch the light beam towards the integrated grating coupler. Electrochemical measurements using the SM-EA-IOW were performed with the standard three electrode configuration mounted in a home-built flow-cell (ITO film on the surface of the SM-EA-IOW device as the working electrode, platinum wire as the counter electrode, and a Ag/AgCl electrode in 1M KCl solution as the reference electrode). A solid state laser source with a linearly transverse-electric polarized laser light (514 nm, Coherent Obis) was routed to the input port of the SM-EA-IOW flow-cell, and used as the excitation light source. Fluorescence emission of adsorbed molecules was collected by diffracted limited lenses and focused into an optical fiber; before focusing the collected fluorescence into the fiber, a notch filter ( $514 \pm 10$  nm, NF514-17, Thorlabs) was used to remove any scattered excitation light. The fluorescent signal was collected from the surface where the excitation beam was propagating. Also, the optical signal was monitored while a potentiostat (CHI 660D, CHInstruments, Inc.) was used to control the electric potential applied to the working electrode. In AC potential-modulated measurements, the fluorescence emission was coupled into a photomultiplier detector (PMT, H5783, Hamamatsu) that was electronically processed by a current pre-amplifier (SR570, Stanford Research Systems) before being sent to a lock-in-amplifier (SR810, Stanford Research Systems). A function generator (DS345, Stanford Research Systems) connected to the potentiostat provided a

continuous sinusoidal wave to electrically drive the SM-EA-IOW working electrode and was also used to provide a reference to the lock-in-amplifier for impedance measurements. In AC potential-modulation mode, an oscilloscope (DSO8104A Infiniium, Agilent) was used to read and record all signal measurements. Under step potential modulation, the fluorescence spectrum signal was coupled to a monochromator (SpectraPro 2300i, Princeton instruments) and detected using a CCD camera (PIXIS 400, Princeton instruments) while recorded on a computer.

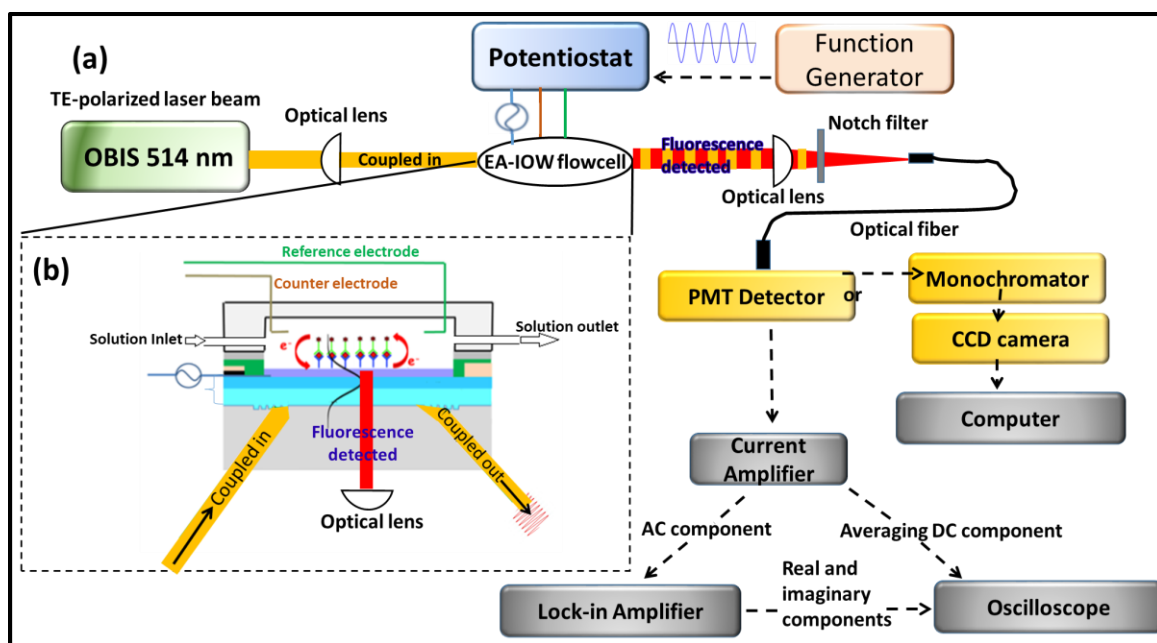


Figure 5-2: The experimental setup for fluorescence data collection from the surface of the SM-EA-IOW include a CCD camera and a monochromator for spectrally resolved measurements.

### 5.2.3. Cresyl violet maleamic sample preparation

For labeling the secondary antibody, the synthesis of an activated form of cresyl violet-NHS ester featuring carboxylic an acid functionality (cresyl violet maleamic,

CrViMa) for direct coupling to amino groups of proteins was followed and summarized in Appendix 10.

### 5.3. Results and Discussion

#### 5.3.1. Fluorescence detection of excited cresyl violet maleamic molecules adsorbed on the surface of the SM-EA-IOW

First, the ability to detect the fluorescence from the SM-EA-IOW surface was tested. For that purpose, a sample of CrViMa with a concentration of 500 nM was used. The setup in Figure 5-2 was deployed with an excitation beam at 514 nm and a corresponding notch filter. An ITO SM-EA-IOW surface was functionalized with CrViMa by injecting a solution of 500 nM into the flow-cell and allowed to incubate for about 40 minutes so the CrViMa molecules would adsorb to the SM-EA-IOW surface before being rinsed with PBS to eliminate the unbounded molecules present in the bulk solution or loosely bound to device surface. Figure 5-3 shows the collected fluorescence spectrum of CrViMa from the surface of the SM-EA-IOW. Such spectrum have the same trend when compared to the fluorescence spectrum obtained using the same sample with the setup illustrated in Figure 5-1. Those results confirm the success and efficiency of the coupled laser beam to excite molecules adsorbed to the SM-EA-IOW surface and the ability to collect the fluorescence emitted.

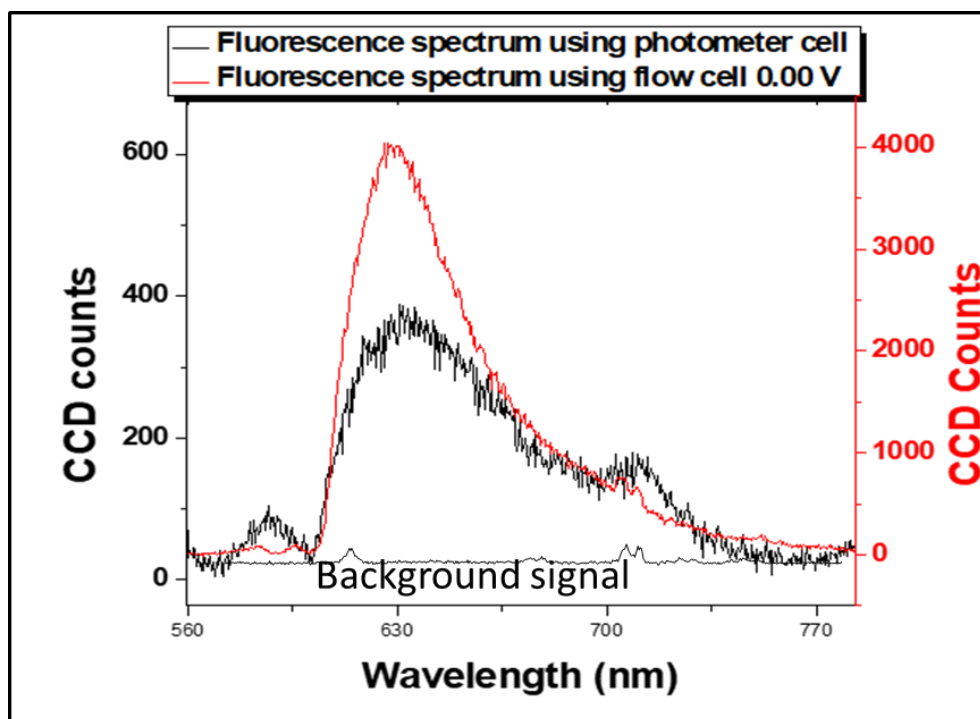


Figure 5-3: (Red) Fluorescence spectrum of CrViMa (500 nM) collected by the fluorescence spectrophotometer. (Black) fluorescence spectrum of CrViMa collected from the SM-EA-IOW surface.

### 5.3.2. SM-EA-IOW electrofluorochromic detection of cresyl violet maleamic under potential modulation (step potential and AC impedance)

Here the analysis of the modulated fluorescent measurements using the SM-EA-IOW platform under potential-modulation is based on the same analysis established for absorbance measurements elsewhere [37]. For that purpose, the ability to retrieve the optical modulated fluorescent of the adsorbed CrViMa (with a concentration of 500 nM) on the SM-EA-IOW platform under potential-modulation was tested using the setup illustrated in Figure 5-2.

Firstly, a step potential modulation was applied to the flow-cell that had CrViMa species in direct contact with a bare ITO electrode on the SM-EA-IOW device.



Figure 5-4(a)-(b) show the measured fluorescence spectrum under step potentials as marked in the plots. Also, Figure 5-4(c) shows the average fluorescence at  $(632 \pm 10)$  nm of both the spectrum fluorescence in Figure 5-4(a) and (b) plotted against applied potential. The optical data shows the unique fluorescence transition changes as the applied potential crosses the formal potential of the redox couple associated with the CrViMa molecules, this redox transition can be clearly seen in Figure 5-4(c). A fit of the modulated fluorescence (blue trace) and its derivative (black trace) as a function of the applied potential is presented in Figure 5-4(c); the derivative of the fluorescence signal against applied potential was used to determine the formal potential of the adsorbed CrViMa and it was found to be approximately -85 mV.

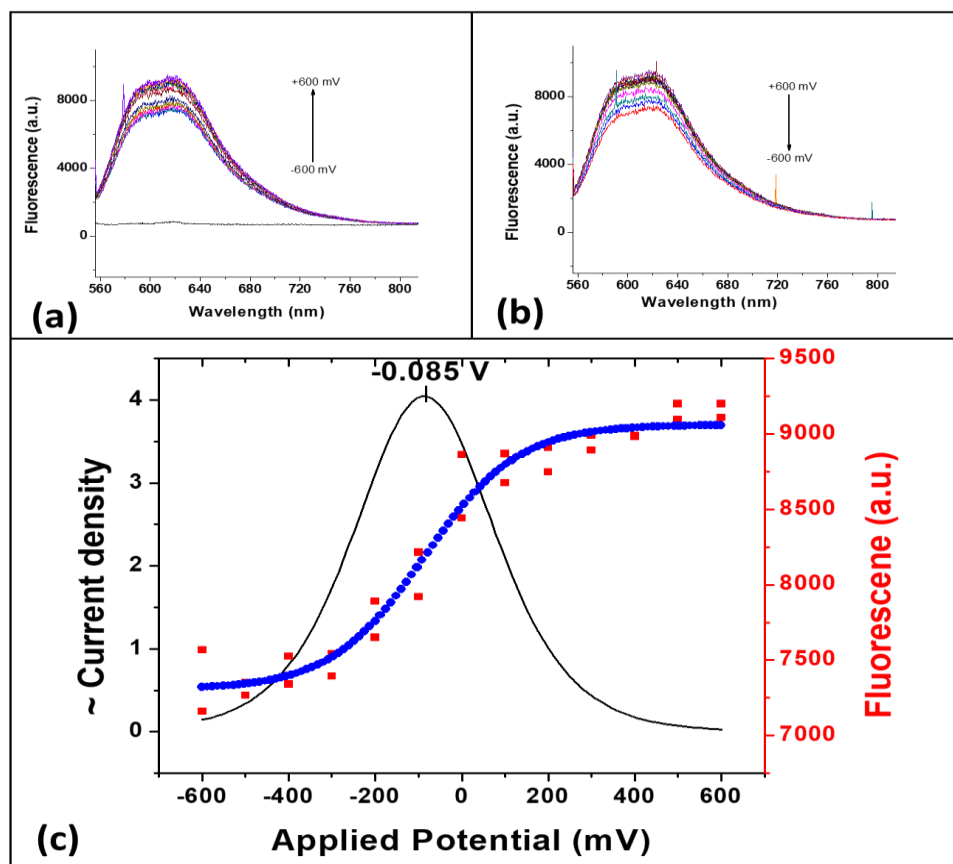


Figure 5-4: (a) Fluorescence spectrum of CrViMa 500 nM collected from the surface of the SM-EA-IOW under step potential using a CCD spectrometer. (b) Same as in Figure 5-4(a) but here the step potential started from +0.6 V to -0.6 V. (c) (red data points) Average fluorescence at  $(632 \pm 10)$  nm from the data presented in Figures 5-4(a)-(b) with a curve fitting (blue data points) and the derivative of the fitted line (black curve) to determine the formal potential.

As discussed previously an improved SNR with faster transduction times can be obtained under AC potential modulation. Briefly, for electrofluorochromic-active molecules under AC potential modulation,  $E = E_{dc} + \Delta E_{ac} \sin(\omega t)$ , a modulated fluorescence optical signal is measured for a light beam propagating along the single-mode SM-EA-IOW device. By acquiring optical data in the absence of the

electrofluorochromic active molecule (i.e., baseline),  $F_0 = F_{dc,0} + \Delta F_{ac,0} \sin(\omega t + \theta_0)$ , (where  $F_{dc,0}$  represents a term that is constant in time and its value depends solely on  $E_{dc}$ ,  $\Delta F_{ac,0}$  represents the amplitude, and  $\theta_0$  represents the phase of the fluorescent optical signal response originated under the electric potential modulation) and in the presence of the electrofluorochromic-active molecule,  $F = F_{dc} + \Delta F_{ac} \sin(\omega t + \theta)$ , (where  $F_{dc}$  represents a term that is constant in time and its value depends solely on  $E_{dc}$ ,  $\Delta F_{ac}$  represents the amplitude, and  $\theta$  represents the phase of the fluorescent optical signal response originated under the electric potential modulation in the presence of the electrofluorochromic active molecule. Based on the previous established equations for in-phase and out-of-phase components of the AC modulated optical signal [37], one can determine the in-phase  $\Delta F_{ac,in}$  and out-of-phase  $\Delta F_{ac,out}$  components of the AC modulated fluorescence optical signal by:

$$\Delta F_{ac,in} = -\frac{\Delta F_{ac} \cos(\theta)}{F_{dc} \ln(10)} + \frac{\Delta F_{ac,0} \cos(\theta_0)}{F_{dc,0} \ln(10)} \quad \text{Equation 5-1}$$

$$\Delta F_{ac,out} = -\frac{\Delta F_{ac} \sin(\theta)}{F_{dc} \ln(10)} + \frac{\Delta F_{ac,0} \sin(\theta_0)}{F_{dc,0} \ln(10)} \quad \text{Equation 5-2}$$

and from the in-phase and out-of-phase components of the AC modulated optical fluorescent one can measure the total fluorescent amplitude with:

$$\Delta F_{ac} = \sqrt{(\Delta F_{ac,in})^2 + (\Delta F_{ac,out})^2} \quad \text{Equation 5-3}$$

Fluorescent modulated signal under applied AC potential modulations was collected using synchronous detection as illustrated Figure 5-2. AC potential modulation with an amplitude of 30 mV at different frequencies ranging from 1 Hz to 45 Hz were applied. Procedure of CrViMa adsorption to the SM-EA-IOW surface was the same as mentioned above, the baseline signal was recorded before the injection of the CrViMa

into the flow-cell, and the fluorescence modulated optical signal was then recorded after the injection of a 500 nM solution of CrViMa under the same AC potential modulation parameters applied to the baseline. Figure 5-5 shows the total fluorescence amplitude of the adsorbed CrViMa measured using Equation 5-3; such results confirm the ability of the established optical impedance technique using the SM-EA-IOW to measure the modulated fluorescence and the possibility to apply the same analysis based on optical absorbance measurements for modulated fluorescence measurements [70].



Figure 5-5: Fluorescence of CrViMa collected from the surface of the SM-EA-IOW using excitation laser at 514 nm under AC impedance with a DC bias at -0.085 V, an amplitude of modulation of 30 mV and optical detection using a PMT with notch filter at 514 nm.

In addition, by following and taking advantage of the established simple methodology to measure the electron-transfer rate of redox active molecules on the SM-EA-IOW platform [70], one can simply use the same equations to measure the electron-transfer rate of electrofluorochromic molecules using the fluorescence-modulated optical signal. Briefly, in order to determine the electron-transfer rate ( $k_{ET}$ ) using OIS, it is sufficient to collect both the electrical impedance,  $Z(\omega)$ , of the electrochemical flow-cell and the modulated fluorescence amplitude,  $\Delta F_{ac}(\omega)$ . Based on electrochemical equivalent circuit described previously for redox active molecules in Appendix 2,  $k_{ET}$  can be expressed as:

$$k_{ET} = \frac{1}{2C_a R_{ct}} = \frac{y(\omega)}{x(\omega)} \quad \text{Equation 5-4}$$

where here for fluorescence modulated signal  $y(\omega)$  and  $x(\omega)$  are defined as

$$x(\omega) = 2[Z'_{tot}(\omega)\Delta F_{ac,in}(\omega) - Z''_{tot}(\omega)\Delta F_{ac,out}(\omega)] \quad \text{Equation 5-5}$$

and

$$y(\omega) = \omega [Z'_{tot}(\omega)\Delta\Delta F_{ac,out}(\omega) + Z''_{tot}(\omega)\Delta F_{ac,out}(\omega)] \quad \text{Equation 5-6}$$

where  $Z'_{tot}(\omega)$  and  $Z''_{tot}(\omega)$  are the real and imaginary parts of the total impedance respectively, which are obtained from the potentiostat, and the real and imaginary parts of  $\Delta F_{ac}(\omega)$  are obtained from the optical impedance measurements. With  $Z_t(\omega)$  and  $\Delta F_{ac}(\omega)$  known and, by following the same analysis discussed in chapter 2 and as shown in Equation 2-7, one can use a parametric plot of  $y(\omega)$  against  $x(\omega)$  where a linear graph is formed with a slope representing the electron-transfer rate,  $k_{ET}$ , of the faradaic process of the adsorbed electrofluorochromic molecules. The formalism described above was applied to retrieve the electron-transfer rate of CrViMa at a concentration of 500 nM, with data in Figure 5-6 showing a parametric plot to retrieve the electron-transfer rate to

be  $(55 \pm 2) \text{ s}^{-1}$ . These experimental results illustrate the ability of the methodology described above to determine and retrieve the electron-transfer rate of electrofluorochromic-active molecules based on potential-modulated fluorescence signal.



Figure 5-6: The parametric plot of  $(\omega) = k_{ET} x(\omega)$  with a linear fitting used to retrieve the electron-transfer rate of electrofluorochromic-active CrViMa molecules based on the potential-modulated fluorescence signal.

### 5.3.3. Preliminary tests to conjugate CrViMa into H5N1 secondary antibody

The results above confirm the ability to detect a modulated fluorescence signal of electrofluorochromic-active molecules adsorbed to the surface of the SM-EA-IOW device. Such assurance opens the possibility to conjugate electrofluorochromic-active molecules on antibodies to be used in immunoassay-based detection incorporated onto the SM-EA-IOW. The idea as illustrated in Figure 5-7 is similar to the strategy presented in chapter 3, but here the reporting signal is based on the modulated fluorescence from

electrofluorochromic-active molecules instead of absorbance signal measured from a redox-active probe.

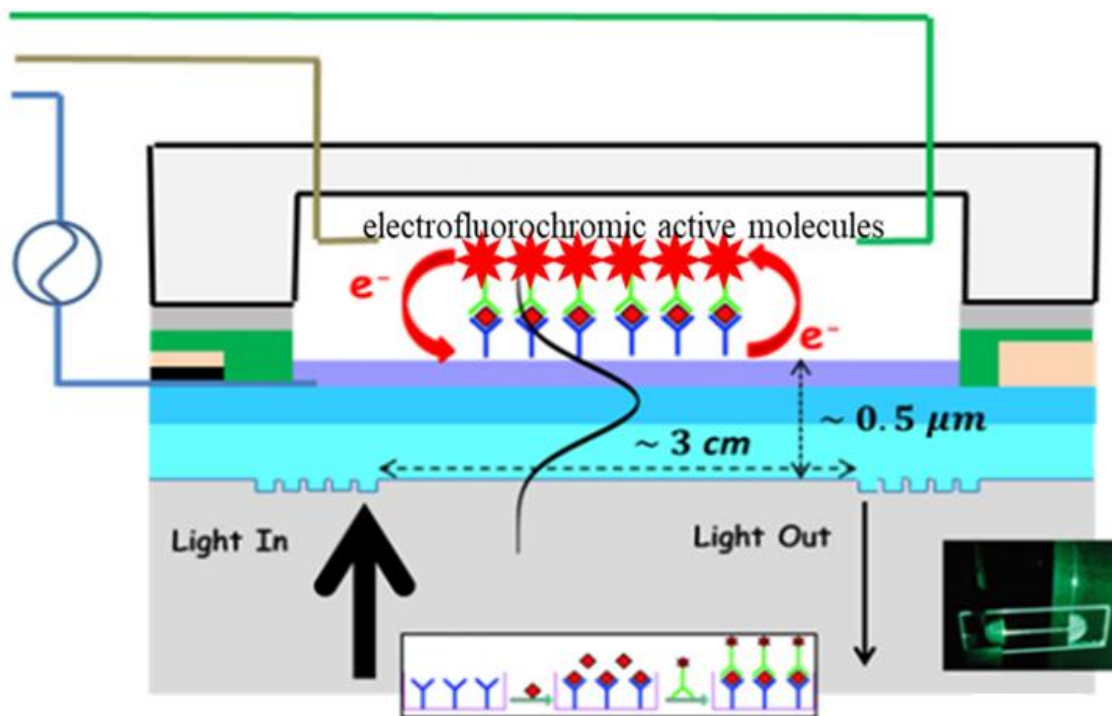


Figure 5-7: Steps of the proposed sandwich bioassay with the bonded Ab, the biological target binding, and the secondary Ab with an electrofluorochromic-active optical marker.

The task is to target an already tested system, the H5N1 virus antigens, using the above proposed methodology. CrViMa was the first molecule used in an attempt to conjugate a secondary Ab signal reporter. CrViMa forms a good candidate as it has a NHS-ester group, which features a carboxylic acid functionality for direct coupling to amino groups of proteins. The attempt conjugation process is summarized in details in Appendix 11. Unfortunately according to the UV-Vis spectrum shown in Figure 5-8, the absence of the peak that is related to the fingerprint of CrViMa indicates that the current conjugation process was not successful.

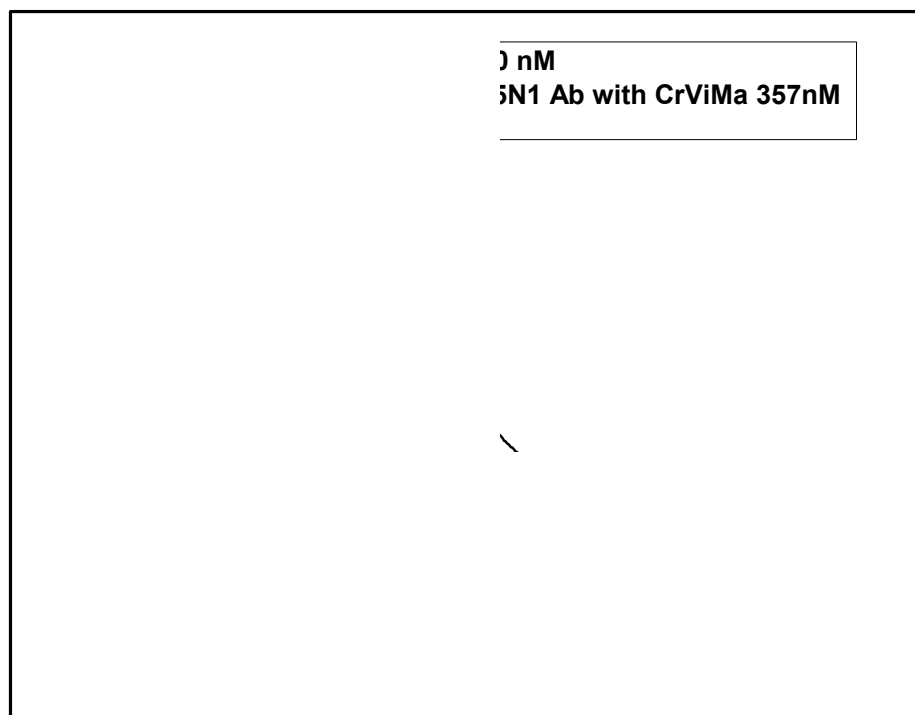


Figure 5-8: UV-Vis absorbance of free CrViMa and CrViMa-labeled H5N1 Ab.

However, after testing the sample using the fluorescence spectrometer illustrated in Figure 5-1, the fluorescence spectrum showed some evidence of the presence of CrViMa in the conjugated secondary H5N1 Ab sample, as shown in Figure 5-9. This may indicate that the conjugation was to some degree successful but the degree of labeling between CrViMa and the secondary Ab stills needs to be improved to fully advance this novel sensing methodology.



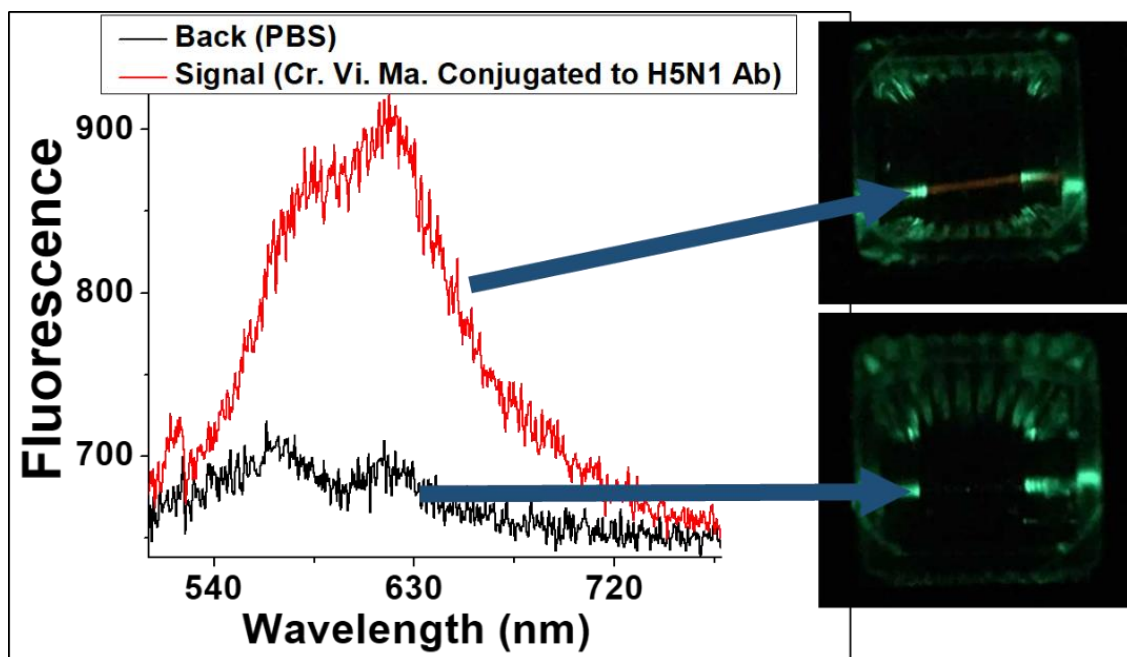


Figure 5-9: Fluorescence spectrum of CrViMa-labeled H5N1 Ab.

#### 5.4. Conclusions

The preliminary steps to deploy the electron-transfer process of an electrofluorochromic-active molecule under potential modulation using SM-EA-IOW were developed and presented here. The experimental results provide a path towards using electrofluorochromic-active molecule to be conjugated into a reporting Ab for bio-sensing applications using SM-EA-IOW platforms; such capability is expected to provide higher sensitivity as the fluorescent analytical signal grows from negligible background. The initial tests for conjugating an electrofluorochromic-active molecule (CrViMa) on a secondary Ab are still insufficient for the envisioned applications, however such a proposed technique is promising and additional improvements in this research efforts are expected to unfold into further breakthroughs in sensing applications.

## CHAPTER 6 PHOTOBLEACHING REDUCTION AND SINGLE MOLECULE SUPER RESOLUTION IMAGING AT LOW EXCITATION AND DEPLETION POWERS WITH MODULATED STED MICROSCOPY

### 6.1. Introduction

Single-molecule spectroelectrochemical techniques based on electrically-driven fluorescence signals is anticipated to be intrinsically more sensitive than those based on absorbance signals. Still, using conventional optical fluorescence microscopy can only provide information limited by the diffraction barrier of the focused light. Also, in fluorescence based measurement, perhaps an even more significant challenge is the effect of photobleaching which can lead to poor signal-to-noise ratio in single-molecule spectroscopic studies. Such limitations are still a challenge and can impact the spectroelectrochemical imaging formation and the collected quantitative data at the single molecular level.

In this chapter, the buildup of an innovative modulated-STED super-resolution imaging technique is described and shown to be capable of achieving far-field images with sub-diffraction resolution in the visible part of the spectrum. Compared to conventional STED approaches, the developed modulated-STED tool is shown to be capable of reducing the required optical powers of the excitation and depletion laser

beams. The outcomes of such improvement were to reduce photobleaching effects in single molecule STED imaging and to minimize undesirable background signals that invariably comes from the application of the depletion beam. Those features may also open the possibility for new applications of STED imaging at reduced complexity and costs.

#### 6.1.1. The diffraction limit

It has been known that the resolution of focusing far-field light in optical imaging is fundamentally limited by the diffraction barrier. The first person to come with the concept of diffraction limit is Ernest Abbe [45] back in 1873; he formulated that in order to separate two features of the same kind by light microscope, they have to be separated by a distance equals to the wavelength of the light divided by twice the numerical aperture of the microscope objective. Mathematically he described it by his famous equation

$$d = \frac{\lambda}{2 \times NA} \quad \text{Equation 6-1}$$

where  $d$  is the minimum resolvable distance,  $\lambda$  is the wavelength of light and  $NA$  is the numerical aperture.

In life sciences probably the most widely used far-field imaging tool has been fluorescence microscopy [104]. In a fluorescence microscope all the features inside the spot of the focused light will be illuminated and excited at the same time by the excitation light beam, as illustrated in Figure 6-1. And hence all those features falling within the diffraction barrier will give signal and this signal will be collected at the same time, thus it will be impossible to resolve those features apart.

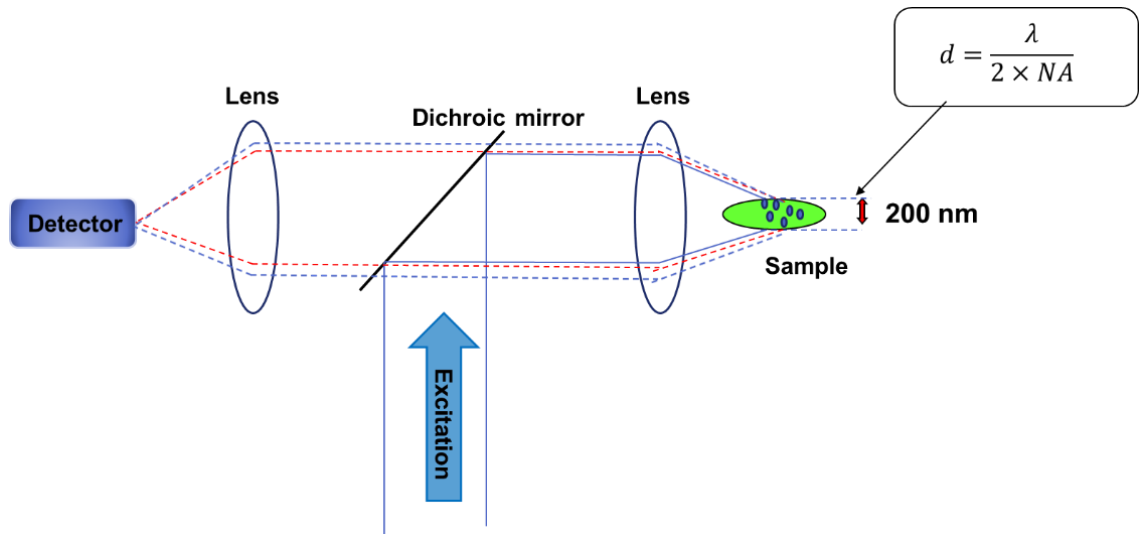


Figure 6-1: Schematic diagram of a fluorescence microscope.

An important issue in fluorescence microscopy is the generation of the out-of-focus signal, as illustrated in Figure 6-1 by the dashed red and blue lines. A modified version of fluorescence microscope is the confocal microscope [105, 106]. The confocal microscope has the ability to achieve optical sectioning from the inside of the investigated sample with a negligible background signal. A schematic layout of a confocal microscope is shown in Figure 6-2. The main part of the confocal microscope is that the fluorescence is collected and focused onto a point-like detector. The image data buildup is achieved by scanning the focus through the sample (or the sample over the focal point). The size of the detector is about 80% of the first two minima in a lateral profile of the generated light focus of the Airy pattern. Still confocal microscope is limited by the diffraction barrier, which is a limiting factor to achieve single molecule imaging.

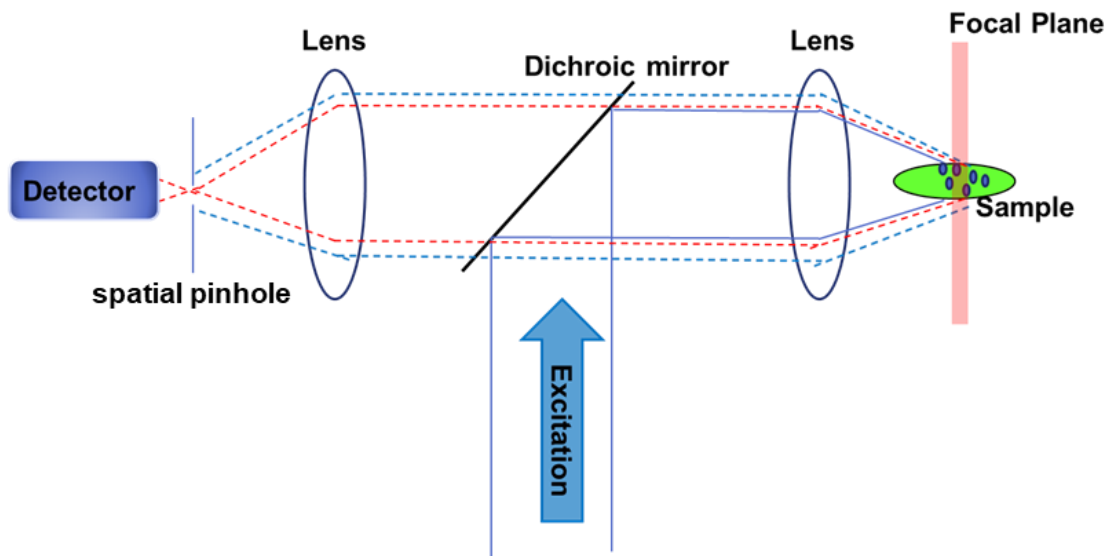


Figure 6-2: Schematic diagram of a confocal microscope.

#### 6.1.2. Super resolution imaging techniques

In far-field imaging a series of innovative strategies have recently been devised to overcome the diffraction limit [48, 52]. The main far-field optical microscopy strategies with sub-diffraction resolution are: structured-illumination microscopy [49], single-molecule based localization microscopy [50], and stimulated-emission depletion (STED) microscopy [51]. The most adopted of those innovative techniques is STED microscopy, which was developed by Stefan Hell (Nobel Prize in chemistry, 2014) and his group in Germany [107, 108]. Since then STED microscopy has become a popular tool and has been widely adopted for investigations in the single molecule level imaging [109-111]. This method relies on a principle related with every dye which is stimulated emission, which makes the method very powerful. Using STED imaging, a single molecule resolution in fluorescent samples of 5 nm to 20 nm in the lateral directions has been demonstrated [112].

### 6.1.3. Principle of STED microscopy

The STED concept takes advantage of the stimulated emission process to create an effective excitation spot below the diffraction limit. The basic concept of stimulated emission is illustrated in Figure 6-3 [113]. The fluorescent molecule is excited by an excitation beam to a higher vibronic level of the excited state  $S_1$  from the ground state  $S_0$ . Then it decays non-radiatively in a very fast time (in several ps) to the lowest vibronic energy level of  $S_1$ . Fluorescence signal, which is red-shifted compared to the excitation wavelength of this molecule, can be detected when this excited molecule relaxes to  $S_0$  state via spontaneous emission. However, the excited state of a molecule can also be stimulated to emit a photon. This can be done using a light (depleting beam) that matches the energy gap between  $S_0$  and the lowest vibronic level of the excited state  $S_1$ . The stimulated emitted wavelength is not detected as a fluorescence signal because it is red-shifted compared to the excitation beam.

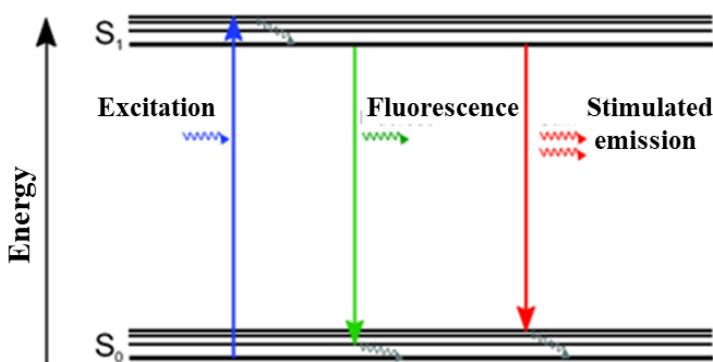


Figure 6-3: Schematic two-level energy diagram of a fluorescent molecule.

In STED imaging technique two overlapping laser beams are deployed: one used for excitation and another for depletion of an optically-active state in a population of nanometer scale species. In general, as illustrated in Figure 6-4, STED imaging can be

applied in any system where the following conditions are met [114]: i) there is a bright A and a dark state B; ii) the transition  $A \rightarrow B$  is photoinducible; iii) an arbitrarily shaped region purely in A can be embedded in a region that is mostly in B; and iv) photo-absorption by the A state produces a detectable signal that is not observed in B. The Airy pattern of an excitation beam which is diffraction limited is combined with a doughnut-shaped depletion beam that is red-shifted and out of the detection region (Figure 6-4(b)). The doughnut-shaped depletion beam is created using a phase plate, as illustrated in Figure 6-4(c) the phase plate will imprint a phase factor onto the incident beams, which transforms its Gaussian beam into a doughnut beam by destructive interference on the optical axis. As shown and illustrated in Figure 6-4(d), due to stimulated emission by the depletion beam on the periphery of the Airy pattern, the fluorescence emission becomes confined to the region around to the doughnut zero. A super-resolved image is then constructed by scanning the sample underneath the beams and sequentially collecting fluorescence signal on a pixel by pixel basis.

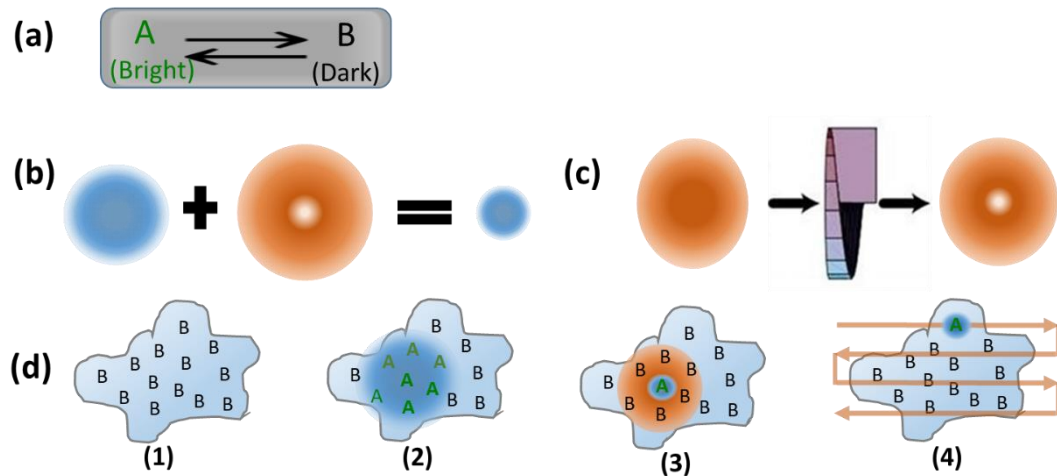


Figure 6-4: (a) Bright and dark states and the transition between A to B and vice versa is photoinducible. (b) The excitation spot (blue) is overlapped with the STED depletion

laser profile (orange) at x-y focal plane to create an effective excitation spot below the diffraction limit. (c) The special phase plate imprints a phase factor  $\exp(i n \phi)$  onto the incident beams, Gaussian beams are transformed into doughnut beams by destructive interference on the optical axis. (d): (1) Ensemble in a sample in B dark state. (2) Some portion of the ensemble is excited to state A within a diffraction limit spot size. (3) A sub-diffraction-sized effective excitation point spread function is generated by superimpose conventional excitation beam and a depletion beam exhibiting a central zero intensity zone. (4) This effective excitation point spread function is scanned across the specimen, and this results in an image that is beyond the diffraction limit.

The effective point-spread-function (PSF) of the STED microscope can be mathematically described as reported by Stefan Hell and coworkers [115, 116] by a modified Abbe's equation and is given by:

$$d = \frac{\lambda}{2 \times NA \times \sqrt{1 + \frac{I}{I_s}}} \quad \text{Equation 6-2}$$

where  $I$  is the intensity of the depletion laser,  $I_s$  is the laser intensity to deplete 50% of the fluorophores intensity.

#### 6.1.4. Main challenges in single molecule imaging using STED microscopy

Implementation of STED microscopy was challenging in the past [117] and several strategies have been developed to facilitate its applications [110, 118]. The most straightforward realization of the STED technique uses CW laser beams for the excitation and depletion [119] of optically active species. In principle, there is no fundamental limit to the spatial resolution obtainable by STED microscopy, which is essentially determined by the extent that the intensity of the depletion beam can be varied over a short distance



[116]. For reaching a high spatial resolution (i.e., a tightly confined point spread function) a strong depletion beam is invariably required [120], however such requirement brings several practical difficulties. One of the crucial drawbacks due to this strong depletion beam in STED imaging is photobleaching, also a relatively high excitation laser power is generally desirable to maximize the fluorescence emission and improve image quality which also increases photobleaching effect. Several approaches have been developed aimed to reduce photobleaching effect in STED microscopy, such as decreasing the dwell time in the scans or increase the field of view in STED imaging [121], or applying a time Gated-STED. In STED time gating imaging, the reduction of the saturating intensity has led to acquire STED images with higher resolution at lower depletion power [122, 123]. Another technical problem that arises from a strong depletion beam is due to its probability to excite the optically active species. This undesirable effect can be reduced by detuning the depletion wavelength far from the excitation band and by using efficient notch and passband filters, but the effect may still be non-negligible for strong depletion beams. Another important point should be taken into account is the preparation of samples for STED microscopy, such as using an embedding medium that matches very well the refractive index of the supporting substrate, as any small mismatch may result in unwanted back reflected background from the depletion laser beam. A strong depletion power has also been reported to induce optical trapping [116].

#### 6.1.5. Modulated STED microscopy

Typically, in STED microscopy only a small number of dyes can be studied by a certain pair of excitation and depletion wavelengths. In order to expand the possibility of

using the single laser wavelength in the depletion beam to work with fluorophores of different emission spectra, a general concept named modulated STED was proposed by Ronzitti and colleagues [61] based on an intensity modulation of the excitation laser beam combined with synchronous detection of the fluorescence signal with a lock-in amplifier, while using a CW depletion beam for reaching super-resolution in far-field imaging. They have demonstrated the ability of modulated STED to work with a broader range of dyes while deploying a single wavelength for the depletion laser.

## 6.2. Experimental Setup (Implementation of Modulated STED Microscopy)

### 6.2.1. Layout of the modulated STED microscope

A STED microscope is shown schematically in Figure 6-5 was built following the major features of a previously reported configuration [124].

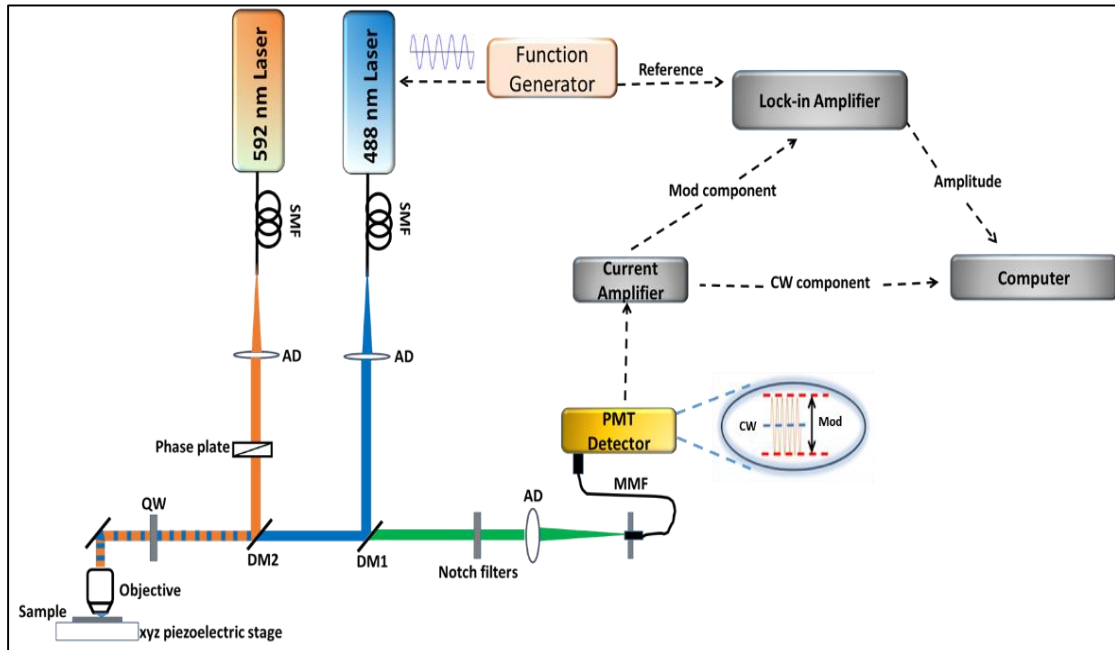


Figure 6-5: Experimental setup with the 488 nm and 592 nm laser lines used for the excitation and depletion sources, respectively. The laser beams are injected into single-

mode fibers with focusing lenses. The excitation beam was modulated using a function generator. The depletion laser was passed through a spiral phase plate to generate the doughnut shape. Both beams were circularly polarized by a quarter-wave plate. The depletion beam was collinearly aligned with the excitation laser coupled into the confocal imaging path. Laser focusing and fluorescence collection was done through an objective lens (Olympus, 100X, 1.35 NA). Sample was scanned using an XYZ piezo electrically driven stage. A photomultiplier tubes was used for light detection. The detected signal was synchronized to the excitation laser modulation using a lock-in amplifier connected to a computer for data acquisition.

#### 6.2.2. Excitation and depletion beam coupling

The excitation laser at 488 nm was delivered by an OBIS laser with single spatial mode and 60 mW maximum power (488-60 LS, Coherent, Santa Clara, California, USA) and the depletion beam at 592 nm was provided by a CW single spatial mode fiber laser with a 1.5 W maximum power (MPB Communications, Montreal , Canada). In order to further spatially filter the excitation and depletion beams, each beam was coupled to a single-mode fiber (P1-488PM-FC-5, Thorlabs, Newton, New Jersey, USA) using a 40X microscope objective with numerical aperture of 0.65 (Newport, Irvine, California, USA) mounted on a single-mode fiber launch unit (MAX350D, Thorlabs, Newton, New Jersey, USA) (Figure 6-6).

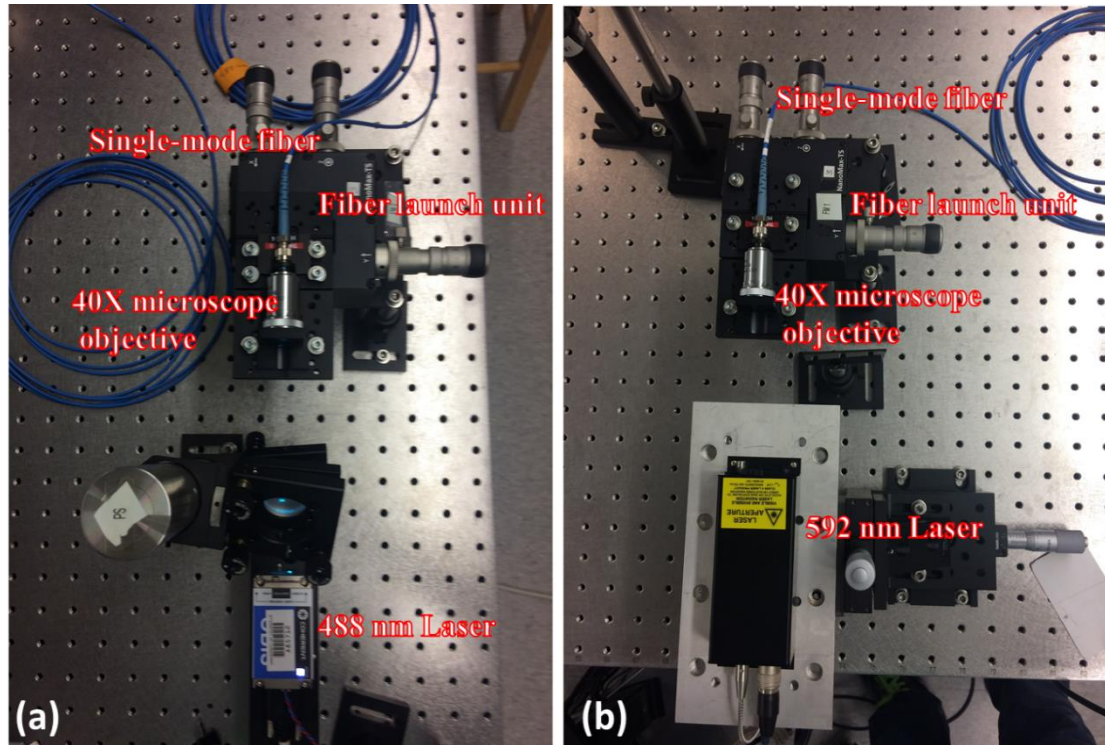


Figure 6-6: (a) Coupling excitation beam into SMF. (b) Coupling depletion beam into SMF.

### 6.2.3. Excitation and depletion beams; collimation and stage beams launch

The output of each fiber port was mounted on a 4-axis stage, which provided the necessary degrees of freedom to collimate and reach co-linearity among the optical beams. Each beam was collimated using an aberration-corrected lens (PAF-X-18-PC-C, Thorlabs, Newton, New Jersey, USA) of focal length of 18.4 mm that was mounted on a 5-axis stage (Figure 6-7).

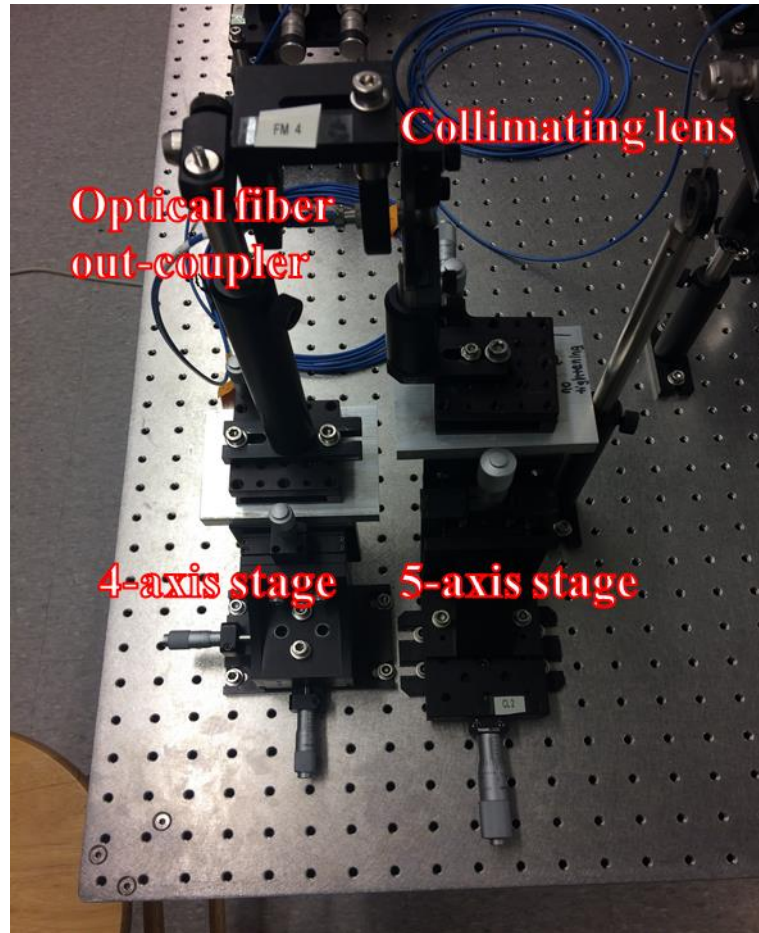


Figure 6-7: Excitation/ Depletion beam fiber launch.

#### 6.2.4. Doughnut shape

As shown in Figure 6-8, the depletion beam passed through a Vortex phase plate (VPP-1, RPC Photonic Inc., Rochester, New York, USA), which was used to generate the characteristic doughnut pattern.

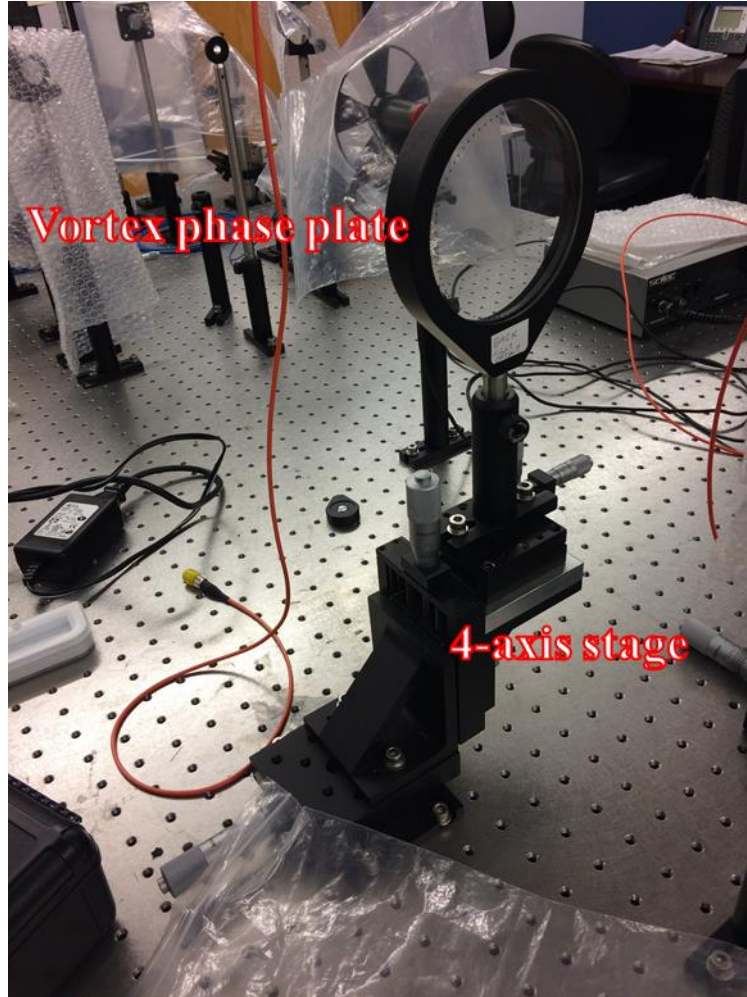


Figure 6-8: The collimated depletion beam is engineered to a doughnut shaped beam using a vortex phase plate mounted on a 4-axis stage.

#### 6.2.5. Main optical path

The excitation beam was directed toward a microscope objective with 100X magnification and a numerical aperture of 1.35 (RMS100X-PFOD Olympus, Thorlabs, Newton, New Jersey, USA) mounted on an optical microscope (BX51M, Olympus, Center Valley, Pennsylvania, USA) using a dichroic mirror DM1 (ZT488rdc-UF2, Chroma, Mchenry, Illinois, USA). The depletion beam was also directed towards the microscope



objective using another dichroic mirror DM2 (z590sp-rdc, Chroma, McHenry, Illinois, USA). The main optical path is shown in Figure 6-9.

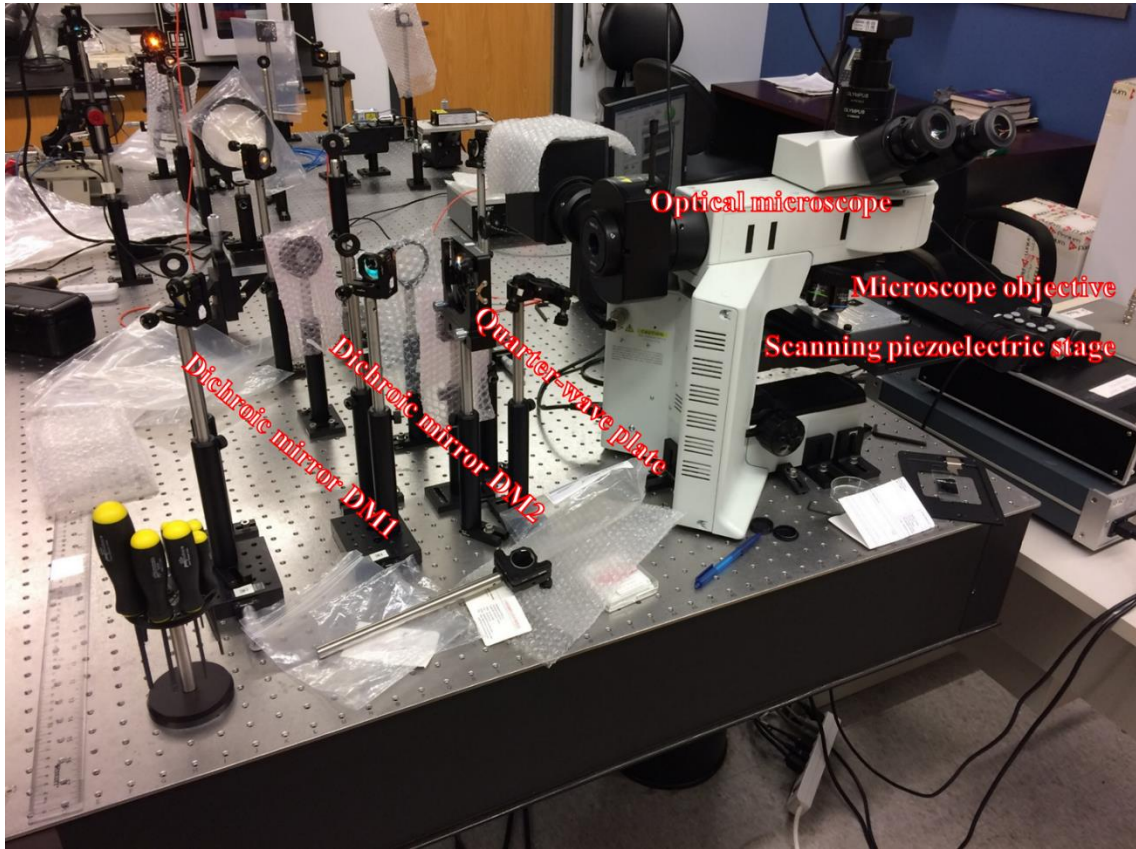


Figure 6-9: Main optical path combining both laser beams on the objective and also collecting the fluorescence signal. Quarter wave plate converts the beams onto circular polarization. Scanning piezoelectric stage used to construct the image.

#### 6.2.6. Coupling laser to objective

Before being directed to the objective, both the excitation and depletion beams were sent through a quarter-wave plate (AQWP025M-600, Thorlabs, Newton, New Jersey, USA), which was used to generate symmetrically and circularly polarized beams at the objective back focal plane. In order to ensure the circularity of the polarization, a

broad-band metallic mirror has been used to reflect the beams through the objective (21010, Chroma, McHenry, Illinois, USA).

#### 6.2.7. Detection path

Figure 6-10 shows the detection path, the fluorescence emitted from the sample was collected by the same objective lens and passed through the dichroic mirrors DM1 and DM2. The signals were then spectrally cleaned via notch filters (NF03-488E-25, NF03-594E-25, Semrock, Rochester, New York, USA) and coupled using an achromatic doublet (AC254-300-A, Thorlabs, Newton, New Jersey, USA) into a multi-mode optical fiber (MMF) (M31L02, Thorlabs, Newton, New Jersey, USA). The opening diameter of the MMF is about 80% of the back-projected Airy disk, which served as the confocal aperture.

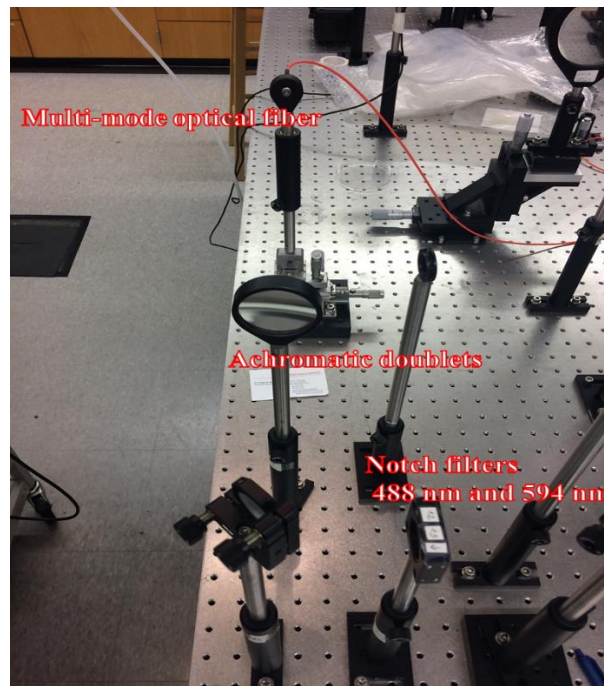


Figure 6-10: Detection path consists of notch filters followed by  $45^\circ$  mirror that sends the beam through an achromatic doublets that focus the detected fluorescence onto a multimode optical fiber.



#### 6.2.8. Synchronous detection

A photomultiplier tubes (H5783, Hamamatsu, Hamamatsu, Japan) that was connected to a low-noise current preamplifier (SR570, Stanford Research Systems, Sunnyvale, California, USA) was used to detect the photons from the fluorescent samples. For acquisition under the modulated STED configuration as shown and illustrated in Figure 6-5, the excitation laser at 488 nm was directly sinusoidal modulated,  $\left(\frac{I_{max} - I_{min}}{I_{max} + I_{min}} = 1\right)$ , from a function generator and the detected fluorescence signal was sent to a lock-in amplifier (SR830 DSP, Stanford Research Systems, Sunnyvale, California, USA) that was tuned to the fundamental frequency of the excitation beam. The amplitude of the modulated signal was sent to a personal computer using a programmable gate array board (BNC 21010, National Instruments, Austin, Texas, USA).

#### 6.2.9. Stage and image acquisition

A home-built LabVIEW code was used to record the signal and build the images. The image construction was acquired using a scanning piezoelectric stage (Nano-PDQ350, Mad City Labs Inc., Madison, Wisconsin, USA). STED and confocal images acquisition were taken consecutively on the same sample area by turning on and off the depletion beam.

#### 6.2.10. Scanning protocol

The LabVIEW program was written by Dr. Thomas J Russel (Department of Bioengineering, J. B. Speed School of Engineering/ University of Louisville) to drive the stage in a form as illustrated in Figure 6-11, the stage starts at the origin at point labeled “start”. Then it moves through a horizontal line in the “x” direction, the length of which

has been assigned by the user. During the scan at each pixel size the detector collects photons at a continuous rate. At the end of the line, the stage moves one “step” defined by the “pixel size” in y-dimension and then scan in the “-x” direction. It repeats this process until to collect data across all the area to be scanned “as illustrated by the light orange arrows”. Subsequently, the image constructed by an algorithm based on photons collected at each pixel. After the stage reaches the end point it returns to the start point as shown with the blue arrow.

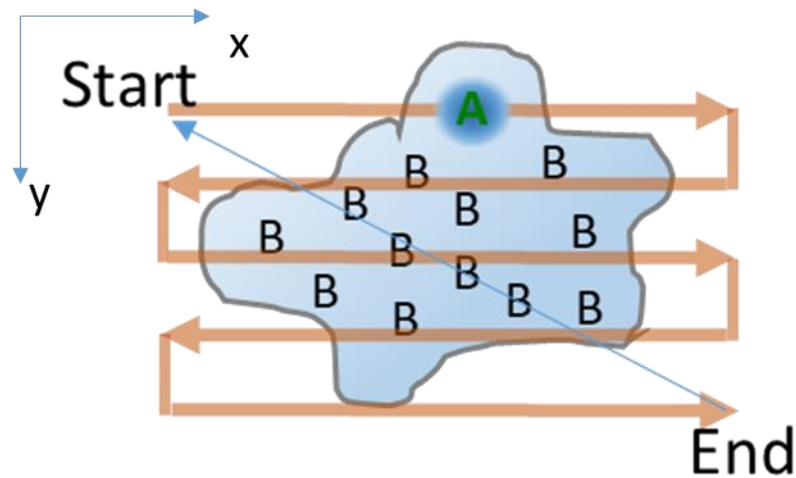


Figure 6-11: Schematic representation of the scan strategy to construct an image.

### 6.3. Validation and Alignment of the STED Setup

#### 6.3.1. Point spread functions of the laser beams

To ensure the beam quality focused poses the diffraction limit with Gaussian shape, the shape of excitation and depletion beams was characterized by scanning and acquiring the back reflection image of strips target in its focal plane, Figure 6-12. With the strips target, the system measured confocal resolution of ~190-220 nm. Also the

central FWHM of the depletion beam was approximately 200 nm. Hence, those beams have point spread functions close to the theoretical diffraction limit.

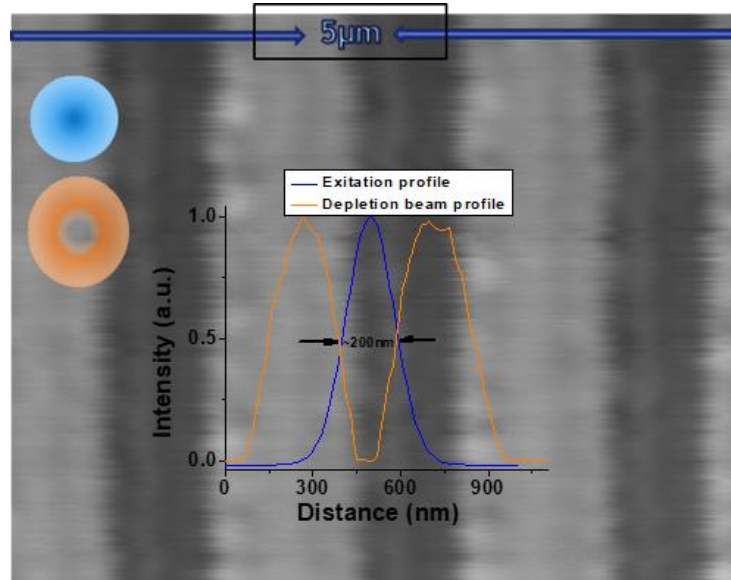


Figure 6-12: Point spread functions of the excitation and depletion beams measured by collecting the back reflected light from a strip target. The measured FWHMs show the dimension of the laser beams are close to the diffraction limit  $\sim 200$  nm.

### 6.3.2. Alignment and collinearity of the depletion and excitation beams

Alignment of the system was achieved by using irises at different spots in the setup as shown in Figure 6-13(a). First, the alignment started with the excitation beam, by sending it through the excitation beam path, then the back reflected beam through a metallic mirror placed in the sample holder was observed. In case of misalignment, the propagated or the back reflected laser beam would be blocked by a specific iris, the absence of the laser beam passing through any of the irises provides an indication of a misalignment. After that the depletion beam was send through the depletion path, and to

align the beam the same alignment procedure as mentioned above for the excitation beam was followed.

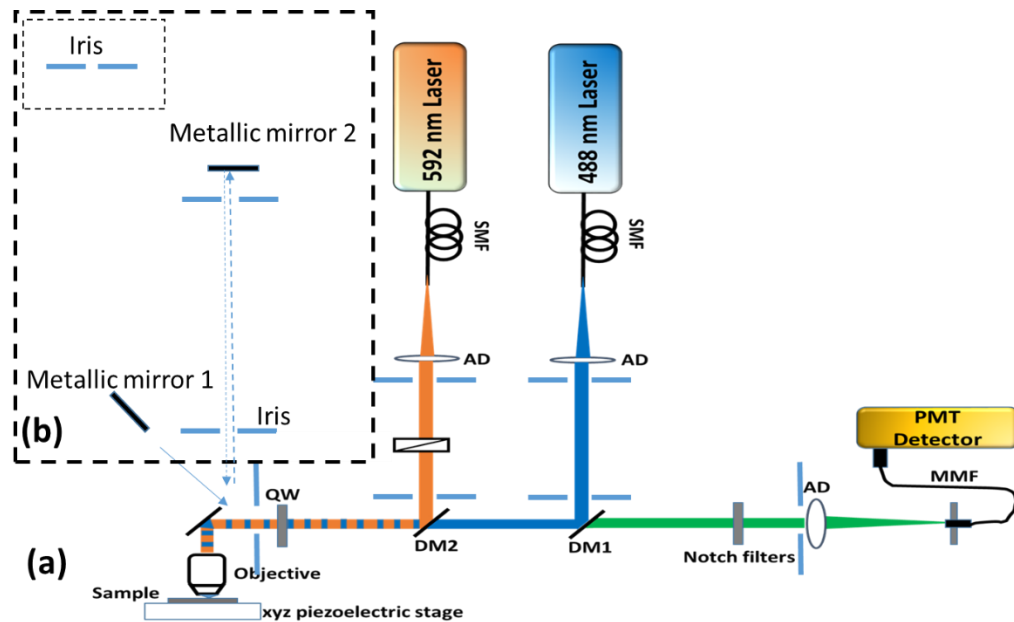


Figure 6-13: (a) Alignment of the system; for the alignment several irises was placed at several points as indicated. The beams are send through the iris through the objective, and a back reflection mirror used to reflect back the beams through the objective lens, and the lasers are allowed to pass back through the irises to confirm optimal alignment. (b) Metallic mirror is placed on front of the beams, then the beams allowed to be reflected back and forth through irises until overlapping of the two beams was achieved.

Since the performance of the STED microscope relies on overlapping of the excitation and depletion beam extra care needed to adapted collinearity of both beams. So in addition of the back reflection protocol described above another two irises with small opening was used to send both the excitation and depletion beams through the irises as illustrated in Figure 6-13(b), a back and forth reflection gives longer propagation length for the alignment. Therefore, a passage through both irises of the alignment bath

in Figure 6-14(b) and observing the back reflection presence on the irises Figure 6-14(a) was considered positive proof for high degree of coarse alignment. And to make sure one have a symmetric Gaussian beam a digital camera was used to observe the beam shape, Figure 6-14(a) and (b). In addition, the digital camera was used to image and observe the collinearity of the two beams in real-time as shown in Figure 6-14(c), those images and intensity profile adds a positive proof for high degree of beams alignment.

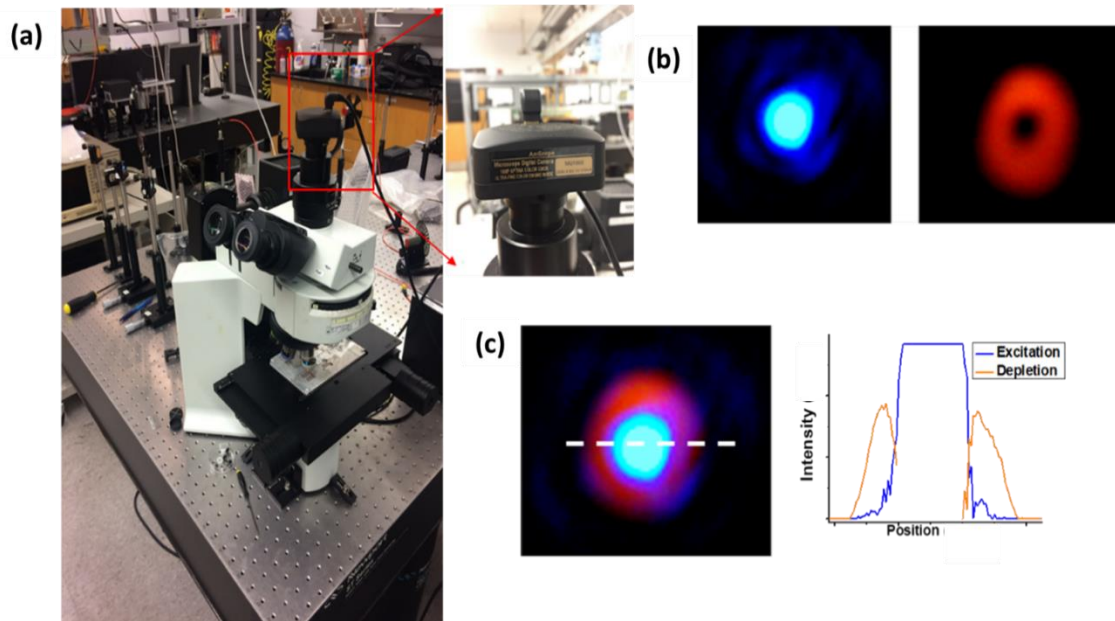


Figure 6-14: (a) Digital camera is used to image both beams. (b) Symmetric of the two beams can be monitored overtime using the digital camera. (c) Overlapping of the two beams also monitored in real-time using the digital camera mounted on the microscope.

## 6.4. Quantitative Investigation of Photobleaching and Background Reduction using Modulated STED Microscopy

### 6.4.1. Sample preparation

#### 6.4.1.1. *Fluorophore sample preparation*

For validation of the modulated STED approach a sample of carboxylate modified fluorospheres beads with a typical size of 20 nm (F8787, Thermofisher scientific, Waltham, Massachusetts, USA) was used, those beads features an absorption peak at 505 nm and a maximum fluorescence emission at 515 nm. Details on beads sample preparation can be found in Appendix 12.

#### 6.4.1.2. *Biological sample preparation*

The STED system was tested using retinal slices with fluorescently labeled structures as a biological sample, the samples were prepared by Prof. Maureen A. McCall labs from the Department of Ophthalmology and Visual Sciences at the University of Louisville. Details on those sample preparations can be found in Appendix 13

### 6.4.2. Experimental validation of the photobleaching reduction using mod STED microscopy

All laser power measurements done for both modulated and CW beams were measured at the back aperture of the objective and the power values averaged over time.

#### 6.4.2.1. *Effect of the excitation beam on photobleaching rate*

Using the setup operating under conventional CW confocal and modulated confocal (both with no depletion beam) the effect of modulating the excitation beam on photobleaching rate was tested. To reach this goal several parameters of the excitation

beam effect on the photobleaching rate was studied. Specifically, the frequency of modulation under AC modulation, the average excitation power under CW and AC modulation and the scan speed. It was found that an excitation power of  $\sim 16 \mu\text{W}$  under CW confocal imaging of the 20 nm beads sample has a weak enough excitation intensity level with negligible photobleaching. At the same time, an excitation power of  $16 \mu\text{W}$  implies a reasonable fluorescence rate that maximize fluorescence signal under scanning parameters with dwell time of  $75 \mu\text{s}$  and pixel size of 15 nm, see Figure 6-15(a). CW confocal images obtained using excitation power less than  $16 \mu\text{W}$  were fade and high photobleaching effect observed when imaging with excitation irradiance higher than  $16 \mu\text{W}$ . One can observe that those results set tight constraints for efficiently operating with a CW excitation beam.

To test the effect of modulating the excitation beam with AC signal at different frequencies on photobleaching rate, an average excitation power of  $16 \mu\text{W}$  was used to operate under modulated confocal configuration at different modulation frequencies, results shown in Figure 6-15(b). Under modulated confocal imaging setup, a bandwidth pass filter was set in the current preamplifier to help remove any DC signal component from the collected fluorescent signal before being sent to the lock-in amplifier. The integration time in the lock-in amplifier and the pixel dwell time (set by on the LabView code) were match to avoid aliasing effects. During those measurements the values of the integration time ( $100 \mu\text{s}$ ), band pass filter on the current preamplifier (10-300 kHz) and the pixel dwell time ( $100 \mu\text{s}$ ) was set in accordance to the lowest frequency of modulation deployed for the laser, which was 20 kHz. According to the experimental results summarized in Figure 6-15(b), modulating the excitation beam has a little impact on

photobleaching rate. However, it is very important to notice that in contrast to higher modulation frequencies in order for low modulation frequencies to overcome aliasing effect from the lock-in amplifier longer integration times is needed which increase the exposure time and then increase the photobleaching rate. These observations are confirmed by the data shown in Figure 6-15(c) where the modulation frequency (95 kHz) and average power (16  $\mu$ W) were fixed but the dwell time (and the matched lock-in amplifier integration time) was varied. Therefore, it is of great advantage to use high enough frequency of modulation combined with a small dwell time to minimize photobleaching effects. Figure 6-15(d) shows a comparison of photobleaching effect between CW confocal mode and modulated confocal configuration at different excitation powers, it can be noticed that there is a negligible difference on photobleaching rate when using CW confocal or modulated confocal configurations.



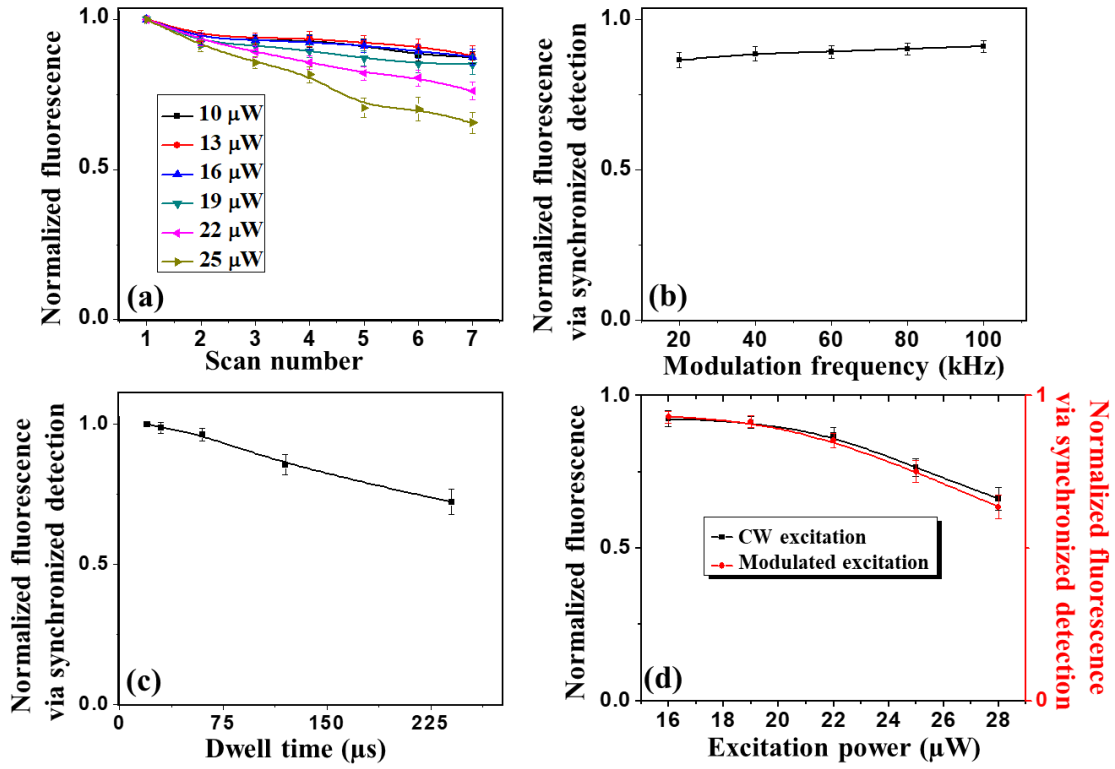


Figure 6-15: (a) Normalized fluorescence signal as a function of the number of scans for different CW excitation powers in the confocal imaging configuration. Each data point represents the average of normalized intensities of five different beads; for each bead the normalized intensity was calculated as  $I_i/I_1$ , where  $I_1$  represents the intensity of a particular bead at the first confocal image and  $I_i$  refers to its intensity at the  $i$ -th image. For all images at a particular excitation power, the dwell time (75  $\mu\text{s}$ ), the pixel size (15 nm), and the scan area were kept constant. For each different excitation power, a different scan spot was adopted. (b) Normalized fluorescent signal in modulated confocal imaging as a function of the modulation frequency at an average power of 16  $\mu\text{W}$ , a dwell time of 100  $\mu\text{s}$ , and a pixel size of 15 nm. For each modulation frequency, a different scan spot was adopted. (c) Normalized fluorescent signal in modulated confocal imaging

as a function of the dwell time at an average power of 16  $\mu\text{W}$ , a pixel size of 15 nm, and a modulation frequency of 95 kHz. For each dwell time, a different scan spot was adopted.

(d) Normalized fluorescent signal in both CW confocal and AC modulated confocal (95 kHz) as a function of the average excitation power at a dwell time of 100  $\mu\text{s}$  and a pixel size of 15 nm. For each average excitation power, a different scan spot was adopted. In Figs. (b, c, and d), each data point represents the average of normalized intensities of five different fluorescent beads and for each bead the normalized fluorescence intensity was calculated as  $I_5/I_1$ , where  $I_1$  is the intensity measured in the first scan and  $I_5$  is the intensity after the same area was scanned five times.

As mentioned previously, confocal images constructed under CW excitation with power lower than 10  $\mu\text{W}$  and small excitation time were faded due to low signal to noise ratio (SNR). However, as shown in Figure 6-16 imaging with a modulated excitation laser combined with synchronous detection the fluorescence signal is filtered and amplified using the lock-in amplifier, which results in an increase in the SNR compared to the corresponding CW confocal image.

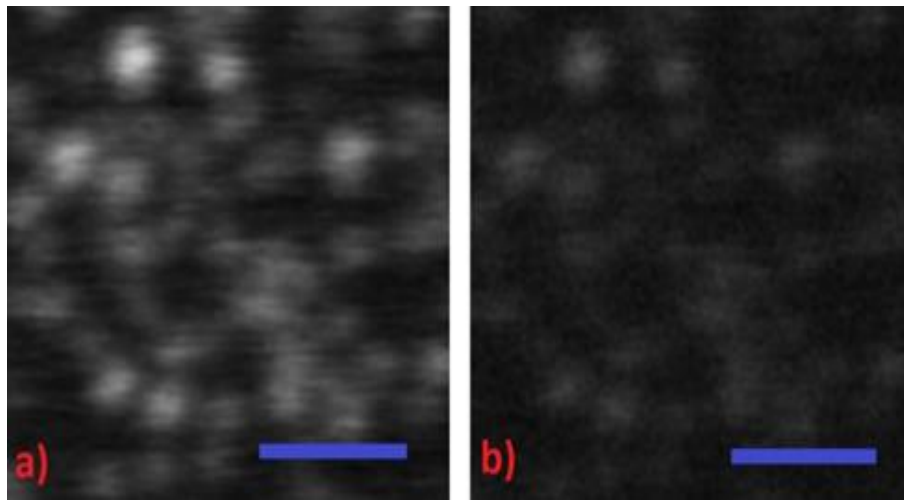


Figure 6-16: A side-by-side comparison of carboxylate fluorescent beads 20 nm recorded in the (a) modulated confocal and (b) CW confocal configurations at excitation power of 7  $\mu$ W. Beads are not well recorded in the CW confocal image, but recorded with better SNR in the modulated confocal recordings. Scale bar in both images is 1  $\mu$ m. In both images pixel size and dwell time were set to be 15 nm and 30  $\mu$ s, respectively.

In summary, confocal imaging at high modulation, short dwell time and low excitation power may lead to a reduction in the photobleaching rate. In contrary, CW confocal imaging aimed reduce photobleaching by decreasing the dwell time and the excitation power will cause a reduction in the fluorescence signal and leads to a low contrast image features.

#### *6.4.2.2. Effect of applying excitation and depletion beam simultaneously on photobleaching rate*

Based on the above conclusions the effect of applying the excitation and depletion beams simultaneously on photobleaching rate using modulated STED and CW STED modes was investigated. A comparison study was performed of the detected fluorescence on the 20 nm beads sampled as a function of the depletion laser irradiance. During those measurements, the phase plate was not mounted and in accordance to the results presented in Figure 6-15 an average optical power of 16  $\mu$ W for the 488 nm excitation laser beam was applied for both modulated STED and CW STED measurements. First, an image was acquired with only the excitation beam present; next the depletion beam was added and a second image was taken. For each bead, the fluorescence signal measured in the second image was normalized with respect to the fluorescence signal obtained in the first image. Figure 6-17 shows the normalized fluorescence intensity

decay as a function of depletion power, where each data point shown corresponds to the average normalized fluorescence signal of five different beads after exposed to different depletion intensities. As shown in Figure 6-17 applying modulated STED shows less photobleaching effect compared to CW STED and this effect increases with the increase of the depletion power. As previously noticed in Figure 6-15(d), without the depletion beam applied a negligible photobleaching effect observed between CW confocal and modulated confocal configurations, but when applying a depletion beam as shown in Figure 6-17 photobleaching becomes more severe, and more severe as the depletion power increased especially when the excitation laser is at a CW operation. It has been reported [125] that the population of the excited triplet state drastically changes with the modulation of the excitation beam, as the modulation of the excitation beam allows spontaneous relaxation of the excited fluorophore between two excitation pulses and this lead to a reduction in the triplet state population. A higher populations in the triplet state enhances the probability of photobleaching [126] and this probability of photobleaching becomes more severe as the depletion power increased and affects the excited fluorophore [127]. Therefore, in case of modulated STED, the population of triplet state affected by the depletion beam is less than in case of using a CW STED, thereby using modulated STED can be beneficial to avoid the pile up of triplet state population and its excitation to further reactive states due to the high depletion beam power applied.

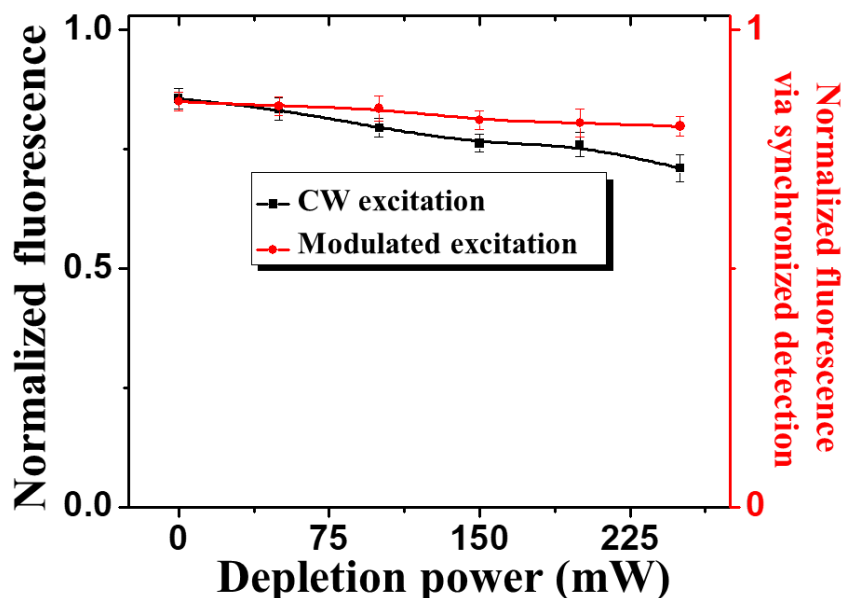


Figure 6-17: The normalized fluorescence intensity when overlapping two Gaussian beams: one for the excitation and one for the depletion; black curve corresponds to CW excitation beam and red curve corresponds to AC modulated excitation beam. Different scan areas were adopted for the CW and modulated excitation approaches. Also, each specific intensity in the depletion beam was performed at a different scan area. For all data points, the dwell time (100  $\mu$ s) and the pixel size (15 nm) were kept constant.

#### 6.4.2.3. Efficiency of depleting the fluorescence state with modulated STED and CW STED

A key performance for the STED microscopy is the efficiency of depleting the fluorescent state with minimum spurious noise. The fluorescence reduction for different depletion intensities measured on 20 nm carboxylate modified beads samples at the modulated STED setup and CW STED setup is presented in Figure 6-18. For those measurements, a diluted bead samples embedded in TDE or Vectashield were used.

Again the measurements for the fluorescence reduction done without the phase plate in the depletion beam path. For the modulated STED measurements the excitation beam was modulated at 95 kHz, the depletion beam was kept at CW operation and a bandwidth pass filter of 30-100 kHz was set in the current preamplifier. The fluorescence signal of a single bead irradiated with the excitation light with an average power of either 7  $\mu$ W or 16  $\mu$ W was recorded as the intensity of the depletion beam was varied from low (zero) to high values. Then the fluorescence signal at recorded at each depletion power was normalized to the fluorescence signal detected when the bead irradiated only with the excitation beam. Figure 6-18 shows a substantial background signal detected at high depletion powers in the CW STED configuration, this background signal becomes larger when the beads samples are embedded in a medium (Vectashield) whose index of refraction mismatches the index of refraction of the glass cover slit. On the other hand, also shown in Figure 6-18 when using the modulated STED scheme to image beads embedded in Vectashield media the background noise generated by the depletion beam was eliminated, the fluorescence signal was filtered and fluorescence reduction decrease as one increase the power of the depletion beam. In the CW STED configuration at low excitation power  $\sim 7$   $\mu$ W it was barely possible to record a fluorescence signal; data is not shown. However, in the modulated STED configuration at excitation power of 7  $\mu$ W a fluorescence signal was effectively recorded and the featured signal reduction was effectively recorded as the depletion beam power was increased. Results in Figure 6-18 under modulated STED at depletion power of 150 mW shows that the remaining fluorescence at AC modulated excitation power of 7  $\mu$ W ( $<12\%$ ) is less than the remaining fluorescence under modulated STED with excitation power of 16  $\mu$ W ( $>22\%$ ).

It is known that the depletion beam at lower excitation powers is more efficient and effective, so under modulated STED the capability to collect images at lower excitation and depletion powers will also contribute in the reduction of photobleaching effect in STED imaging.

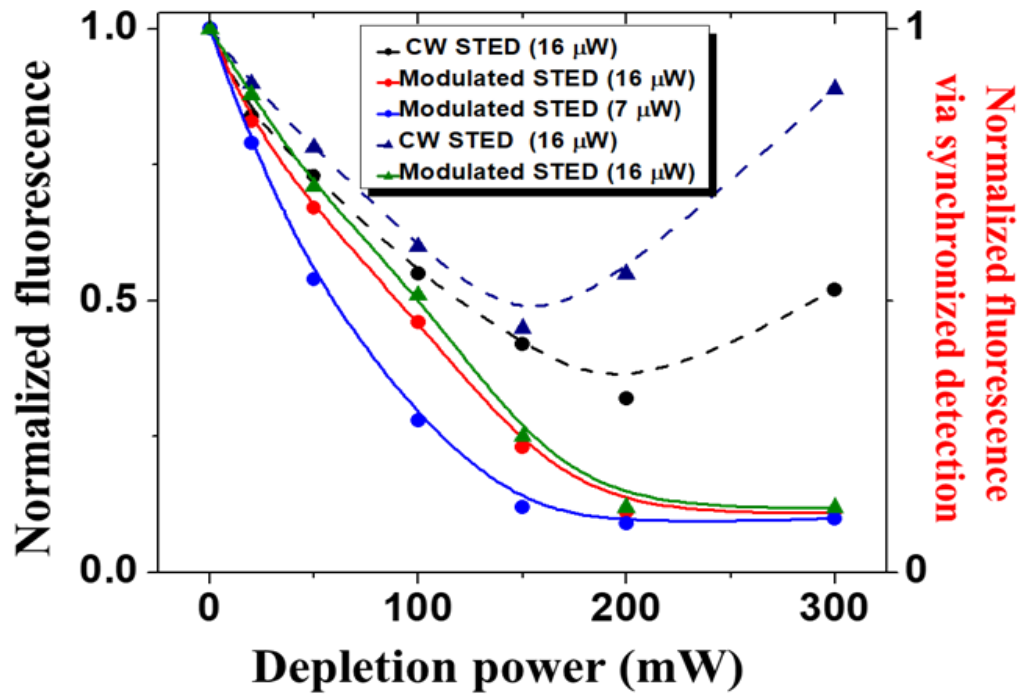


Figure 6-18: Fluorescence reduction for different STED intensities measured on the 20 nm carboxylate modified beads samples with both the modulated STED (solid) and CW STED (dashed) configurations at two different excitation powers of 7  $\mu$ W and 16  $\mu$ W (as indicated in brackets), and different embedding medium TDE (circles) and Vectashield (triangles).

#### *6.4.2.4. Super-resolution imaging using modulated STED and CW STED setups*

For the images discussed and shown below, the phase plate was mounted in the optical bath of the depletion beam to shape the beam in the desired doughnut-shaped profile. First, the setup operating under the conventional CW confocal was compared with CW STED configurations using the 20 nm carboxylate modified fluorospheres samples embedded in TDE. The excitation wavelength for both configurations was at 488 nm. For the CW STED configuration, a depletion beam at the wavelength of 592 nm was used. The dwell time was set to be 30  $\mu$ s with a pixel size of 15 nm. The power measured at the entrance aperture of the microscope objective lens was 16  $\mu$ W for the excitation beam and 270 mW for the depletion beam. Image Pro Plus and Origin software were used for handling the acquired images. Resolution estimation was performed based on statistical measurements of the full-width at half-maximum (FWHM) of a lorentzian fitted curve of the intensity profile for more than 5 different single particles of each image. The CW confocal image is shown in Figure 6-19(a) to be compared with the CW STED image shown in Figure 6-19(b). As shown in Figure 6-19(d), CW confocal imaging showed an estimate resolution of about 190 nm (within the diffraction limit, as expected). Same statistical resolution estimation was carried out for CW STED and the estimated average size of the 20 nm beads in CW STED configuration was 83 nm. Undesirable background effects appeared when one has increased the depletion power beyond this point in an attempt to improve (reduce) the point spread function Figure 6-19(c).



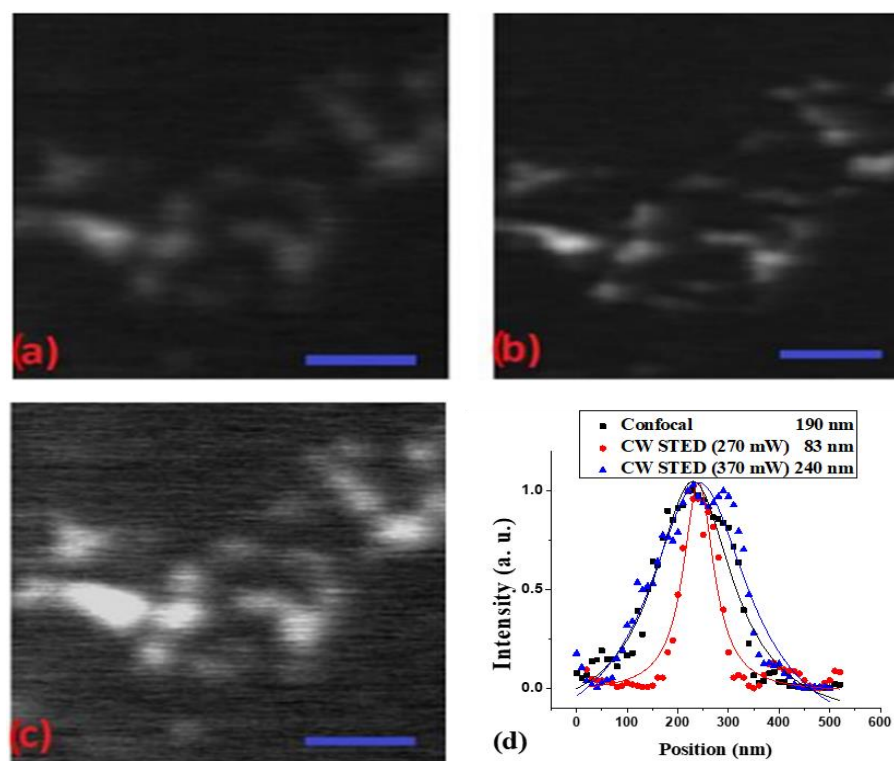


Figure 6-19: A side-by-side comparison of carboxylate modified fluorescent beads recorded in the (a) CW confocal and (b) CW STED configurations. Closely-spaced beads are not well-resolved in the CW confocal image, but are better discernible in the CW STED recordings. (c) Undesirable background effects appeared in CW STED configuration when the depletion power was increased to 370 mW. Scale bar in all images is 1  $\mu\text{m}$ . The normalized intensity profiles in (d) show the spatial resolution measured to be approximately 190 nm for the CW confocal image and about 83 nm for the CW STED image at 270 mW depletion power, and due to background signal at 370 mW in CW STED the estimated resolution measured was 240 nm.

Next, a modulated STED technique was applied to similar samples of the carboxylate modified fluorescent 20 nm beads. The average power for the excitation beam was kept at (16  $\mu\text{W}$ ) while the average depletion beam power was increased to 410

mW (as opposed to the previously 270 and 370 mW). The excitation beam was modulated at 95 kHz, while the depletion beam was kept at CW operation. A bandwidth pass filter of 30-100 kHz was set in the current amplifier to remove any DC signal component from the collected fluorescent signal before being sent to the lock-in amplifier. As previously mentioned, the integration time in the lock-in amplifier was set to be longer than one period of the modulation frequency, while the integration time and the pixel dwell time were matched to avoid aliasing effects. The dwell time was set to 30  $\mu$ s with a pixel size of 15 nm. For comparison, confocal image obtained under modulation of the excitation beam and without the presence of the depletion beam was collected and shown in Figure 6-20(a) as modulated confocal image. Figure 6-20(b) shows image of the modulated STED configuration with imaging parameters as described above. The average intensity profile of five different beads showed an approximate spatial resolution for the mod confocal of 192 nm as shown in Figure 6-20(e), which is similar and consistent with the diffraction-limited results described in Figure 6-20(d). However, the modulated STED image (Figure 6-20(b)) showed a point spread function of about 42 nm (Figure 6-20(e)) that represents a two-fold reduction compared to the CW STED data at lower depletion power (Figure 6-20(d)) and an approximate Five-fold improvement when confronted with either the CW confocal (Figure 6-20(d)) or modulated confocal (Figure 6-20(e)) techniques. It is worth mentioning that operating the depletion beam at higher power (410 mW, instead of 270 mW); the point spread function of the CW STED technique showed an increase in the background signal, (As noticed in Figure 6-19(c) compared to Figure 6-20(b)), which is probably caused by fluorophore excitation with the depletion beam or even back-scattered light of the

depletion beam from the sample under investigation. Because in modulated STED those detrimental effects from CW depletion beam are eliminated through a frequency filtering process a higher spatial resolution could be achieved. Also, as noticed in images shown in Figure 6-16, using synchronous detection the SNR can be improved and imaging at relatively low excitation power is possible in a mod confocal configuration. Using such low modulated excitation power was tested under modulated STED imaging, Figure 6-20(c) shows modulated STED image for the same carboxylate beads sample, except that the excitation beam power was set to be 7  $\mu$ W instead of 16  $\mu$ W and the depletion beam power was lowered to 310 mW. The lower power in modulated STED scan shows a statistical measured point spread function of 44 nm, which is approximately the same size as that observed in Figure 6-20(b) using a higher excitation and depletion beams average powers. In addition, the results in Figure 6-18 showed that the fluorescence reduction efficiency is higher under modulated STED configuration with relatively low excitation power. Figure 6-20(f) shows that imaging under modulated STED configuration at lower excitation power (Figure 6-20(c)) the estimated special resolution is lower than modulated STED imaging at higher excitation power (Figure 6-20(d)). Clearly, the modulated STED technique allows high resolution images to be achieved using lower power levels as compared to the CW STED methodology, those results are consistent with the conclusions and results presented in Figure 6-18. As mentioned earlier the ability to acquire super resolution imaging at low powers of excitation and depletion beams has also an advantage and a role in decreasing the photobleaching effect in single molecule super resolution imaging.

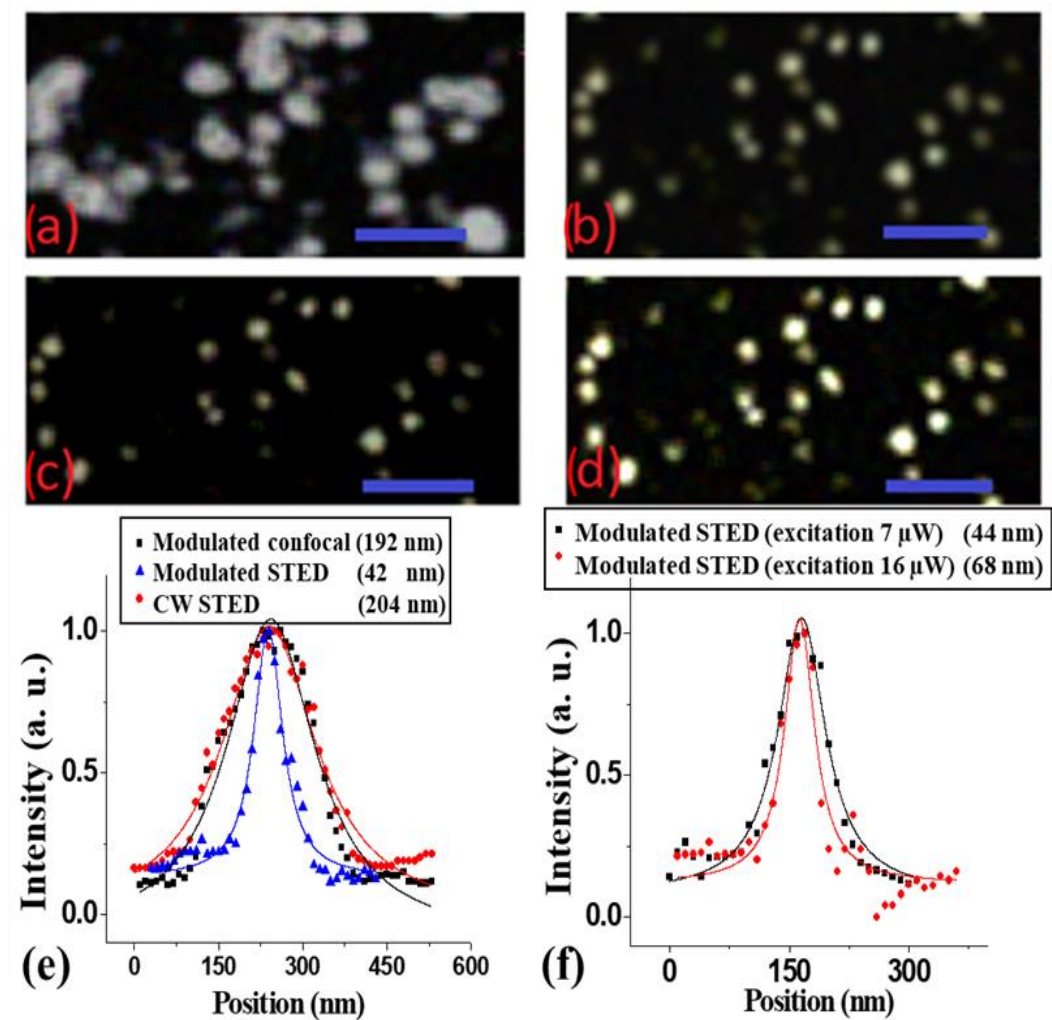


Figure 6-20: Comparison of (a) modulated confocal at excitation average power of 16  $\mu\text{W}$ , (b) modulated STED at excitation average power of 16  $\mu\text{W}$  and depletion average power of 410 mW, (c) modulated STED images at excitation average power of 7  $\mu\text{W}$  and depletion average power of 310 mW and (d) modulated STED images at excitation average power of 16  $\mu\text{W}$  and depletion average power of 310 mW of carboxylate modified 20 beads obtained for the same sample region. Scale bar is 500 nm for all images. (e) Normalized intensity profiles of the same bead in the three imaging configurations in (a) and (b) and for CW STED -image is not shown-. FWHM shown in the profiles were estimated based on a fitted lorentzian curve. The CW STED at a high

power level shows degradation in the spatial resolution compared to the results of the confocal image. On the other hand, the spatial resolution measured for the modulated STED image at (b) was approximately 44 nm and for the modulated confocal was about 192 nm, at excitation average power of 16  $\mu$ W and depletion average power of 410 mW. (f) Normalized intensity profiles of the same bead in the two images in (c) and (d) FWHM shown in the profiles were estimated based on a fitted lorentzian curve. The spatial resolution measured for the modulated STED image at excitation average power of 7  $\mu$ W and depletion average power of 310 mW was approximately 48 nm and for the modulated STED image at excitation average power of 16  $\mu$ W and depletion average power of 310 mW was approximately 68 nm.

Figure 6-21 show images for comparison of modulated confocal and modulated STED images of the 20 nm carboxylate modified fluorospheres when embedded in a medium (Vectashield) that creates a mismatch in refractive index against the sample under investigation. All parameters (pixel size, dwell time, modulation frequency) were the same as previously described. The excitation average power and depletion average power were 16  $\mu$ W and 350 mW, respectively. Super resolution STED imaging on such kind of samples is hardly possible in the CW STED configuration, Figure 6-21(b). The results shows that even under such conditions, modulated STED is still able to overcome adverse effects that would be observed due the mismatch in index of refraction between sample and embedding medium if an image is taken in modulated STED configuration, Figure 6-21(c). It is important to note that under modulated STED condition the back scattered light is still present and non-negligible, but the synchronous detection approach is able to filter out the undesirable background and only record the desired signal.

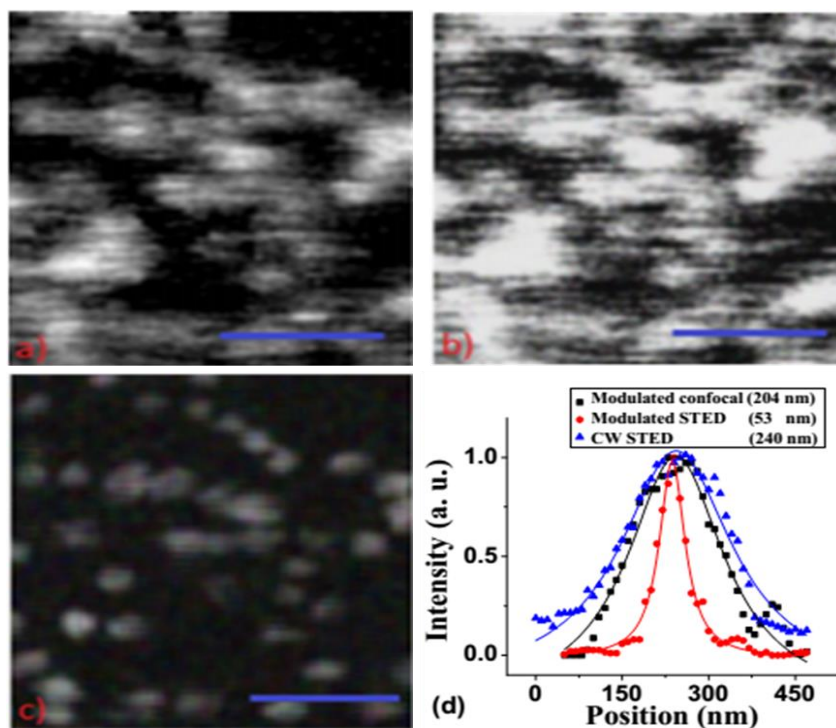


Figure 6-21: Comparison of the (a) modulated confocal and (b) CW STED images for the 20 nm carboxylate modified fluorospheres embedded in a medium (Vectashield) that creates a significant refractive-index contrast. (c) Modulated STED image for the 20 nm carboxylate modified fluorospheres embedded in a medium (Vectashield) same area as (a) and (b). Scale bar is 500 nm in all images. (d) The normalized intensity profiles of the same particles in the modulated STED image CW STED and its modulated confocal counterpart. The estimated average spatial resolution measured was about 190 nm for the modulated confocal image, around 53 nm for the modulated STED image and due to background effect 240 nm in CW STED.

#### 6.4.3. Applications of the constructed modulated and CW STED microscope at the University of Louisville

The demonstrated single-molecule super resolution imaging tool described above was used to study the effect of photobleaching and how one can decrease photobleaching

effect using synchronous detection. However, within the body of work describing the advantages of synchronous detection, the system built at University of Louisville can provide a promising pathway for furthering the research and increase the potential applications for users. Different applications and capabilities of the setup has already been demonstrated.

#### *6.4.3.1. Modulated STED super resolution imaging of biological samples*

To demonstrate the benefits of modulated STED for imaging biological samples, Figure 6-22 presents a side-by-side comparison of modulated confocal and modulated STED images of retinal slices with fluorescently labeled Alexa 488. The samples were embedded in TDE medium. For these results the average power measured in the entrance aperture of the objective lens was between 2.0-2.5  $\mu$ W for the excitation beam at 488 nm and 95 mW for the depletion beam at 592 nm. The pixel dwell-time was 30  $\mu$ s, the pixel size was 15 nm, and a modulation frequency of 85 kHz was deployed for the excitation beam. The data shows a clear improvement in optical resolution and in signal-to-background ratio using the modulated STED technique. Intensity line profiles of the smallest features in modulated STED images showed a FWHM of about 120 nm, as compared to the diffraction-limit resolution of about 210 nm for the modulated confocal. Antibody labeling those biological samples does not fill the cells completely and results in splotchy label [128], however those spots are clearly resolved in modulated STED image Figure 6-22(b).



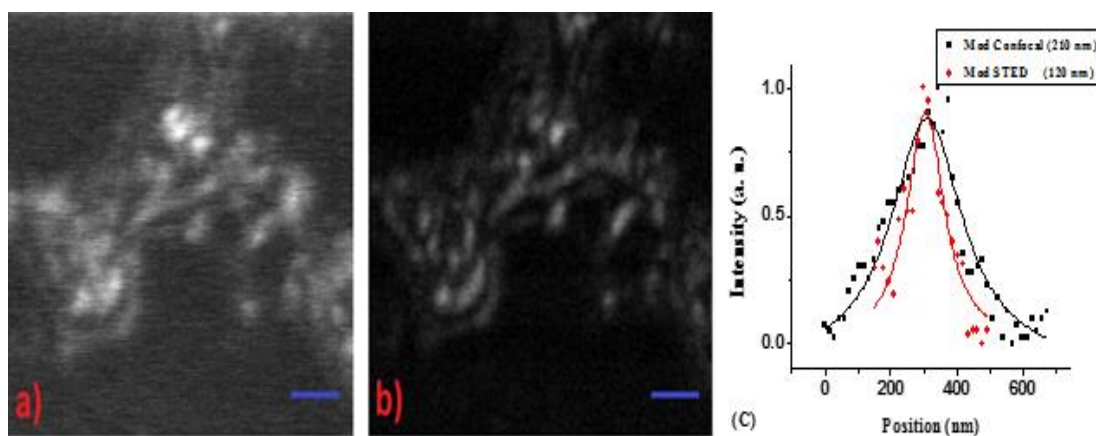


Figure 6-22: Imaging of retina bipolar cells (Gus-GFP-PNA) labeled with Alexa 488. Images from modulated confocal approach are shown in (a) and from modulated STED shown in (b). Special resolution of the smallest features presented in (c), where the black trace corresponds to the modulated confocal image and the red trace for the modulated STED. The modulated STED image demonstrates distinguishable particles that cannot be resolved by the modulated confocal imaging. Excitation average power used was about 2.0-2.5  $\mu$ W and depletion power was 95 mW. Pixel dwell time was set at 30  $\mu$ s. Scale bars in both images are 1  $\mu$ m.

#### 6.4.3.2. *Electrical imaging using STED microscope*

As previously described, STED fluorescent microscopy works by combining a doughnut-shaped depletion beam with an excitation beam lying along the donut zero. An additional capability add to the existing STED fluorescence imaging setup without hindering its functionality, an electronic microscope was developed which combines a depletion beam and an excitation beam in a similar way for fluorescence imaging with capacitance photocurrent measurements [129], where the detection mechanism is electrical rather than optical, which has been a joint project between Alphenaar research group (Electrical Computer Engineering Department at University of Louisville) and



Mendes Photonics Research Labs. The electrical detection mechanism is illustrated in Figure 6-23.

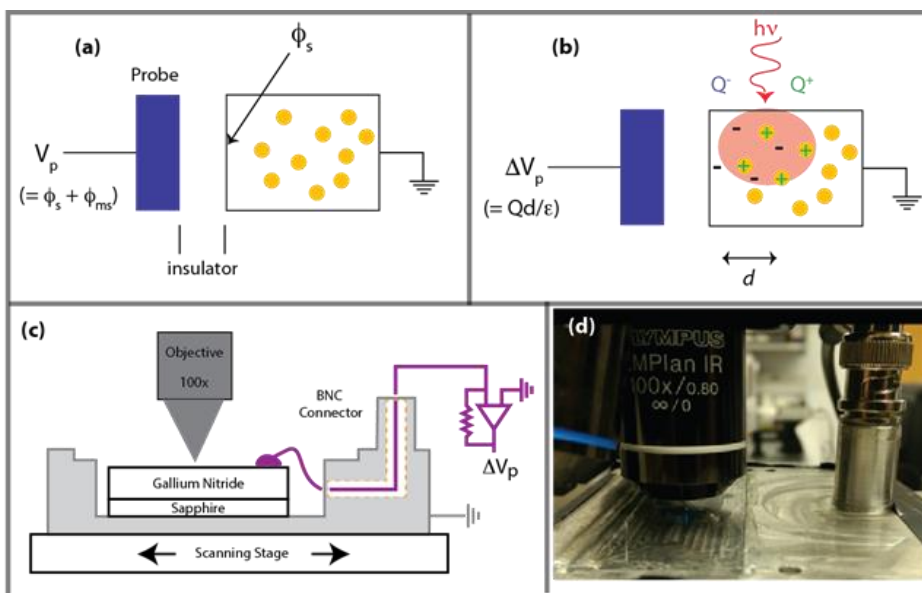


Figure 6-23: The scanning capacitive photocurrent technique used for STED electrical imaging. (a) When light incident on the sample it generates separated charge pairs, (b) an additional potential is created, which to first approximation is given by  $\Delta V_p = \frac{Qd}{\epsilon}$ . A pulsed light source then creates a measurable ac-voltage on the electrode. It is referring to the photo-generated electrical signal as capacitive photocurrent. (c) Measurement set-up including sample holder for STED electrical imaging (d) Photo showing objective and sample holder.

#### 6.4.3.3. Single molecule spectroelectrochemical imaging

The idea is to use the constructed STED configuration to reach single molecule spectroelectrochemical detection. A homemade flow-cell configuration as illustrated in Figure 6-24(a) is mounted in the sample holder with a standard three electrodes (working electrode ITO film on cover slit, platinum wire as a counter electrodes, and a Ag/AgCl

**(a)** Schematic diagram of the electrochemical cell. The cell consists of a working electrode (ITO-coated thin cover slide) immersed in an analytical solution. A gasket is used to seal the cell. A reference electrode (Ag/AgCl) and a counter electrode (Pt wire) are also present. A fluorophore sample is adsorbed on the ITO surface. An objective lens (100x, NA=1.35) is positioned above the cell for STED microscopy.

**(b)** Schematic diagram of the STED microscopy setup and data acquisition system. The setup includes a STED laser, an excitation laser, a phase mask, a detector, a current amplifier, a lock-in amplifier, a voltage amplifier, a potentiostat, an oscilloscope, and a computer. The STED laser and excitation laser are directed through a phase mask and objective lens onto the sample. The detector collects the signal, which is then amplified by a current amplifier and a voltage amplifier. The amplified signal is sent to a lock-in amplifier for phase and amplitude measurement. The potentiostat controls the electrochemical cell, and the oscilloscope displays the signal. The computer controls the entire system.

## 6.5. Conclusions

129

pattern of an excitation beam. The strong dependence of the spatial resolution on the depletion beam power in CW STED imaging can cause undesirable background signals and a damaging effect on many fluorophores in general. By applying an excitation modulated STED approach, which filters the fluorescence signal and eliminates undesirable background effects by means of synchronous detection with a lock-in amplifier, a single molecule spatial resolution that is consistent with conventional STED microscope [119] by deploying relatively low power levels for both the depletion and excitation beams can be reached. Applying low power levels in single molecule STED imaging can lead to a reduction in photobleaching effects. Also the photobleaching rate in STED imaging is decreased by modulating the excitation beam, and the photobleaching effect reduction in the modulated STED configuration is more notable at higher levels of depletion irradiance compared to CW STED imaging. Also in addition to addressing the photobleaching effect several other applications of the modulated STED is possible including imaging sensitive biological samples, electrical imaging and single molecule imaging spectroelectrochemical applications. Despite rapid advances and availability of high power lasers, their costs are still high. Therefore, the ability to reach high spatial resolutions with relatively low power levels is certainly of great interest. The lower laser intensity in modulated STED opens the possibility for new STED microscopy implementations based on a modulated laser source that reduces complexity and costs.

## CHAPTER 7 SUMMARY AND OUTLOOK

### 7.1. Summary

Two photonic tools were developed and applied to advance molecular interrogation at the nanoscale. A single-mode, electro-active, integrated optical waveguide platform was shown to provide a novel analytical tool of extremely high sensitivity for spectroscopic measurements. A potential-modulated optical signal was used to study adsorption, binding kinetics, and electron-transfer processes of a model redox protein adsorbed onto different molecular assemblies of a modified electrode. The experimental results using the SM-EA-IOW proved that the novel tool has the capability to retrieve the mechanisms of electron-transfer, molecular binding, and affinity strength of redox species adsorbed on different interfaces of a multilayer stack which can better bridge the analytical signals required in bio-sensing applications. From those lessons, a novel bio-sensing technology based on the combination of a single-mode electro-active integrated optical waveguide with a biological immunoassay displaying redox activity was developed. The electrically-controlled optical transduction was experimentally demonstrated for biological materials and a remarkable limit of detection in the picomolar range for the influenza virus antigen was achieved. The transduction mechanism of the bio-photonic device is also highly selective as the monitored analytical signal is optically and electrochemically locked to the probe tailored for interrogation. The

benefits of these selective factors was further demonstrated with authentic clinical samples and the novel technology showed remarkable consistency with state-of-the-art tests. Such performance using the SM-EA-IOW and the demonstrated detection capabilities has the potential to create a new bio-sensing technology capable of offering substantially shorter detection times with simpler and more cost-effective protocols, which are critical for point-of-care applications in disease diagnostics.

Single-molecule imaging in general and spectroscopic measurements at the single molecular level typically suffer from two main challenges, the diffraction limit and photobleaching effects. A super-resolution imaging technique was built and an ingenious approach was developed by applying modulated optical excitation in the STED technique. The fluorescent signal of interest, which is filtered in the frequency domain by means of synchronous detection, is free of many undesirable background effects and can be detected with high fidelity at much lower levels. A direct consequence of such an approach is that the average optical power in both the AC modulated excitation beam and the CW depletion beam can be substantially diminished without negative impact on the image quality. It was shown that spatial resolutions consistent with a conventional STED microscope can be achieved by deploying relatively lower power levels for both the excitation and depletion beams. Those lower power levels under the AC modulated STED technique have a direct benefit in reducing photobleaching effects. Experimental results evidenced that the photobleaching rate in STED imaging is decreased by modulating the excitation beam. In addition, the usefulness of the modulated STED technique in reducing the applied laser power for imaging sensitive biological samples was demonstrated. Typically, biological samples may feature unwanted back-scattered

background from a strong depletion beam under conventional CW STED imaging due to local mismatches in refractive index. The modulated STED technique is shown to be helpful in overcoming those difficulties as well. Despite rapid advances and availability of high power lasers, their costs are still high. Therefore, the ability to reach high spatial resolutions with relatively low power levels is certainly of great interest. The lower laser intensity in modulated STED opens the possibility for new STED microscopy implementations based on a modulated laser source that reduces complexity and costs.

## 7.2. Outlook

Based on the advances reported here, several studies from molecular assemblies to single molecule detection can be performed for fundamental research and to improve performance of many current technologies. The SM-EA-IOW proved to be a highly performing platform that showed exceptional sensitivity and selectivity. Such results already encourages several applications and to broaden even further its applicability several aspects should be developed including strategies for integration of the bio-sensor with lab-on-a-chip approaches to facilitate their performance, achieve higher sensitivity, and to micro-fabricate sensitive and specific array of sensors. Additional work to improve the proposed modulated-electrofluorochromic bio-sensing methodology is of high interest to materialize the envisioned benefits of arrayed detection. As an outlook for single molecule modulated-STED imaging, it would be of high interest to apply multicolor STED microscopy. Another very interesting possibility would be to further link the high resolution spatial information provided by STED microscopy to single molecule immunoassay detection based on electrofluorochromic bio-sensing detection.

## REFERENCES

1. Grieshaber, D., et al., *Electrochemical Biosensors - Sensor Principles and Architectures*. Sensors, 2008. **8**(3): p. 1400.
2. Lippa, P.B., L.J. Sokoll, and D.W. Chan, *Immunosensors—principles and applications to clinical chemistry*. Clinica Chimica Acta, 2001. **314**(1): p. 1-26.
3. Gopinath, S.C.B., et al., *Current aspects in immunosensors*. Biosensors and Bioelectronics, 2014. **57**(Supplement C): p. 292-302.
4. Fowler, J.M., et al., *CHAPTER 5 - Recent developments in electrochemical immunoassays and immunosensors A2 - Zhang, Xueji*, in *Electrochemical Sensors, Biosensors and their Biomedical Applications*, H. Ju and J. Wang, Editors. 2008, Academic Press: San Diego. p. 115-143.
5. Pei, X., et al., *Sandwich-type immunosensors and immunoassays exploiting nanostructure labels: A review*. Analytica Chimica Acta, 2013. **758**(Supplement C): p. 1-18.
6. Amano, Y. and Q. Cheng, *Detection of influenza virus: traditional approaches and development of biosensors*. Analytical and Bioanalytical Chemistry, 2005. **381**(1): p. 156-164.
7. Place, J.F., R.M. Sutherland, and C. Dähne, *Opto-electronic immunosensors: A review of optical immunoassay at continuous surfaces*. Biosensors, 1985. **1**(4): p. 321-353.
8. Ross, S.E., et al., *Spectroelectrochemical sensing: planar waveguides*. Electrochimica Acta, 2003. **48**(20): p. 3313-3323.
9. Wang, J., *CHAPTER 3 - Electrochemical glucose biosensors*, in *Electrochemical Sensors, Biosensors and their Biomedical Applications*. 2008, Academic Press: San Diego. p. 57-69.
10. Wang, H., G. Shen, and R. Yu, *CHAPTER 9 - Aspects of recent development of immunosensors*, in *Electrochemical Sensors, Biosensors and their Biomedical Applications*. 2008, Academic Press: San Diego. p. 237-260.
11. Hassanpour, S., et al., *Recent trends in rapid detection of Influenza infections by Bio and nanobiosensor*. TrAC Trends in Analytical Chemistry.
12. Nguyen, B.T.T., et al., *Electrochemical impedance spectroscopy characterization of nanoporous alumina dengue virus biosensor*. Bioelectrochemistry, 2012. **88**(Supplement C): p. 15-21.
13. Sapsford, K.E., *Total-Internal-Reflection Platforms for Chemical and Biological Sensing Applications*, in *Optical Guided-wave Chemical and Biosensors I*, M. Zourob and A. Lakhtakia, Editors. 2009, Springer Berlin Heidelberg: Berlin, Heidelberg. p. 3-20.
14. Mukundan, H., et al., *Waveguide-Based Biosensors for Pathogen Detection*. Sensors, 2009. **9**(7): p. 5783.

15. Kale, R.R., et al., *Detection of Intact Influenza Viruses using Biotinylated Biantennary S-Sialosides*. Journal of the American Chemical Society, 2008. **130**(26): p. 8169-8171.
16. Chauhan, S., et al., *Evanescent Wave Absorption Based S-shaped Fiber-optic Biosensor for Immunosensing Applications*. Procedia Engineering, 2016. **168**: p. 117-120.
17. Carlborg, C.F., et al., *A packaged optical slot-waveguide ring resonator sensor array for multiplex label-free assays in labs-on-chips*. Lab on a Chip, 2010. **10**(3): p. 281-290.
18. Lu, J., et al., *Plasmonic-Based Electrochemical Impedance Spectroscopy: Application to Molecular Binding*. Analytical Chemistry, 2012. **84**(1): p. 327-333.
19. Guo, X., *Surface plasmon resonance based biosensor technique: A review*. Journal of Biophotonics, 2012. **5**(7): p. 483-501.
20. Halliwell, J., et al., *Electrochemical impedance spectroscopy biosensor for detection of active botulinum neurotoxin*. Sensing and Bio-Sensing Research, 2014. **2**(Supplement C): p. 12-15.
21. Jarocka, U., et al., *Electrochemical immunosensor for detection of antibodies against influenza A virus H5N1 in hen serum*. Biosensors and Bioelectronics, 2014. **55**(Supplement C): p. 301-306.
22. Chung, D.-J., K.-C. Kim, and S.-H. Choi, *Electrochemical DNA biosensor based on avidin–biotin conjugation for influenza virus (type A) detection*. Applied Surface Science, 2011. **257**(22): p. 9390-9396.
23. Protsailo, L.V. and W.R. Fawcett, *Electrochemical Impedance Spectroscopy at Alkanethiol-Coated Gold in Propylene Carbonate*. Langmuir, 2002. **18**(23): p. 8933-8941.
24. Al-Kutubi, H., et al., *Electrofluorochromic systems: Molecules and materials exhibiting redox-switchable fluorescence*. European Polymer Journal, 2016. **83**: p. 478-498.
25. Dallaire, A.-M., et al., *Electrochemical plasmonic sensing system for highly selective multiplexed detection of biomolecules based on redox nanoswitches*. Biosensors and Bioelectronics, 2015. **71**(Supplement C): p. 75-81.
26. Juan-Colás, J., et al., *The electrophotonic silicon biosensor*. Nature Communications, 2016. **7**: p. 12769.
27. Dixon, M.C., *Quartz Crystal Microbalance with Dissipation Monitoring: Enabling Real-Time Characterization of Biological Materials and Their Interactions*. Journal of Biomolecular Techniques : JBT, 2008. **19**(3): p. 151-158.
28. Hansen, W.N., T. Kuwana, and R.A. Osteryoung, *Observation of electrode-solution interface by means of internal reflection spectrometry*. Analytical Chemistry, 1966. **38**(13): p. 1810-1821.
29. Kuwana, T. and W.R. Heineman, *Study of electrogenerated reactants using optically transparent electrodes*. Accounts of Chemical Research, 1976. **9**(7): p. 241-248.
30. Bradshaw, J.T., et al., *Broadband Coupling into a Single-Mode, Electroactive Integrated Optical Waveguide for Spectroelectrochemical Analysis of Surface-Confin ed Redox Couples*. Analytical Chemistry, 2003. **75**(5): p. 1080-1088.



31. Doherty, W.J., et al., *Potential-Modulated, Attenuated Total Reflectance Spectroscopy of Poly(3,4-ethylenedioxythiophene) and Poly(3,4-ethylenedioxythiophene Methanol) Copolymer Films on Indium–Tin Oxide*. The Journal of Physical Chemistry B, 2006. **110**(10): p. 4900-4907.
32. Araci, Z.O., et al., *Potential-Modulated Attenuated Total Reflectance Characterization of Charge Injection Processes in Monolayer-Tethered CdSe Nanocrystals*. The Journal of Physical Chemistry Letters, 2010. **1**(12): p. 1900-1905.
33. Sagara, T., et al., *Voltammetric application of electromodulated electoreflection absorption spectroscopy: electoreflectance voltammetry as an in situ spectroelectrochemical technique*. Langmuir, 1991. **7**(5): p. 1005-1012.
34. Dunphy, D.R., et al., *The Electroactive Integrated Optical Waveguide: Ultrasensitive Spectroelectrochemistry of Submonolayer Adsorbates*. Analytical Chemistry, 1997. **69**(15): p. 3086-3094.
35. Feng, Z.Q., T. Sagara, and K. Niki, *Application of potential-modulated UV-visible reflectance spectroscopy to electron transfer rate measurements for adsorbed species on electrode surfaces*. Analytical Chemistry, 1995. **67**(19): p. 3564-3570.
36. Matsuda, N., et al., *Spectroelectrochemical studies on surface immobilized cytochrome c on ITO electrode by slab optical waveguide spectroscopy*. Thin Solid Films, 2003. **438-439**(Supplement C): p. 403-406.
37. Han, X. and S.B. Mendes, *Optical Impedance Spectroscopy with Single-Mode Electro-Active-Integrated Optical Waveguides*. Analytical Chemistry, 2014. **86**(3): p. 1468-1477.
38. Borisov, S.M. and O.S. Wolfbeis, *Optical Biosensors*. Chemical Reviews, 2008. **108**(2): p. 423-461.
39. Strianese, M., et al., *Fluorescence-Based Biosensors*. Vol. 875. 2012. 193-216.
40. Weber, G. and F.W.J. Teale, *Fluorescence excitation spectrum of organic compounds in solution. Part 1.-Systems with quantum yield independent of the exciting wavelength*. Transactions of the Faraday Society, 1958. **54**(0): p. 640-648.
41. Zhang, J., et al., *Creating new fluorescent probes for cell biology*. Nature Reviews Molecular Cell Biology, 2003. **4**: p. 80.
42. Lei, C., D. Hu, and E.J. Ackerman, *Single-molecule fluorescence spectroelectrochemistry of cresyl violet*. Chemical Communications, 2008(43): p. 5490-5492.
43. Peterson, E.M. and J.M. Harris, *Imaging Fluorescent Nanoparticles To Probe Photoinduced Charging of a Semiconductor–Solution Interface*. Langmuir, 2013. **29**(38): p. 11941-11949.
44. Palacios, R.E., et al., *Single-Molecule Spectroelectrochemistry (SMS-EC)*. Journal of the American Chemical Society, 2006. **128**(28): p. 9028-9029.
45. Abbe, E., VII.—*On the Estimation of Aperture in the Microscope*. Journal of the Royal Microscopical Society, 1881. **1**(3): p. 388-423.
46. Zang, L., et al., *A Single-Molecule Probe Based on Intramolecular Electron Transfer*. Journal of the American Chemical Society, 2002. **124**(36): p. 10640-10641.

47. Hill, C.M., D.A. Clayton, and S. Pan, *Combined optical and electrochemical methods for studying electrochemistry at the single molecule and single particle level: recent progress and perspectives*. Physical Chemistry Chemical Physics, 2013. **15**(48): p. 20797-20807.
48. Heilemann, M., *Fluorescence microscopy beyond the diffraction limit*. Journal of Biotechnology, 2010. **149**(4): p. 243-251.
49. Gustafsson, M.G.L., *Nonlinear structured-illumination microscopy: Wide-field fluorescence imaging with theoretically unlimited resolution*. Proceedings of the National Academy of Sciences of the United States of America, 2005. **102**(37): p. 13081-13086.
50. Rust, M.J., M. Bates, and X. Zhuang, *Sub-diffraction-limit imaging by stochastic optical reconstruction microscopy (STORM)*. Nat Meth, 2006. **3**(10): p. 793-796.
51. Hell, S.W., *Microscopy and its focal switch*. Nat Meth, 2009. **6**(1): p. 24-32.
52. Hell, S.W. and J. Wichmann, *Breaking the diffraction resolution limit by stimulated emission: stimulated-emission-depletion fluorescence microscopy*. Optics Letters, 1994. **19**(11): p. 780-782.
53. Hein, B., K.I. Willig, and S.W. Hell, *Stimulated emission depletion (STED) nanoscopy of a fluorescent protein-labeled organelle inside a living cell*. Proceedings of the National Academy of Sciences, 2008. **105**(38): p. 14271-14276.
54. Chakrova, N., et al., *Adaptive illumination reduces photobleaching in structured illumination microscopy*. Biomedical Optics Express, 2016. **7**(10): p. 4263-4274.
55. Patterson, G., et al., *Superresolution Imaging using Single-Molecule Localization*. Annual review of physical chemistry, 2010. **61**: p. 345-367.
56. Lu, X., et al., *Towards single molecule biosensors using super-resolution fluorescence microscopy*. Biosensors and Bioelectronics, 2017. **93**: p. 1-8.
57. Alberto Diaspro, G.C., Cesare Usai, Paola Ramoino, and a.J. Dobrucki, *Photobleaching*, in *Handbook of Biological Confocal Microscopy*, J.B. Pawley, Editor. 2006, Springer Science+Business Media, LLC.; New York, USA. p. 690-702.
58. Amos, W.B. and J.G. White, *How the Confocal Laser Scanning Microscope entered Biological Research*. Biology of the Cell, 2003. **95**(6): p. 335-342.
59. Song, L., et al., *Photobleaching kinetics of fluorescein in quantitative fluorescence microscopy*. Biophysical Journal, 1995. **68**(6): p. 2588-2600.
60. Alberto Diaspro, G.C., Cesare Usai, Paola Ramoino, and a.J. Dobrucki, *Photobleaching*, in *Handbook of Biological Confocal Microscopy*, J.B. Pawley, Editor. 2006, Springer Science+Business Media: New York.
61. Ronzitti, E., B. Harke, and A. Diaspro, *Frequency dependent detection in a STED microscope using modulated excitation light*. Optics Express, 2013. **21**(1): p. 210-219.
62. Feng, Z.Q., et al., *Electroreflectance spectroscopic study of the electron transfer rate of cytochrome c electrostatically immobilized on the  $\omega$ -carboxyl alkanethiol monolayer modified gold electrode*. Journal of Electroanalytical Chemistry, 1995. **394**(1): p. 149-154.
63. Qiang Feng, Z., et al., *Long-range electron-transfer reaction rates to cytochrome c across long- and short-chain alkanethiol self-assembled monolayers:*

- Electroreflectance studies*. Journal of the Chemical Society, Faraday Transactions, 1997. **93**(7): p. 1367-1370.
64. Gaigalas, A.K. and G. Niaura, *Measurement of Electron Transfer Rates between Adsorbed Azurin and a Gold Electrode Modified with a Hexanethiol Layer*. Journal of Colloid and Interface Science, 1997. **193**(1): p. 60-70.
  65. Han, X., *Novel analytical tools for studies in molecular assemblies : I. Electro-active single-mode integrated optical waveguides ; II. Coupled plasmon waveguide resonances.*, in *Electronic Theses and Dissertations*. 2014, University of Louisville: USA.
  66. Aslan, M.M., et al., *Low-loss optical waveguides for the near ultra-violet and visible spectral regions with Al<sub>2</sub>O<sub>3</sub> thin films from atomic layer deposition*. Thin Solid Films, 2010. **518**(17): p. 4935-4940.
  67. Han, X. and S.B. Mendes, *Spectroelectrochemical properties of ultra-thin indium tin oxide films under electric potential modulation*. Thin Solid Films, 2016. **603**: p. 230-237.
  68. Karlsson, R., A. Michaelsson, and L. Mattsson, *Kinetic analysis of monoclonal antibody-antigen interactions with a new biosensor based analytical system*. Journal of Immunological Methods, 1991. **145**(1): p. 229-240.
  69. Saha, K., F. Bender, and E. Gizeli, *Comparative Study of IgG Binding to Proteins G and A: Nonequilibrium Kinetic and Binding Constant Determination with the Acoustic Waveguide Device*. Analytical Chemistry, 2003. **75**(4): p. 835-842.
  70. Han, X. and S.B. Mendes, *Electron-Transfer Rate in Potential-Modulated Redox Reactions with Electro-Active Optical Waveguides*. Analytical Sciences, 2017. **33**(4): p. 435-441.
  71. Avila, A., et al., *An Electrochemical Approach to Investigate Gated Electron Transfer Using a Physiological Model System: Cytochrome c Immobilized on Carboxylic Acid-Terminated Alkanethiol Self-Assembled Monolayers on Gold Electrodes*. The Journal of Physical Chemistry B, 2000. **104**(12): p. 2759-2766.
  72. Yue, H., et al., *On the Electron Transfer Mechanism Between Cytochrome c and Metal Electrodes. Evidence for Dynamic Control at Short Distances*. The Journal of Physical Chemistry B, 2006. **110**(40): p. 19906-19913.
  73. Murgida, D.H. and P. Hildebrandt, *Proton-Coupled Electron Transfer of Cytochrome c*. Journal of the American Chemical Society, 2001. **123**(17): p. 4062-4068.
  74. Wackerbarth, H. and P. Hildebrandt, *Redox and Conformational Equilibria and Dynamics of Cytochrome c at High Electric Fields*. ChemPhysChem, 2003. **4**(7): p. 714-724.
  75. Kausaite, A., et al., *Surface plasmon resonance label-free monitoring of antibody antigen interactions in real time*. Biochemistry and Molecular Biology Education, 2007. **35**(1): p. 57-63.
  76. Khoshtariya, D.E., et al., *Charge-Transfer Mechanism for Cytochrome c Adsorbed on Nanometer Thick Films. Distinguishing Frictional Control from Conformational Gating*. Journal of the American Chemical Society, 2003. **125**(25): p. 7704-7714.

77. Murgida, D.H. and P. Hildebrandt, *Electron-Transfer Processes of Cytochrome c at Interfaces. New Insights by Surface-Enhanced Resonance Raman Spectroscopy*. Accounts of Chemical Research, 2004. **37**(11): p. 854-861.
78. Croney, J.C., et al., *Conformational Dynamics and Temperature Dependence of Photoinduced Electron Transfer within Self-Assembled Coproporphyrin: Cytochrome c Complexes*. Biophysical Journal, 2003. **84**(6): p. 4135-4143.
79. Yue, H., et al., *Multiple Sites for Electron Tunneling between Cytochrome c and Mixed Self-Assembled Monolayers*. The Journal of Physical Chemistry C, 2008. **112**(7): p. 2514-2521.
80. Yue, H. and D.H. Waldeck, *Understanding interfacial electron transfer to monolayer protein assemblies*. Current Opinion in Solid State and Materials Science, 2005. **9**(1): p. 28-36.
81. Davis, K.L., et al., *Electron-Transfer Kinetics of Covalently Attached Cytochrome c/SAM/Au Electrode Assemblies*. The Journal of Physical Chemistry C, 2008. **112**(16): p. 6571-6576.
82. Bard, A.J. and L.R. Faulkner, *Electrochemical methods : fundamentals and applications*. 2nd ed. ed. 2001, New York :: Wiley.
83. Schmickler, W., *Interfacial Electrochemistry*. 1996, Oxford University Press, Inc: New York. p. 67-76.
84. Chatterjee Ganguly, S., *Biomolecular films—design, function and applications (Marcel Dekker Surfactant Science Series)*. Edited by JF Rusling. Marcel Dekker, New York, 2003. ISBN 0-8247-0899-7. pp 640. Polymer International, 2004. **53**(12): p. 2188-2188.
85. Niki, K., et al., *Coupling to Lysine-13 Promotes Electron Tunneling through Carboxylate-Terminated Alkanethiol Self-Assembled Monolayers to Cytochrome c*. The Journal of Physical Chemistry B, 2003. **107**(37): p. 9947-9949.
86. Wei, J.J., et al., *Probing Electron Tunneling Pathways: Electrochemical Study of Rat Heart Cytochrome c and Its Mutant on Pyridine-Terminated SAMs*. The Journal of Physical Chemistry B, 2004. **108**(43): p. 16912-16917.
87. Vashist, S.K., et al., *Immobilization of Antibodies and Enzymes on 3-Aminopropyltriethoxysilane-Functionalized Bioanalytical Platforms for Biosensors and Diagnostics*. Chemical Reviews, 2014. **114**(21): p. 11083-11130.
88. Aziz, M.A., S. Patra, and H. Yang, *A facile method of achieving low surface coverage of Au nanoparticles on an indium tin oxide electrode and its application to protein detection*. Chemical Communications, 2008(38): p. 4607-4609.
89. Kim, J., et al., *Formation, structure, and reactivity of amino-terminated organic films on silicon substrates*. Journal of Colloid and Interface Science, 2009. **329**(1): p. 114-119.
90. Akerström, B., et al., *Protein G: a powerful tool for binding and detection of monoclonal and polyclonal antibodies*. The Journal of Immunology, 1985. **135**(4): p. 2589-2592.
91. Schreurs, J., et al., *Electrochemical behaviour of horse-heart cytochrome-c*. Recueil des Travaux Chimiques des Pays-Bas, 1984. **103**(9): p. 263-269.
92. Fedurco, M., *Redox reactions of heme-containing metalloproteins: dynamic effects of self-assembled monolayers on thermodynamics and kinetics of*

- cytochrome c electron-transfer reactions*. Coordination Chemistry Reviews, 2000. **209**(1): p. 263-331.
93. Xiao, Y. and S.N. Isaacs, *Enzyme-linked immunosorbent assay (ELISA) and blocking with bovine serum albumin (BSA)—not all BSAs are alike*. Journal of Immunological Methods, 2012. **384**(1): p. 148-151.
  94. Lubin, A.A., et al., *Sequence-Specific, Electronic Detection of Oligonucleotides in Blood, Soil, and Foodstuffs with the Reagentless, Reusable E-DNA Sensor*. Analytical Chemistry, 2006. **78**(16): p. 5671-5677.
  95. Ding, F., et al., *Measuring the bioactivity and molecular conformation of typically globular proteins with phenothiazine-derived methylene blue in solid and in solution: A comparative study using photochemistry and computational chemistry*. Journal of Photochemistry and Photobiology B: Biology, 2016. **158**(Supplement C): p. 69-80.
  96. Beam, B.M., N.R. Armstrong, and S.B. Mendes, *An electroactive fiber optic chip for spectroelectrochemical characterization of ultra-thin redox-active films*. Analyst, 2009. **134**(3): p. 454-459.
  97. Imai, K., et al., *Simultaneous Multiselective Spectroelectrochemical Fiber-Optic Sensor: Demonstration of the Concept Using Methylene Blue and Ferrocyanide*. Analytical Chemistry, 2015. **87**(4): p. 2375-2382.
  98. Fujimoto, B.S., et al., *Fluorescence and Photobleaching Studies of Methylene Blue Binding to DNA*. The Journal of Physical Chemistry, 1994. **98**(26): p. 6633-6643.
  99. Sandhu, H.S., et al., *Diagnostic Utility of Quantitative Polymerase Chain Reaction versus Culture in Endophthalmitis and Uveitis*. Ocular Immunology and Inflammation, 2018: p. 1-5.
  100. Medicine, I.o., *Global Infectious Disease Surveillance and Detection: Assessing the Challenges—Finding Solutions: Workshop Summary*, ed. S.M. Lemon, et al. 2007, Washington, DC: The National Academies Press. 284.
  101. Lazcka, O., F.J.D. Campo, and F.X. Muñoz, *Pathogen detection: A perspective of traditional methods and biosensors*. Biosensors and Bioelectronics, 2007. **22**(7): p. 1205-1217.
  102. Velusamy, V., et al., *An overview of foodborne pathogen detection: In the perspective of biosensors*. Biotechnology Advances, 2010. **28**(2): p. 232-254.
  103. Massad-Ivanir, N., et al., *Porous Silicon-Based Biosensors: Towards Real-Time Optical Detection of Target Bacteria in the Food Industry*. Scientific Reports, 2016. **6**: p. 38099.
  104. Wilson, T., C.J.R. Sheppard, and K. Löschke, *Theory and practice of scanning optical microscopy*. Academic Press, London 1984, 213 Seiten, 138 Abbildungen, Preis \$ 39.50 ISBN 0-12-757760-2. Crystal Research and Technology, 1985. **20**(12): p. 1608-1608.
  105. Ferrando, M. and W.E.L. Spiess, *Review: Confocal scanning laser microscopy. A powerful tool in food science Revision: Microscopía láser confocal de barrido. Una potente herramienta en la ciencia de los alimentos*. Food Science and Technology International, 2000. **6**(4): p. 267-284.
  106. Wilson, T., *Resolution and optical sectioning in the confocal microscope*. Journal of Microscopy, 2011. **244**(2): p. 113-121.

107. Klar, T.A. and S.W. Hell, *Subdiffraction resolution in far-field fluorescence microscopy*. Optics Letters, 1999. **24**(14): p. 954-956.
108. Hell, S.W., *Nanoscopy with Focused Light (Nobel Lecture)*. Angewandte Chemie International Edition, 2015. **54**(28): p. 8054-8066.
109. Donnert, G., et al., *Two-Color Far-Field Fluorescence Nanoscopy*. Biophysical Journal, 2007. **92**(8): p. L67-L69.
110. Wildanger, D., et al., *A STED microscope aligned by design*. Optics Express, 2009. **17**(18): p. 16100-16110.
111. Fornasiero, E.F. and F. Opazo, *Super-resolution imaging for cell biologists*. BioEssays, 2015. **37**(4): p. 436-451.
112. Donnert, G., et al., *Macromolecular-scale resolution in biological fluorescence microscopy*. Proceedings of the National Academy of Sciences, 2006. **103**(31): p. 11440-11445.
113. Paschotta, R., *Field Guide to Lasers*. SPIE Field Guides, ed. J.E. Greivenkamp. Vol. FG12. 2008, USA: SPIE Press. 154.
114. Hell, S.W., *Strategy for far-field optical imaging and writing without diffraction limit*. Physics Letters A, 2004. **326**(1): p. 140-145.
115. Hell, S.W., *Toward fluorescence nanoscopy*. Nature Biotechnology, 2003. **21**: p. 1347.
116. Harke, B., et al., *Resolution scaling in STED microscopy*. Optics Express, 2008. **16**(6): p. 4154-4162.
117. Klar, T.A., et al., *Fluorescence microscopy with diffraction resolution barrier broken by stimulated emission*. Proceedings of the National Academy of Sciences, 2000. **97**(15): p. 8206-8210.
118. Wildanger, D., et al., *STED microscopy with a supercontinuum laser source*. Optics Express, 2008. **16**(13): p. 9614-9621.
119. Moneron, G., et al., *Fast STED microscopy with continuous wave fiber lasers*. Optics Express, 2010. **18**(2): p. 1302-1309.
120. Hell, S.W., M. Dyba, and S. Jakobs, *Concepts for nanoscale resolution in fluorescence microscopy*. Current Opinion in Neurobiology, 2004. **14**(5): p. 599-609.
121. Wu, Y., et al., *Resonant Scanning with Large Field of View Reduces Photobleaching and Enhances Fluorescence Yield in STED Microscopy*. 2015. **5**: p. 14766.
122. Vicidomini, G., et al., *Sharper low-power STED nanoscopy by time gating*. Nat Meth, 2011. **8**(7): p. 571-573.
123. Castello, M., et al., *Gated-sted microscopy with subnanosecond pulsed fiber laser for reducing photobleaching*. Microscopy Research and Technique, 2016. **79**(9): p. 785-791.
124. Willig, K.I., et al., *STED microscopy with continuous wave beams*. Nat Meth, 2007. **4**(11): p. 915-918.
125. Gatzogiannis, E., et al., *Observation of Frequency-Domain Fluorescence Anomalous Phase Advance Due to Dark-State Hysteresis*. The Journal of Physical Chemistry Letters, 2011. **2**(5): p. 461-466.
126. Song, L., et al., *Influence of the triplet excited state on the photobleaching kinetics of fluorescein in microscopy*. Biophys J, 1996. **70**(6): p. 2959-68.

127. Wu, Y., et al., *Reducing Photobleaching in STED Microscopy with Higher Scanning Speed*. Biophysical Journal. **108**(2): p. 477a.
128. Breuninger, T., et al., *Chromatic Bipolar Cell Pathways in the Mouse Retina*. The Journal of Neuroscience, 2011. **31**(17): p. 6504-6517.
129. Mohite, A., et al., *Displacement current detection of photoconduction in carbon nanotubes*. Applied Physics Letters, 2005. **86**(6): p. 061114.
130. <http://omlc.org/spectra/PhotochemCAD/html/047.html>.
131. Wurm, C.A., et al., *Sample Preparation for STED Microscopy*, in *Live Cell Imaging: Methods and Protocols*, D.B. Papkovsky, Editor. 2010, Humana Press: Totowa, NJ. p. 185-199.
132. Huang, L., et al., *G protein subunit G $\gamma$ 13 is coexpressed with G $\alpha$ , G $\beta$ 3, and G $\beta$ 4 in retinal ON bipolar cells*. The Journal of Comparative Neurology, 2003. **455**(1): p. 1-10.

## APPENDICES

### Appendix 1: Optical Impedance Spectroscopy Measurements

It should be noted that the wavelength for interrogation was selected in accordance to the wavelength with the largest molar absorptivity difference between the two redox states of Cyt-C, as shown in Figure 1.

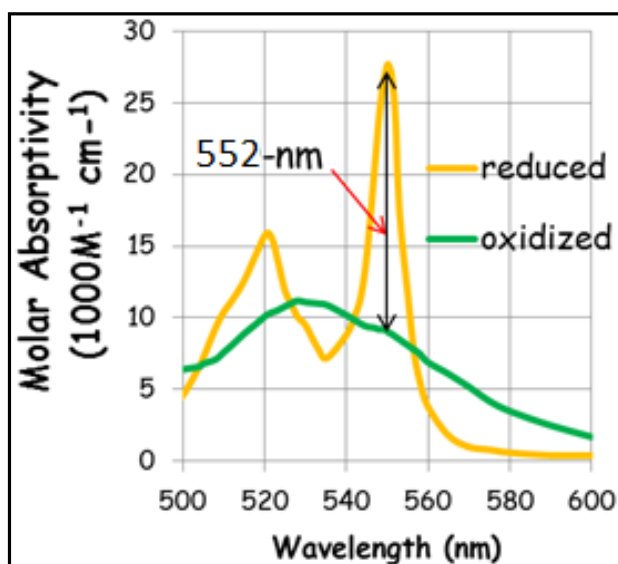


Figure 1: Molar absorptivity for the oxidized and the reduced states of Cyt-C proteins in the buffer solution. Cytochrome c proteins were reduced chemically using ascorbic acid in the solution environment.

To obtain the in-phase  $\Delta A'_{ac}$  and out-of-phase  $\Delta A''_{ac}$  impedance absorbance components described by the equations:



$$\Delta A'_{ac} = -\frac{\Delta I_{ac} \cos(\theta)}{I_{dc} \ln(10)} + \frac{\Delta I_{ac,0} \cos(\theta_0)}{I_{dc,0} \ln(10)} \quad \text{Equation 1}$$

$$\Delta A''_{ac} = -\frac{\Delta I_{ac} \sin(\theta)}{I_{dc} \ln(10)} + \frac{\Delta I_{ac,0} \sin(\theta_0)}{I_{dc,0} \ln(10)} \quad \text{Equation 2}$$

Under AC potential modulation described by  $E = E_{dc} + \Delta E_{ac} \sin(\omega t)$ , one need first to determine the formal potential  $E_{dc}$  of the redox active probe.

The data under cyclic voltammetry is collected with and without cytochrome c protein, Figure 2(a), from those data the absorbance can be measured and plotted vs potential as shown in Figure 2(b). A fit of the absorbance is shown in red trace; this fitting trace can be used to approximate the formal potential. The faradaic current from the absorbance can be retrieved using the equation  $i_F = \frac{n F v}{S \Delta \epsilon} \frac{dA}{dE}$ , since  $\frac{n F v}{S \Delta \epsilon}$  is a constant and only the formal potential is needed, a measured derivative of absorbance (A) with respect to the applied potential (E) is enough to determine the formal potential  $E_{dc}$ , blue curve Figure 2(b).

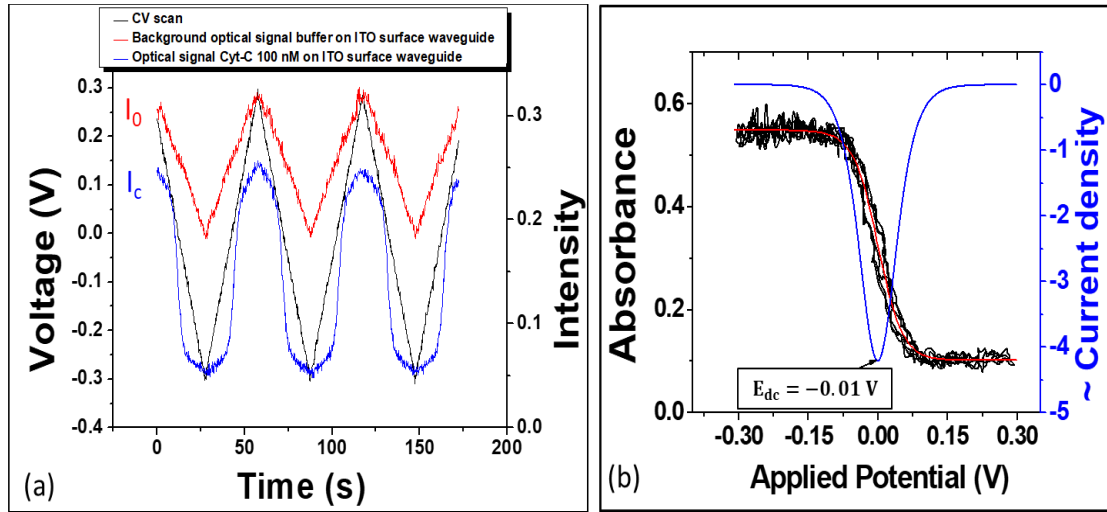


Figure 2: (a) The CV potential scan (black trace) and the optical signals, at 552 nm for the reference (red trace) and for the surface-adsorbed proteins (blue trace) plotted against time. (b) Absorbance data as measured by the SM-EA-IOW device for an adsorbed sub-

monolayer of Cyt-C protein undergoing CV potential modulation on ITO SM-EA-IOW surface (black trace) with curve fitted line (red trace) used to approximate the formal potential by measuring the current density (here the blue trace is only proportional to the current density).

After determining the formal potential one can apply an AC modulated signal at the formal potential, and collect the other components needed to calculate the in-phase and out-of-phase optical impedance absorbance. Figure 3 shows the sequence of data collection when an AC modulated potential is applied, both the baseline and sample optical data including the  $x$  and  $y$  component under synchronous detection is recorded. The  $x$  and  $y$  values represent the components indicated in the inset table (b) of Figure 3. The DC components  $I_{dc}$  and  $I_{dc,o}$  is calculated from averaging the recorded optical response. In the Figure 3(c) the dashed line represents an average obtained for  $I_{dc}$ .

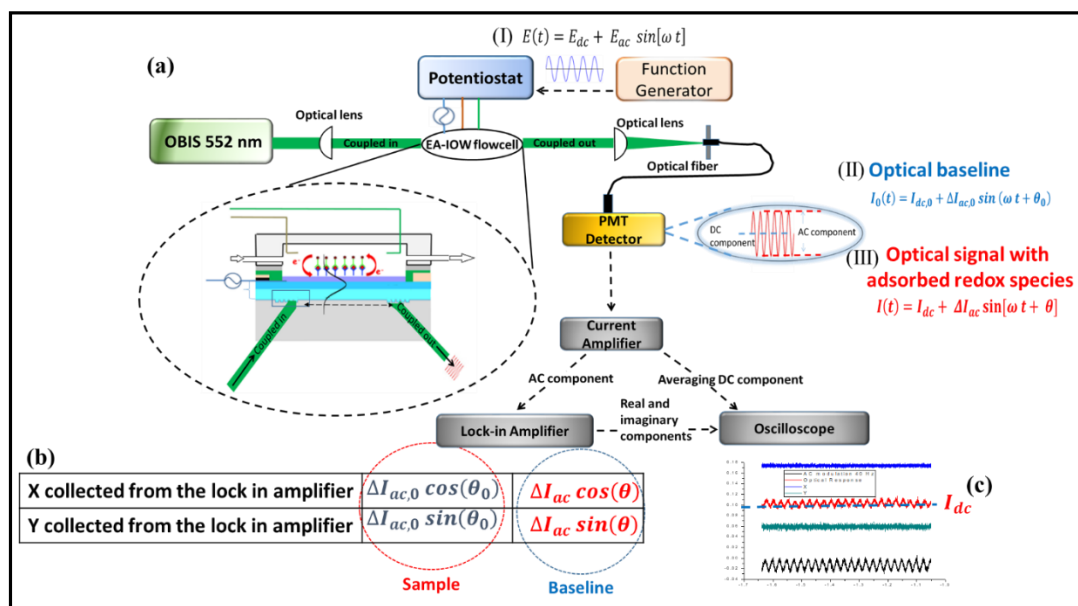


Figure 3: Experimental setup with steps shows data collection for an applied AC modulated potential, the baseline and sample optical signal is recorded on the

oscilloscope with traces for the x and y components obtained from the lock in amplifier under synchronous detection. The  $I_{dc,0}$  and  $I_{dc}$  component were obtained by directly averaging the optical signal for the baseline and sample, respectively. And the component as indicated in the inset table was obtained from the x and y signals by the lock-in amplifier.

With the above process for data collection at different frequencies, the components  $\Delta I_{ac} \sin(\theta)$ ,  $\Delta I_{ac} \cos(\theta)$ ,  $\Delta I_{ac,0} \cos(\theta_0)$ ,  $I_{dc}$  and  $I_{dc,0}$  is determined and one can measure the in-phase and out-of-phase components using equations as shown in Figure 4(a). The analyzed data can be schematically summarized in a complex plane plot as shown for Cyt-C on bare ITO SM-EA-IOW in Figure 4(b).

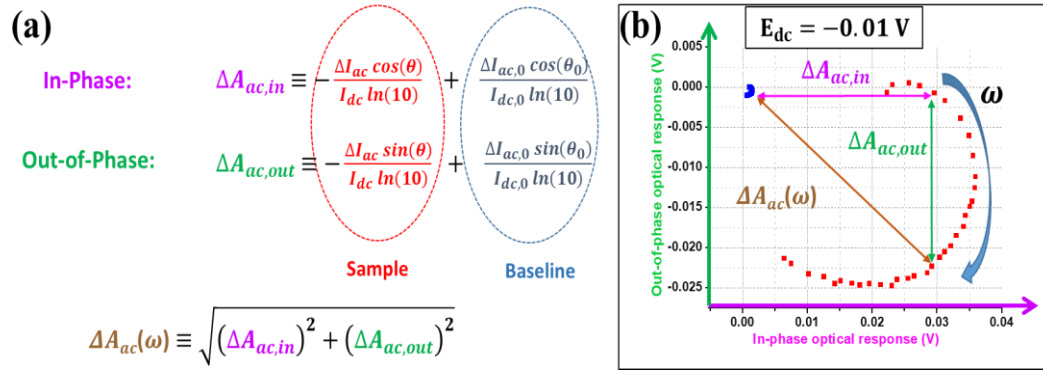


Figure 4: (a) Equation used to calculate the in-phase and out-of-phase components. (b) A complex plot of the in-phase and out-of-phase components of the baseline (blue) and the sample (red). Each point corresponds to a particular frequency, which increases clockwise from the smallest (1 Hz) to the largest (45 Hz). The mathematical equations in Figure (a) can be represented as follow: the amplitude of the AC absorbance,  $\Delta A_{ac}(\omega)$ , is described by the distance between two points with the same frequency, as schematically illustrated by the brown arrow. The horizontal distance between those two points (purple

arrow) corresponds to the in-phase component of the AC absorbance,  $\Delta A_{ac,in}$ , and the vertical distance corresponds to the out-of-phase component,  $\Delta A_{ac,out}$  (green arrow).

From the optical data collected above one can measure the current density using the following equation

$$I_F = \frac{nF}{S \times \Delta A_{ac}} \omega \Delta A_{ac}. \quad \text{Equation 3}$$

where  $\Delta A_{ac}$  is the absorbance amplitude,  $S$  is the sensitivity factor,  $\omega$  is the angular frequency,  $n$  is the number of electrons transferred in each redox event and  $F$  is the faradaic constant.

## Appendix 2: Calculating Electron Transfer rate $k_{ET}$ using Optical Impedance Spectroscopy

The generalized equivalent circuit of adsorbed redox molecules reacted on an electrode surface can be represented as shown in Figure 5, where  $Z_1$  and  $Z_2$  account for the electrolyte solution resistance and other possible electrical effects in the cell,  $R_s$  is the electrolyte solution resistance,  $E_{ac}$  represents the applied potential modulation provided by the potentiostat across the whole electrochemical cell, and  $E_{ac,F}$  is the actual potential modulation across the redox reaction. The charge transfer resistor  $R_{ct}$  in series with a pseudo capacitance  $C_a$  and the faradaic current is represented by  $I_F$  which is due to the faradaic chemical process.

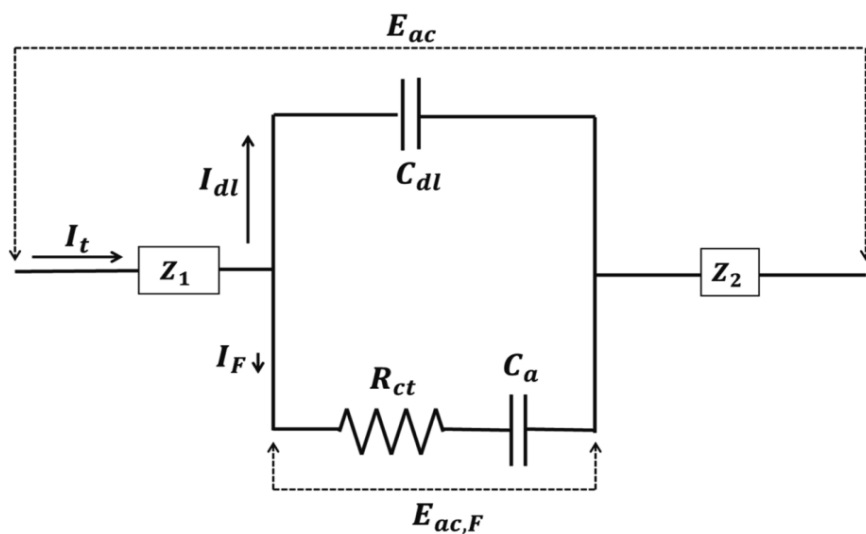


Figure 5: Equivalent electrical circuit for the electrochemical flow-cell of a redox active molecules on the working electrode surface.  $Z_1$  and  $Z_2$  are the generalized impedances. Under the total AC impedance  $E_{ac}$  across the entire flow cell,  $I_t$  is the total current density going through total impedance  $Z_{tot}$ . With the actual potential modulation  $E_{ac,F}$  applied on the redox molecules,  $I_F$  is the faradaic current density going through the

faradaic impedance from the redox reactions of the protein.  $I_{dl}$  is the current density going through double layer capacitance  $C_{dl}$ .

The analysis processes described below follow the same in a previous work. From the surface density,  $\Gamma_{ac} = \frac{\Delta A_{ac}(\omega)}{S \Delta \epsilon}$ , of the electro-active species, the associated faradaic current density can be determined by using the relation:

$$I_F(\omega) = j\omega n F \Gamma_{ac} \quad \text{Equation 4}$$

where  $S$  is a sensitivity factor (e.g.,  $S \cong 14,500$  for the SM-EA-IOW device),  $\Delta \epsilon$  is the difference in molar absorptivity between the two oxidation states,  $n$  is the number of electrons involved in the redox process, and  $F$  is the Faraday constant. And whenever  $I_F \ll I_{dl}$  the admittance of the faradaic process,  $Y_F(\omega)$ , can be described by the following equation:

$$Y_F(\omega) = j \frac{\omega C_{dl} A_{eff}}{E_{ac}} Z_t(\omega) I_F(\omega) \quad \text{Equation 5}$$

where  $A_{eff}$  is the effective area of the working electrode. By substituting Equation 3 into Equation 4 one can come up with

$$Y_F'(\omega) = - \frac{n F \omega^2 C_{dl} A_{eff}}{S \Delta \epsilon E_{ac}} \times \{ (Z_{tot}'(\omega) \Delta A'_{ac}(\omega) + Z_{tot}''(\omega) \Delta A''_{ac}(\omega)) + j (Z_{tot}'(\omega) \Delta A''_{ac}(\omega) + Z_{tot}''(\omega) \Delta A'_{ac}(\omega)) \} \quad \text{Equation 6}$$

For the described electrochemical reaction,  $k_{ET}$  can be expressed as

$$k_{ET} = \frac{1}{2 C_a R_{ct}} = \frac{\omega Y_F''(\omega)}{2 Y_F'(\omega)} \quad \text{Equation 7}$$

Where

$$Y'_F(\omega) = -\frac{nF\omega^2 C_{dl} A_{eff}}{S \Delta \epsilon E_{ac}} [Z'_{tot}(\omega) \Delta A'_{ac}(\omega) - Z''_{tot}(\omega) \Delta A''_{ac}(\omega)] \quad \text{Equation 8}$$

$$Y''_F(\omega) = -\frac{nF\omega^2 C_{dl} A_{eff}}{S \Delta \epsilon E_{ac}} [Z'_{tot}(\omega) \Delta A''_{ac}(\omega) + Z''_{tot}(\omega) \Delta A'_{ac}(\omega)] \quad \text{Equation 9}$$

And by defining

$$x(\omega) = 2[Z'_{tot}(\omega) \Delta A'_{ac}(\omega) - Z''_{tot}(\omega) \Delta A''_{ac}(\omega)] \quad \text{Equation 10}$$

and

$$y(\omega) = \omega [Z'_{tot}(\omega) \Delta A''_{ac}(\omega) + Z''_{tot}(\omega) \Delta A'_{ac}(\omega)] \quad \text{Equation 11}$$

Then by inserting Equation 10 and Equation 11 into Equation 7, one can use a parametric plot of  $y(\omega)$  against  $x(\omega)$ . The values of the total electrical impedance obtained from the potentiostat are shown in Figure 6.

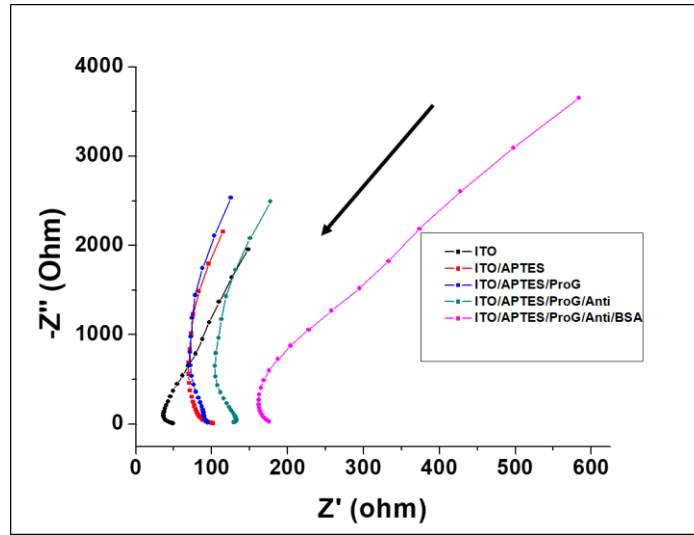


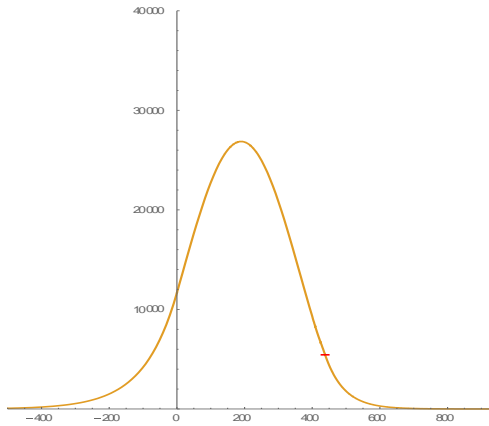
Figure 6: The real and imaginary electrical impedance measurements obtained using a potentiostat in the frequency range (1 Hz to 45 Hz), low frequency to high frequency as indicated with the black arrow.

Appendix 3: The Sensitivity for Guided Waveguide Mode, for the TE Polarization  
Incident Light with  $\lambda = 552$  nm and  $\lambda = 610$  nm.

A Mathematica program code, where details elsewhere can be found in [65], was used for sensitivity calculations with parameters as follow:

$$(I) \quad \lambda = 552; n_c = 1.33; n_1 = 1.88; t_1 = 13; n_2 = 1.46; t_2 = 16; a = 1.64576; b = 42.89898; c = 308958233.142; n_3 = a+b/(\lambda^2)+c/(\lambda^4); t_3 = 409; n_s = 1.51; \beta = 1.589598680435842$$

distribution field intensity

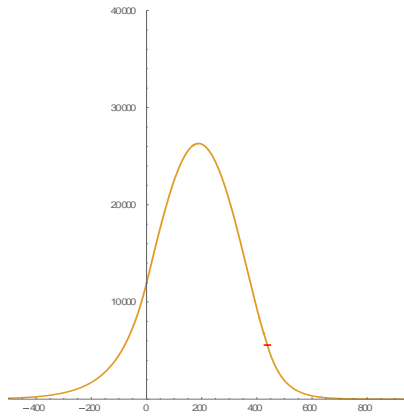


Sensitivity = {14543.174371315871} this sensitivity is for waveguides with 2.45 cm grating separation.

$$(II) \quad \lambda = 610; n_c = 1.33; n_1 = 1.88; t_1 = 13; n_2 = 1.46; t_2 = 16; a = 1.64576; b = 42.89898; c = 308958233.142; n_3 = a+b/(\lambda^2)+c/(\lambda^4); t_3 = 409; n_s = 1.51; \beta = 1.586725242145626$$

distribution field intensity





Sensitivity = {18566.181389836439} this sensitivity is for waveguides with 3.4 cm grating separation.

#### Appendix 4: AC Potential Modulation Parameters for Binding Kinetics Measurements of Cyt-C.

As discussed in Appendix 1, the absorbance amplitude is maximized when the AC modulated potential is set around the formal potential and a resonant frequency. As shown in Figure 7(a) there was no major shift in the formal potential of Cyt-C at the different immunolayers. However, there is an obvious change in the resonant frequency, Figure 7(b), a fixed frequency when measuring the absorbance amplitude for kinetic study will have no major effect on the binding constants, this is because the main data set needed is only the change in surface binding.

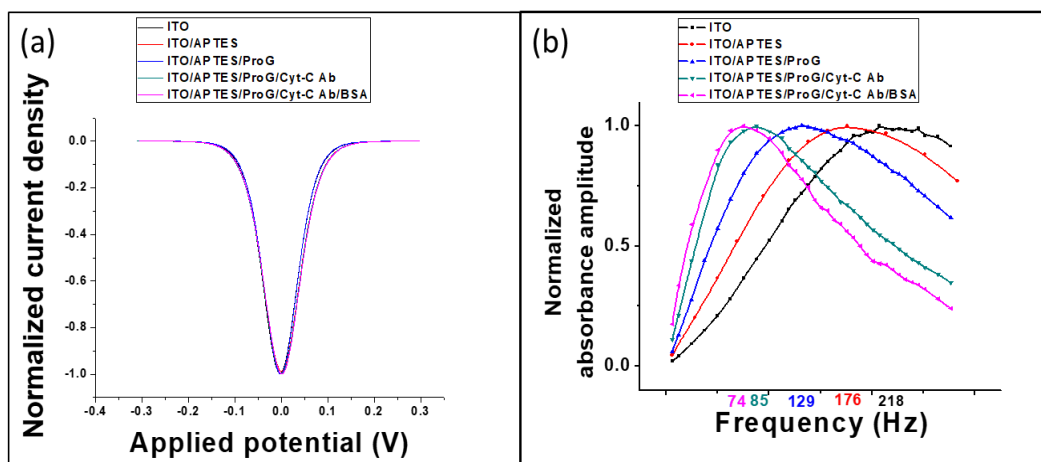


Figure 7: (a) The normalized current density as a function of potential at different functionalized immunolayers, the current density was obtained from the derivative of curve fitting from the absorbance under CV potential modulation, and then each curve was normalized to its maximum current density value. As noticed there is no major change in the formal potential as immunolayers functionalized on the SM-EA-IOW surface. (b) The normalized amplitude of the AC absorbance for Cyt-C 100 nM,  $\Delta A_{ac}$ , against the frequency for an AC amplitude modulation of 10 mV at -10 mV DC bias

potentials at different functionalized bio-immunolayers, a shift in the frequency where the maximum absorbance amplitude is observed upon the functionalization of the SM-EA-IOW.

## Appendix 5: Confocal imaging Characterization of Immunolayers Functionalized on the SM-EA-IOW Surface

The bio-layers should be bound to the surface with specific chemical, electrical or optical properties. Self-assembled monolayers (SAMs) are one means of modifying the surface of immunosensors to promote and immobilize bio-interphases using several methods including covalent attachment, physical adsorption or electrostatic interaction. External confocal optical imaging was used to evaluate the build-up of the bio-immunolayers assembly. The fluorescent confocal images of the functionalized layers evidenced the dense, complete and homogeneous morphology of the functionalized layers on the SM-EA-IOW device surface.

### 1. APTES

The density of surface-immobilized binding sites is an important factor for the control of surface properties and development of sensors. The APTES layer functionalized on the ITO surface was characterized by labeling the amine groups of APTES with fluorescent molecules. Imaging the single molecules with confocal fluorescent microscopy, provided a means to determine the presence and reactivity of the APTES layer on the SM-EA-IOW device. Carboxylate-modified fluorescent beads (Yellow–Green (505/515), F8787, Thermo-Fisher Scientific) diluted to ( $\sim 1: 10^3$ ) in PBS, with a typical size of about 20 nm, were bound to the surface amine sites. Samples of ITO and ITO/APTES were incubated in PBS solution of the carboxylate-modified fluorescent beads for 30 minutes, then sonicated for 10 minutes in DI water, and dried with N<sub>2</sub>.

Figure 8 shows a side-by-side comparison between ITO and ITO/APTES surfaces, and clearly demonstrates a significant difference between the affinity of ITO and ITO/APTES surfaces to bind the carboxylate-modified beads, which indicates the successful functionalization, presence and reactivity of the APTES on the ITO surface.

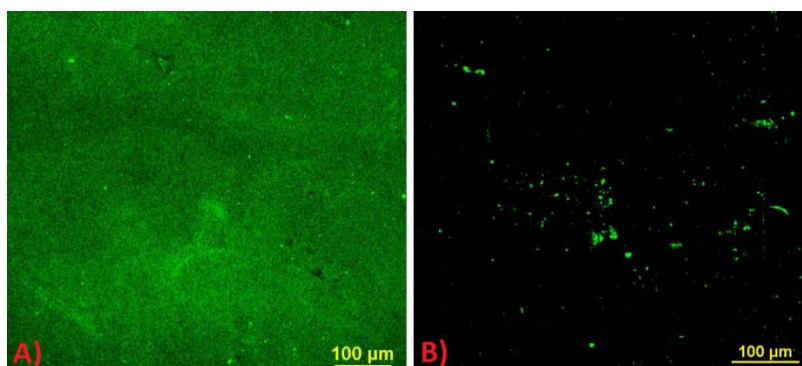


Figure 8: Confocal images of (A) ITO/APTES-functionalized surface and (B) ITO surface. Both surfaces were incubated with carboxylate-modified fluorescent beads under a similar protocol.

## 2. ProG

A labeled fluorescent form of ProG solution was used to test the morphology of the SAM of ProG on the ITO/APTES surface. ProG was conjugated to Alexa Fluor 488 using a protein labeling kit (caA10235, Thermo Fisher Scientific) and following the same protocol of labeling described by the vendor. Samples of ITO/APTES were functionalized for four hours with different concentrations of labeled ProG 2  $\mu\text{g/mL}$ , 4  $\mu\text{g/mL}$ , and 8  $\mu\text{g/mL}$ . The labeled ProG solutions were filtered using a 0.2  $\mu\text{m}$  membrane filter before being functionalized on the ITO/APTES electrode. Then, the functionalized samples were analyzed by confocal imaging microscopy. It was found that the sample treated with 4  $\mu\text{g/mL}$  of labeled ProG exhibited a smoothly uniform surface and was

chosen as the optimal concentration as illustrated in Figure 9(a). Then, the labeled ProG was used also in conjunction with the SM-EA-IOW device to fully investigate the adsorption kinetic process. As indicated in Figure 9(b), one hour gives the sample enough time to functionalize the ITO/APTES surface with a 4  $\mu\text{g/mL}$  solution of labeled ProG. A 10 mL volume of PBS, which corresponds to five times the volume of the flow-cell, was used to rinse the electrochemical flow-cell.

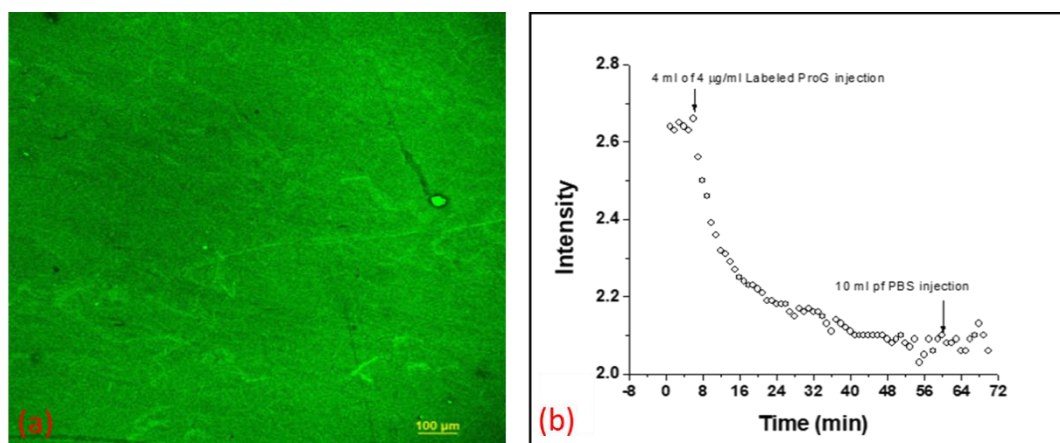


Figure 9: (a) Confocal image of the ITO/APTES SM-EA-IOW surface functionalized with the labeled ProG (4  $\mu\text{g/mL}$ ) solution. (b) Intensity versus time providing adsorption kinetics of the labeled ProG (4  $\mu\text{g/mL}$ ) into the device surface. The setup for these measurements is similar to the one described in chapter 2 Figure 2-2, except for using a 488 nm laser and no potential was applied to the device. To minimize photobleaching effects the laser beam was blocked between readings ( $\sim 1\text{min}$ ) and the power propagating through the waveguide was substantially reduced.

### 3. Cytochrome c antibody

Next the adsorption kinetic process of Cyt-C Ab on the ITO/APTES/ProG surface was characterized, a labeled Cyt-C Ab (Cytochrome c (A-8) mouse monoclonal IgG2b

Alexa Fluor. 647, Santa Cruz Biotechnology) was used in conjunction with the SM-EA-IOW device. Based on the results displayed in Figure 10(a), an incubation time of one hour was then adopted to functionalize the ITO/APTES/ProG surface with Ab with 2  $\mu\text{g}/\text{mL}$  solution concentration. Also, a 10 mL PBS that corresponds to five times the volume of the flow-cell was used to rinse the electrochemical cell. The uniformity of the SAM of labeled Ab on ITO/APTES/ProG SM-EA-IOW surface was tested under confocal fluorescence imaging with results shown in Figure 10(b) indicating that we have successfully functionalized the ITO/APTES/ProG SM-EA-IOW with Ab uniformly using a 2  $\mu\text{g}/\text{mL}$  concentration for one hour incubation. A dual color fluorescent image was used to identify both the labeled ProG and labeled Ab layers, as shown in Figure 10(c).

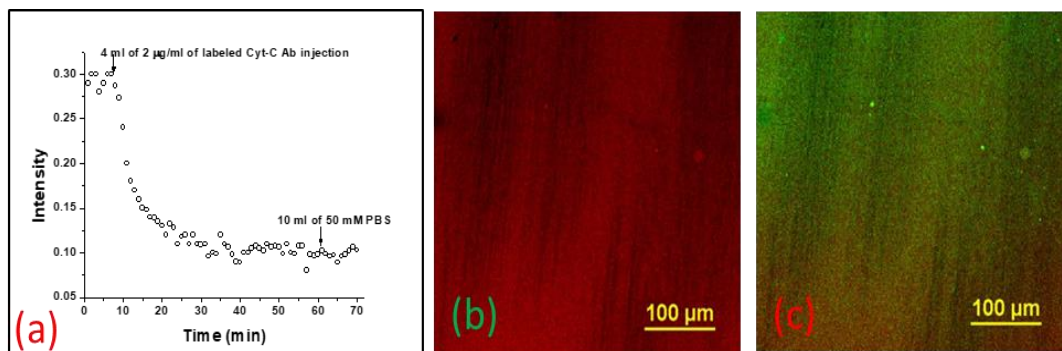


Figure 10: (a) Intensity versus time providing adsorption kinetics of the labeled Cyt-C antibody (2  $\mu\text{g}/\text{mL}$ ) injected into the flow-cell. The setup for these measurements is similar to the one shown in Figure 2-2 except for using a 633 nm laser and no potential was applied. To minimize photobleaching effect the laser beam was blocked between readings ( $\sim 1$  min) and the coupled power into the SM-EA-IOW device was substantially reduced. (b) Confocal image of labeled Cyt-C antibody (2 $\mu\text{g}/\text{mL}$ ) functionalized on the

ITO/APTES/ProG SM-EA-IOW surface. (c) Dual color confocal image of green-labeled ProG protein and red-labeled Cyt-C antibody.

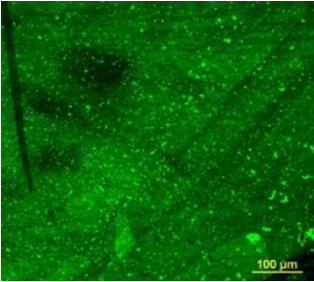
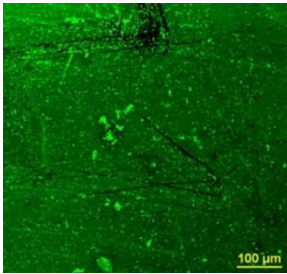
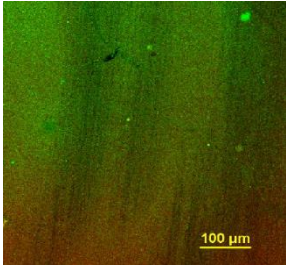
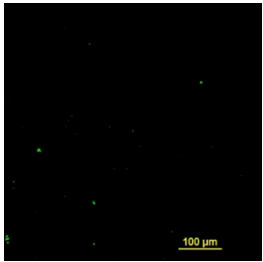
#### 4. Cleaning protocol

The functionalized SM-EA-IOW with APTES is permanent due the strong binding between ITO and APTES. The resilience of the APTES functionalized surface over time was tested under device operating conditions and using confocal imaging; no major change in the performance of the APTES layer was observed over time. Also no change in the SM-EA-IOW performance (coupling loss, resistance, etc.) was observed after several cleaning processes using the carbonate solution Table (A) (I,II and III) summarizes the results of the SM-EA-IOW performance after several carbonate cleaning processes. Also Table (A) (IV) shows the effective use of carbonate for the recycling of the SM-EA-IOW surface.

Table A: (I) Resistance test before and after cleaning process of the SM-EA-IOW surface using carbonate solution. The resistance was measured using a digital multi-meter, the average of ten resistance measurements was acquired and during all the measurements the distance between the electrodes was set to be approximately constant. (II) Waveguide mode technique as described elsewhere [66] was employed to measure the optical coupling loss of the SM-EA-IOW before and after several cleaning processes. (III) ITO/APTES reactivity test before and after cleaning process; two ITO samples were functionalized with APTES under same condition, first one was conjugated with carboxylate beads before sonication and the second ITO/APTES sample was sonicated in carbonate three times for 30 minutes each and then conjugated with carboxylate beads, the confocal images were taken after each sample was conjugated with carboxylate



beads. (IV) Fluorescence labeled (ProG and Cyt-C Ab) complete bio-conjugation on the SM-EA-IOW was used to show the effective cleaning of the SM-EA-IOW waveguide surface using sonication in a carbonate solution with pH (9-11).

Num	Test	Before carbonate sonication	After carbonate sonication
I	Resistance	924±7 $\Omega$	930±7 $\Omega$
II	Coupling loss	6.8 dB	7.2 dB
III	APTES reactivity		
IV	Cleaning test complete Bio-functionalization (ITO/APTES/ProG/Cyt-C Ab) sonicated for 30 minutes		

## Appendix 6: Calculation of MB-Labeled H5N1 Ab

The degree of labelling (dye-to-protein ratio) can be determined by absorption spectroscopy making use of the Lambert-Beer law and a simple measurement of the UV-VIS spectrum the conjugate solution as obtained after column filtration as shown in Figure 11.

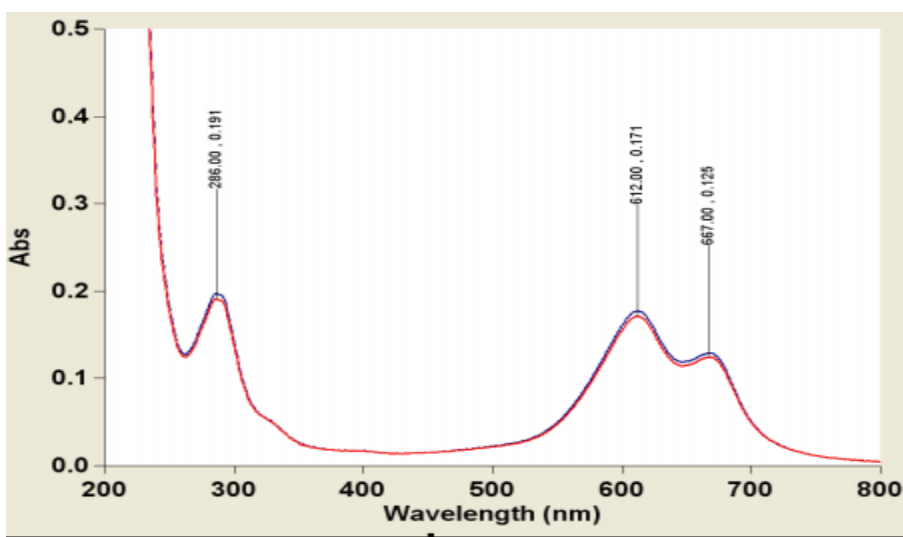


Figure 11: UV-Vis spectra of MB-labeled H5N1 Ab.

The absorbance ( $A_{610}$ ) at the absorption maximum which is observed to be at 610 nm of the MB ester dye and the absorbance ( $A_{280}$ ) at 280 nm (absorption maximum of proteins).

$$\text{The antibody concentration} = \frac{(A_{280} - (A_{610} \times 0.28)) \times \text{dilution factor}}{203000}$$

where  $203000 \text{ cm}^{-1}\text{M}^{-1}$  is the molar extinction coefficient of a typical IgG antibody and 0.28 is correction factor to account for absorption of the dye at 280 nm.

$$\text{The dye concentration} = \frac{A_{610} \times \text{dilution factor}}{26000}$$

Degree of labelling = antibody concentration/ dye concentration

Several conjugations were done and the data shown in Table B below summarizes the consistency of the degree of labelling

Table B: Summary of calculated degree of labeling of the MB-labeled H5N1 Ab for several runs.

Date	Abs ~ 286 nm	Abs ~ 612 nm	Conc. Lab. Ab ( $\mu$ M)	$\mu$ g/mL Lab. Ab	mol dye/mol Lab. Ab
June 28	0.203	0.190	2.21	318	2
July 25	0.197	0.177	2.18	314	2
July 26	0.191	0.171	2.12	305	2
July 27	0.191	0.171	2.12	305	2

	SPR (Reichert systems)	ITC	MST	BLI
Kinetics	Yes	No	No	Protein-protein only
Affinity	Yes	Yes	Yes	Yes
Thermodynamics	Yes	Yes	Yes	Limited
Stoichiometry	Yes	Yes	Yes	Yes
Concentration – analyte	Yes	No	No	Yes
Affinity range	pM – mM	nM – $\mu$ M	pM – mM	nM – $\mu$ M
Precision of read-out	High	Medium	Low	Medium
Sensitivity	High	Low	Medium	Low
Temperature range	10°C below ambient – 70°C	2-80°C	20-45°C	Ambient + 4°C
Sample consumption	Low	High	Very low	Low
Sample types*	Maximum flexibility	Few	Intermediate	Intermediate
Buffers	No restrictions for aqueous solutions Concentrated Acids/Bases Most organic solvents	Aqueous solutions with small amounts of organic solvents	No restrictions for aqueous solutions (incl. 8M urea, 4M MgCl <sub>2</sub> etc.)	Aqueous solutions with small amounts of organic solvents
Maintenance	Operator or service technician	Service technician	NA	Service technician
Signal read-out (change of...)	Refractive index	Temperature	Fluorescence intensity	Wavelength shift
Benefits	Highest information content Reference method for FDA/ICH/EMA Max experimental flexibility	No immobilization No labeling	Low sample consumption	Highest throughput
Disadvantages	Immobilization of one binding partner required. Trained personnel is required for high quality data	High sample Consumption Limited applicability – reactions with measureable temperature change.	Cannot discern 2 <sup>nd</sup> binding site or non-specific binding Labeling with hydrophobic fluorophores required, which can alter binding profile. High CV of fluorescence data.	Immobilization of one binding partner required. Dissociation phases are imprecise due to analyte rebinding (no flow through system)

\*See table on following page for detail list of sample types

## Appendix 8: Gram Positive and Gram Negative Bacteria

The terms gram positive or gram negative bacteria are named after Hans Christian Gram, a scientist who devised a way to differentiate between the two types of bacteria. Gram positive bacteria only have a cell wall. That cell wall is full of layers of peptidoglycan. The layers of peptidoglycan retain the dye crystal violet, hence called 'gram positive'. Gram negative bacteria have an additional outer membrane that contains only one layer of peptidoglycans in between this outer membrane and the cell wall. With this additional membrane with only one layer of peptidoglycan, the bacteria cannot retain the dye, hence the term 'gram-negative'.

A stock solution of endotoxin from E. Coli K12 strain cultured in LB broth provided by Dr. Deborah Yoder-Himes at the University of Louisville was prepared and quantified. In a 2 mL tube, the bacteria and broth were boiled in a beaker on a hot plate with stirring for 1.5 hours. The tube was removed from the boiling water, cooled and placed into 10 mL of DI water for dilution. Quantification of the endotoxin was performed using a Limulus Amebocyte Lysate (LAL) assay (Thermo-Fisher, Waltham, MA). A standard curve of endotoxin was prepared according to manufacturer's instructions. Due to the high endotoxin content from the boiled E. coli, a final dilution of  $1 \times 10^{15}$  contained a detectable amount of endotoxin that fell within the standard curve. In a 96 well plate, the standards and samples, in triplicate, were incubated with the LAL for 10 minutes. Then the chromogenic substrate was added and incubated for 6 minutes. To terminate the reaction, 25% v/v acetic acid was added to all standards and samples. Absorbance measurements of 405nm were made on a Biotek spectrophotometer (Winooski, VT).

## Appendix 9: Conjugation Polyclonal Lipopolysaccharides (LPS) Endotoxins Ab with Methylene Blue Ester

The antibody to be labeled with the methylene blue must be free of all azide for a more efficient reaction. Dialysis is performed for 24 hours into sodium bicarbonate buffer with a pH 8.3 that includes 3 changes of sodium bicarbonate buffer. Methylene blue is conjugated to a polyclonal LPS antibody through ester-linkage chemistry. The methylene blue is purchased from LGC Biosearch Technologies (Petaluma, CA) with the ester-linkage chemistry already performed, known as methylene blue ester. Using a 1:2 molar ratio of antibody to methylene blue ester dye, the antibody and dye are incubated together and mixed for 1-2 hours at room temperature. To separate the unbound dye and antibody-methylene blue dye complex, gel separation (Thermo-Fisher, Waltham, MA) is performed. The column is equilibrated with 50 mM phosphate buffer solution. The dye-antibody solution is then poured into the column and allowed to absorb into the gel. PBS is then added and the size exclusion separation begins. The premise is the antibody-dye complex is heavier than the unbound dye and unbound antibody. There is a clear band of separation within the column (Figure 12). The first band is collected and measured by UV-Vis in the 200-800 nm range, Figure 13. Degree of labeling and concentration are calculated based on Beer's Law.

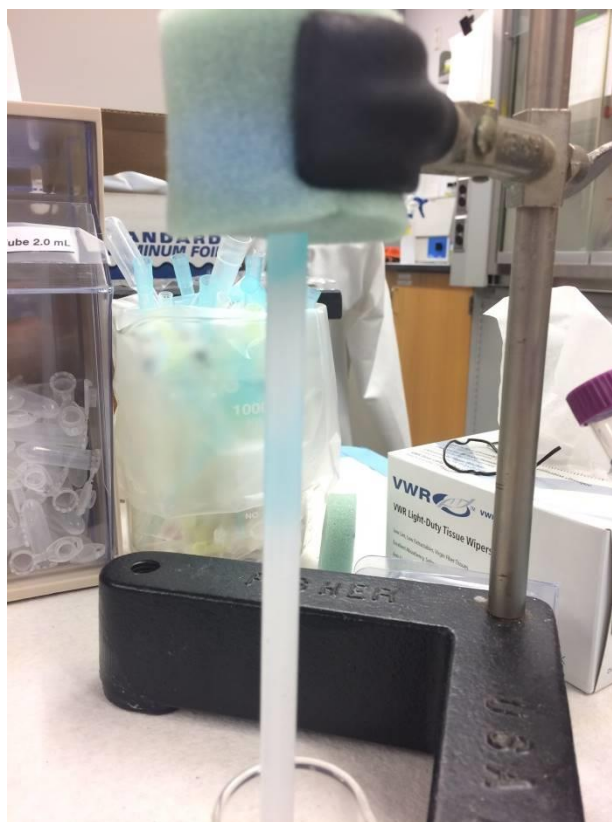


Figure 12: Gel separation column (Thermo-Fisher, Waltham, MA) with a clear band of separation within the column.

$s = 0.276$

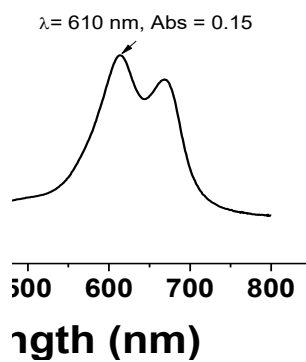


Figure 13: UV-Vis spectra of MB-labeled H5N1 Ab.

## Appendix 10: Preparation of Cresyl Violet Maleamic Acid

Cresyl Violet acetate (CrViAc) purchased from Sigma Aldrich was dissolved with enough amount in PBS to prepare a stock solution. The stock solution of CrViAc UV-Vis spectrum was then collected as illustrated in Figure 14, which features a peak at around 592 nm, that have a molar absorptivity of  $83000 \text{ cm}^{-1}/\text{M}$  [130], and using Beer's law one can determine the concentration of the stock solution, and any desired CrViAc solution concentration was prepared by dilution from the stock solution.

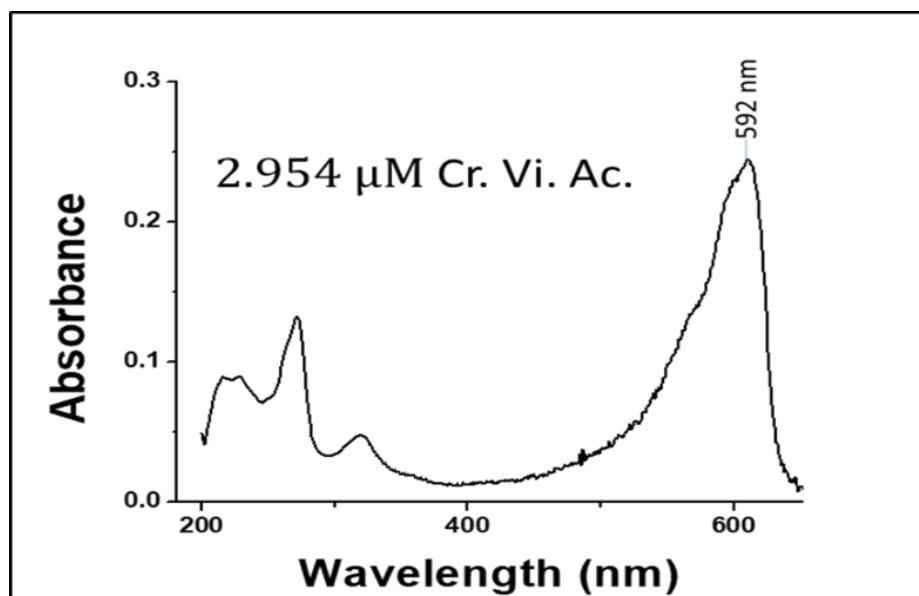


Figure 14: UV-Vis spectrum of Cresyl violet acetate collected by a UV-Vis spectrophotometer Cary 300.

CrViMa was synthesized as follow

- A mixture of 1,284 mg of cresyl violet acetate (200 mM) and 600 mg excess of maleic anhydride (306 mM) in 20 mL of glacial acetic acid was stirred at an ambient temperature for 24 hours. The reddish-brown solid product was filtered and washed with 150 mL of hexane and ether, Figure 15.



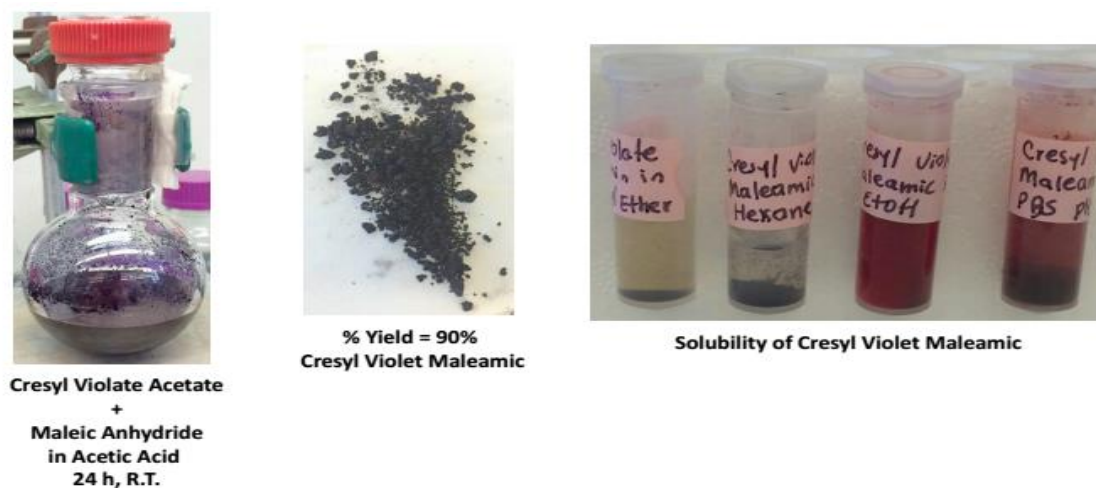


Figure 15: Product of the reactions described.

For characterization of CrViMa product the UV-Vis spectrum Figure 16 of CrViAc and CrViMa was collected with the same concentration, a shift in the peak of the CrViAc was observed compared to the CrViMa, such shift indicates the successful synthesis of a new product.

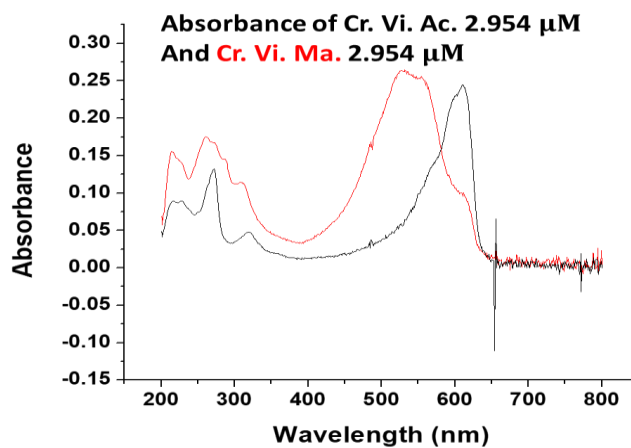


Figure 16: The UV-Vis of the initial product CrViAc (black trace) with a peak at 592 nm and the final product CrViMa (red trace) with a peak at 514 nm.

Also the IR spectrum of both CrViAc and CrViMa was acquired and shown in Figure 17, the IR measurements confirm the successful synthesis of CrViMa

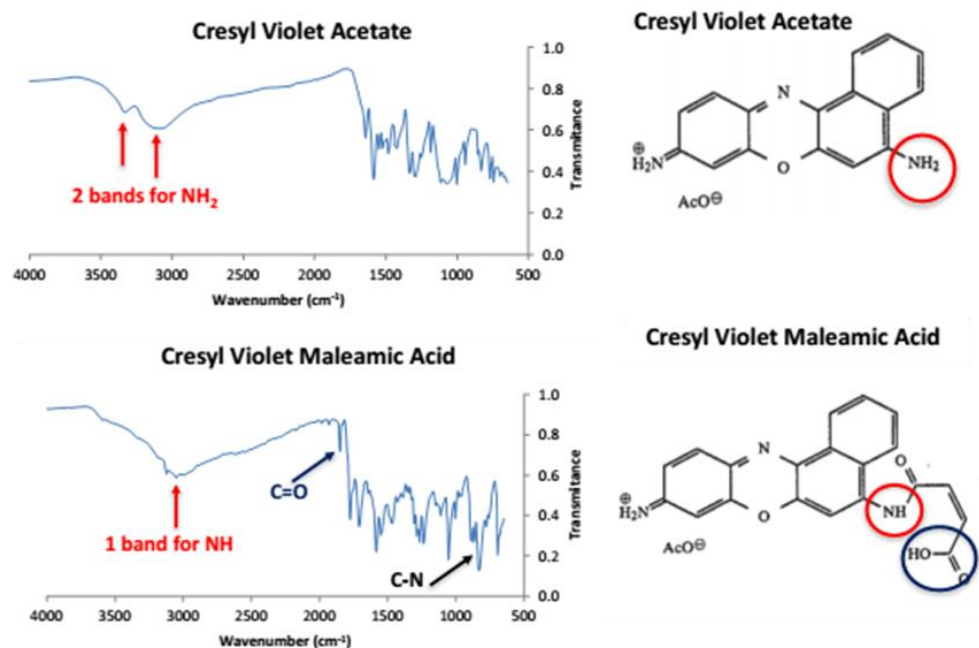


Figure 17: IR spectrum of CrViAc and CrViMa

## Appendix 11: CrViMa Conjugation to H5N1 Secondary Antibody

Prior to conjugation, the antibody undergoes dialysis to perform a buffer exchange into 0.1M 2-(N-Morpholino) ethanesulfonic acid hydrate (MES) buffer to remove any azide and to bring the antibody down to pH 6.0 needed for optimum reaction. Dialysis goes for 24 hours with 3 changes of buffer. A stock concentration of Cresyl Violet maleamic acid is dissolved into anhydrous dimethylsulfoxide (DMSO) aliquoted and stored at -20°C. It then can be diluted further into MES buffer. The Cresyl Violet maleamic acid, N-hydroxysulfosuccinimide (sulfo-NHS) and N-Ethyl-N'-(3-dimethylaminopropyl) carbodiimide hydrochloride (EDC) are calculated for a 50:1 molar ratio to antibody. This is to help have the excess to drive the reaction of the dye to conjugate to the antibody. The reaction happens in the dark either in a foil covered tube or light blocking tube with a micro-stirbar on a magnetic stir plate overnight at 4°C. After the reaction is complete, the separation of conjugated antibody is completed just the same as the methylene blue ester. Degree of labeling and antibody concentration are calculated using Beer's law.

## Appendix 12: Fluorophore Beads Sample Preparation

Samples with the beads of 20 nm size were prepared according to the following protocol: first the acquired fluorescent solution was sonicated for 15 minutes, then diluted ( $\sim 1:10^5$ ) in ethanol (SHBD20324, Sigma, Saint Louis, Missouri, USA). The diluted sample was sonicated again for another 15 minutes. The fluorescent species were immobilized on microscope glass coverslips (VWR 24×60 mm, VWR, Radnor, Pennsylvania, USA). The coverslip was initially cleaned with ethanol and coated with Poly-L-lysine (P8920, Sigma, Saint Louis, Missouri, USA) by incubating the whole sample for 10 minutes inside the Poly-L-lysine; Poly-L-lysine was used as a linker. The coverslip was washed off with deionized water and blown-dried with nitrogen gas. A drop ( $\sim 20 \mu\text{l}$ ) of the diluted fluorescent solution was pipetted onto the coverslip and allowed to immobilize onto the surface for about  $\sim 10$  minutes, before washing with deionized water and drying with nitrogen gas. Finally, a drop ( $\sim 20 \mu\text{l}$ ) of 2,2'-Thiodiethanol (TDE) (88559, Sigma, Saint Louis, Missouri, USA), which has an index of refraction of about 1.51, was added to the sample by drop-casting as an embedding medium. To obtain an embedding medium of TDE that has an index of refraction of about 1.51; TDE was mixed with phosphate buffered saline PBS with a ratio of 97% (v/v) TDE, then adjusted to a pH of  $\sim 7.5$  with HCL/NaOH solutions [131]. The coverslip was then pressed against a microscope slide and sealed with nail polish. To test the ability of the modulated STED technique to obtain super-resolution images even under conditions of substantial mismatch in index of refraction between the cover slip and the embedding medium, a sample of the fluorescent-beads was prepared under the same protocol mentioned above, but instead of using TDE Vectashield was used (H-1000-10,

Vectorslabs, Burlingame, California, USA) with an index of refraction of 1.45 as the embedding medium.

### Appendix 13: Retinal Slices with Fluorescently Labeled Structures Sample Preparation

All experimental procedures involving animals were approved by the University of Louisville Animal Care and Use Committee. Transgenic mice with green fluorescent protein (GFP) labeled bipolar cells [132] were euthanized using anesthetic overdose, eyes were removed and retinas dissected in 0.01 M PBS. The retina was fixed by immersion in 4% paraformaldehyde for 20 minutes then incubated for an hour each in a series of sucrose solutions in 0.1 M phosphate buffer of increasing concentrations (5%, 10%, 15%, and 20%). The retina was then incubated for 1 hour in Tissue Tek OCT tissue freezing media (4583, Ted Pella, Inc., Redding, California, USA) and 20% sucrose (2:1) and flash frozen using liquid nitrogen in the same solution. Frozen blocks were sliced using a cryostat to yield vertical sections of the retina in which the three nuclear layers were all visible (bipolar cells reside in the middle nuclear layer). Cryoslices were dried on coated slides for 30-60 minutes then incubated in 0.01M PBS for 10 minutes followed by incubation in blocking solution (10% normal donkey serum in 0.5% triton X in PBS) for 1 hour at room temperature. Slides were incubated in primary antibody diluted 1:1000 in blocking solution overnight at 4 °C. Primary antibodies included chicken anti-GFP (Invitrogen, Carlsbad, California, USA) to label the GFP positive bipolar cells and mouse anti-C-terminal binding protein 2 (Chemicon, Shinagawa-Ku, Japan), a marker for the ribbon synapse. Slides were washed in PBS (4×10 min) then incubated for 1.5 hours at room temperature in secondary antibody diluted 1:1000 in PBS. Secondary antibodies included donkey anti-chicken and donkey anti-mouse conjugated Alexa 488. Slides then were washed in PBS (4×10 minutes) and embedded in TDE medium; to prevent cellular structure damaging due to osmotic shock [131] the exchange of water with TDE was

done slowly using the following protocol; the exchange of water with TDE was done by incubating the labeled samples in a series of diluted TDE solution with PBS: 10% (v/v) TDE, 25% (v/v) TDE, 50% (v/v) TDE, and 97% (v/v) TDE. The samples were incubated for 5 minutes in each diluted solution of TDE from low to high concentration, and then the samples were mounted in 97% (v/v) TDE. Finally; slides were covered with glass coverslips then sealed with nail polish.

## CURRICULUM VITAE

Jafar H. Ghithan

### ➤ **EDUCATION**

- **M.Sc. Physics and Astronomy** May 2014  
University of Louisville, Louisville, KY, USA GPA 3.975/4.0
- **M.Sc. Physics and Astronomy** May 2010  
Al-Quds University/ Jerusalem, Palestine
- **B.Sc. Degree Physics & mathematics/Physics** June 2007  
Birzeit University/ Ramallah, Palestine

### ➤ **EXPERIENCE**

#### **Research Assistant / University of Louisville**

*Physics and Astronomy Dept.*

**August 2014 - Present**

- Successfully fabricated single-mode electro-active integrated optical waveguides using optical photolithography, atomic layer deposition (ALD), sputtering coating, and ion beam etching processing.
- Developed an innovative approach to detect and quantify influenza virus molecules by combination of electro-chemical and optical transduction responsive biological assay onto novel photonic devices.
- Studied electron-transfer kinetics and mechanisms of redox active molecules at different molecular assemblies by single-mode, electro-active, integrated optical waveguides.
- Built a super-resolution imaging tool that is capable of achieving far-field images with resolution better than 50 nm in the visible part of the spectrum.
- Developed an electron-state depletion imaging microscope to study and detect variations, defect states, disorder, and impurities in materials.

Graduate Teaching Assistant / University of Louisville



Physics and Astronomy Dept.

August 2012 - July 2014

- Responsible for grading student's lab reports/exams in a timely manner
- Planned lab sections and course tutorials for students
- Ensured students maintained good laboratory practices
- Assist faculty members with classroom instruction, exams, record keeping...
- Teach several undergraduate courses

**Research Assistant / Al-Quds University**

*Physics and Astronomy Dept.*

**August 2010- June 2012**

- Studied proteins interaction with drugs using AFM and FTIR.
- Binding constants measurements of drugs interactions with proteins, using fluorescence and UV spectrophotometers.

**Graduate Teaching Assistant / Al-Quds University**

*Physics and Astronomy Dept.*

**August 2007- July 2010**

- Oversaw and ran entry level college physics labs, covering multiple topics such as mechanics and electromagnetism.
- Calibrated and troubleshoot physics labs equipment.
- Responsible for grading student's lab reports/exams in a timely manner.
- Planned lab sections and course tutorials for students.
- Ensured students maintained good laboratory practices.

**Birzeit University**

*Physics and Astronomy Dept., Palestine*

**April 2006 - June 2007**

- Final-year project: studied the conduction mechanism in ultrathin discontinuous metal films using vacuum evaporation system.

➤ **SELECTED AWARDS**

- The Manuel Schwartz Award for Excellence, University of Louisville 2018.
- National Science Foundation (NSF) Innovation Corps (I-Corps) 2018.
- The Manuel Schwartz Award for Excellence, University of Louisville 2014.
- Musa Naser Undergraduate Outstanding Physics Student Award, Birzeit University, 2004-2007.

➤ **PUBLICATIONS RELATED TO THIS DISSERTATION**

- **Jafar H. Ghithan**, Monica Moreno, Guilherme Sombrio, Rajat Chauhan, Martin G. O’Toole, and Sergio B. Mendes. “Influenza Virus Immunosensor with an Electro-Active Optical Waveguide under Potential Modulation”, **Optics Letters** **42 (7) 1205-1208, 2017.**
- Sergio B. Mendes, **Jafar H. Ghithan**, Monica Moreno, Guilherme Sombrio, Rajat Chauhan, and Martin G. O’Toole. “Detecting Influenza virus with Electro-Active Optical Waveguides”, **Optics and Photonics News (Optics in 2017)** **39, 2017.**
- **Jafar H. Ghithan**, Jennifer M. Noel, Thomas J. Roussel, Maureen A. McCall, Bruce W. Alphenaar, and Sergio B. Mende, “Photobleaching Reduction in Modulated Super Resolution Microscopy”, **Journal of Biomedical Optics**, submitted, under revision.
- **Jafar H. Ghithan**, Monica Moreno, Martin G. O’Toole, and Sergio B. Mendes, “Adsorption Properties and Electron-Transfer Rates of a Redox Probe at Different Interfaces of an Immunoassay Assembled on an Electro-Active Photonic Platform”, **The Journal of Physical Chemistry C**, submitted, under review.
- Austin L. Carver, **Jafar H. Ghithan**, Sergio B. Mendes, and Bruce W. Alphenaar “Non-local defect detection using scanning capacitive photocurrent spectroscopy”, **Applied Physics Letters**, under preparation.
- **Jafar H. Ghithan**, Aymen H. Qatamin, Monica Moreno, Betty M. Nunn, Martin G. O’Toole, and Sergio B. Mendes, “Immunosensing with Electro-Active Photonic Devices”, **Invited Book Chapter**, RSC’S Detection Science Series – IMMUNOSENSORS - **Royal Society of Chemistry** 2018, under preparation.

➤ **CONFERENCE PRESENTATIONS RELATED TO THIS DISSERTATION**

- **Jafar H. Ghithan**, Monica Moreno, Guilherme Sombrio, Martin G. O’Toole, and Sergio B. Mendes. “Avian Influenza Virus Immunosensor Using Single-Mode, Electro-Active, Integrated Optical Waveguide”, **SeTu2E, Optics in the Life Sciences Congress, OSA April 2 2017**, San Diego, CA.
- **Jafar H. Ghithan**, Monica Moreno, Martin G. O’Toole, and Sergio B. Mendes. “Characterization of an Immunoassay Assembly on an Electro-Active Waveguide Platform”, **BoS2A.6, Advanced Photonics, OSA, July 25 2017**, New Orleans, LA.
- Monica Moreno, **Jafar H. Ghithan**, Guilherme Sombrio, Martin G. O’Toole, and Sergio B. Mendes. “Rapid and Sensitive Waveguide Biosensor for Detection of H5N1 Influenza A Virus”, **Pittcon Conference and Expo, March 2017**, Chicago, IL. poster presentation.

- **Jafar H. Ghithan**, Monica Moreno, Robert S. Keynton Martin G. O'Toole, and Sergio B. Mendes. "Detection of Influenza Antigen with Electro-active Waveguides" **March 26 2018**, Monterey, CA. poster presentation.
- **Jafar H. Ghithan**, Sergio B. Mendes "STED Microscopy", Invited talk, Department of Anatomical Sciences and Neurobiology, University of Louisville, July 3 2015.
- **Jafar H. Ghithan**, Rodrigo S. Wiederkehr, Farzaneh Hoveyda, Austin L. Carver, Thomas J. Roussel Bruce W. Alphenaar, and Sergio B. Mendes, "Development of an Electron State Depletion Microscope", 2013 Kentucky Nano-Symposium, poster presentation.

#### ➤ **PRIOR PUBLICATIONS**

- Abuteir M. M., **Ghithan J.**, Abu-Taha M. I., Darwish S. M., Abu-hadid M. M. "Spectroscopic Approach of the Interaction Study of Ceftriaxone and Human Serum Albumin", **Journal of Biophysics and Structural Biology**, **02/6(1):1-12, 2014**.
- Saqer M. Darwish, **Jafar H. Ghithan**, Musa M. Abuteir, Mariam Faroun, and Mahmoud M. Abu-hadid. "Spectroscopic Investigations of Pentobarbital Interaction with Transthyretin", **Journal of Spectroscopy**, **Volume 2013, Article ID 927962, 10 pages**.
- M. M. Abuteir, **J. H. Ghithan**, S. M. Darwish, M. M. Abu-hadid. "Study of Progesterone Interaction with Human Serum Albumin: Spectroscopic Approach", **Journal of Applied Biological Sciences**, **5 (13): 35-47, 2011**.
- M. M. Abuteir, **J. H. Ghithan**, S. M. Darwish, M. M. Abu-hadid "Multi Spectroscopic Investigation of the Interactions between Cholesterol and Human Serum Albumin", **Journal of Applied Biological Sciences**, **6 (3): 45-55, 2012**.

#### ➤ **PRIOR CONFERENCE PRESENTATION**

- **Jafar H. Ghithan**, Saqer M. Darwish, Musa M. Abuteir, and Mahmoud Abu-hadid, "Temperature-dependent  $\beta$ -sheet formation in Transthyratine Protein, detection of oligomeric structures using FTIR and AFM", 2012 Poster presentation, Max Plank Institute of Molecular Cell Biology and Genetics, poster presentation.

#### ➤ **MEMBERSHIPS**

- Optical Society, former Optical Society of America.
- Kentucky Academy of Science.